Mixed-Mode Fracture & Fatigue Analysis of Rotating Blades Using the Extended Finite Element Method

by

Juan J. Reinés-Navedo

A thesis submitted in partial fulfillment of the requirements for the degree of

MASTER OF SCIENCE
in
MECHANICAL ENGINEERING

UNIVERSITY OF PUERTO RICO
MAYAGÜEZ CAMPUS
2010

Approved by:

_____	_____
Ricky Valentín, Ph.D. Member, Graduate Committee	Date
_____	_____
Pedro Quintero, Ph.D. Member, Graduate Committee	Date
_____	_____
Vijay K. Goyal, Ph.D. Chair, Graduate Committee	Date
_____	_____
Omar Colón-Reyes, Ph.D. Representative of Graduate Studies	Date
_____	_____
Gustavo Gutierrez, Ph.D. Chairperson of the Department	Date

Mixed-Mode Fracture & Fatigue Analysis of Rotating Blades Using the Extended Finite Element Method

Abstract

This work focuses in the analysis of *mixed-mode* crack propagation and fatigue of two dimensional rotating blades using the Extended Finite Element Method (XFEM). A horizontal plate model simulates a UH-60 helicopter rotor blade rotating at a constant angular velocity. The calculation of body forces and mixed-mode fatigue analysis was implemented into XFEM. The critical location is at about 8% from the rotating hub for a single-edged crack. At this critical location, a crack size of approximate 15% of total blade width will cause catastrophic failure.

Análisis del Modo Mixto de Fractura y de Fatiga de las Aspas Giratorias Utilizando el Método del Elemento Finito Extendido

Resumen

Este trabajo se enfoca en el análisis de la propagación de grietas y fatiga en modo mixto de placas rotando en dos dimensiones usando método extendido de elementos finitos (XFEM). Un modelo de placa horizontal simula al helicóptero UH-60, girando a una velocidad angular constante. Se ha implementado en XFEM la calculación de las fuerzas de cuerpo y el análisis de modo mixto de fatiga. El lugar crítico se encuentra en alrededor del 8% con respecto al centro de rotación. En esta localización critica, una grita de 15% del ancho de la aspa produce falla catastrófica.

ACKNOWLEDGEMENTS

First, I want to thank God; because of His will we are given the privilege of life. Next, I want to thank my parents Juan Reinés and Mary Navedo for their unconditional love and support, even through my hastiest mistakes, and to my sister, Celimar Reinés, for her steady embrace and consistency in my life. I also would like to thank my girlfriend, Glorimar Ramos, for her patience and unconditional support through this thesis.

I am also indebted to say my heartily thanks to Dr. Vijay K. Goyal for the confidence in me that he has always shown and for all the years that I have spent working with him. His unstinting support and guidance always remained a key factor in my success. I also want to thank Dr. Goyal also for providing me this opportunity and for making possible this step in my career.

I want to thank Innovations in Research & Engineering (A29IRE), small business located in PR, for their support throughout this work. I found invaluable the theoretical and computational help they provided.

I would like to deeply thank Prof. Stéphane Bordas, from Cardiff University, and his research Institute in Modeling and Simulation in Mechanics and Materials. Special thanks to Mr. Sundararajan Natarajan, his doctoral student. They are frontrunners in this field and their inputs and technical insights were invaluable. They provided us with a preliminary XFEM code and helped us to speed up our knowledge in the field. It was a great to communicate with them via conference calls, Skype, and emails.

I would also like to thank the few professors that have had a significant impact in my life and education. I would like to thank Mrs. Delgado and Mr. Gillette, for teaching me the math I know, and for their guidance in my early years.

TABLE OF CONTENTS

LIST OF FIGURES

LIST OF TABLES

CHAPTER 1: PRELIMINARY REMARKS

This work consists in using the Extended Finite Element Method (XFEM) to conduct *mixed-mode* (modes I and II) crack propagation and fatigue analysis in rotating blades, being this a major need for industries such as turbine fan-blade and helicopter blade designs. Here, a two-dimensional rotating blade with a constant angular velocity is subjected to single edged-cracks at the blade's leading edge. We conducted the crack propagation analysis using one of the newer techniques known as the Extended Finite Element Method (XFEM). We performed static fatigue analysis on each single edged-crack location, leading to the identification of the most critical location. We used a commercially available explicit solver such as LS-DYNA and results available in the literature to validate our computational results. Finally, we conducted mixed-mode (mode I and II) fatigue analysis to determine the blade's remaining life.

1.1: MOTIVATION

Crack propagation analysis prevents rupture and predicts the remaining duty cycles of rotating elements. Examples of some rotating structural elements are commercial jet engine blades and helicopter rotor blades, shown in Figure 1.1 and Figure 1.2.

Figure 1.1: UH-60 BlackHawk Helicopter, USA [2].

Figure 1.2: Pratt & Whitney PW1000G Turbofan Engine [3].

Figure 1.3: R22 Main Rotor fatal Blade rupture [4].

Helicopter rotor blades are subjected to diverse type of loadings that affects how microscale cracks propagate. Under the main assumption that every analyzed structural element contains a microscopic crack, these cracks eventually propagate if they are subject to loads over a period of time, causing a catastrophic damage, as shown in Figure 1.3**.**

One possibility of crack propagation in rotating blades is because blades service overpasses its life expectancy due to excessive helicopter rotor fatigue, being this the main focus of this work. Fatigue may be defined as the initiation and propagation of microscopic cracks when the structure is subject to cyclic loadings. Examples of these loads as applied to rotating blades may include:

1. In-flight loads
    a) Lift forces
    b) Drag forces
    c) Torque generated by changes in rotor angular velocity (acceleration)
2. Landing loads
3. Vibrations caused by blade flapping
4. Simply just having the engine running

By designing, installing and calibrating load sensors applied directly on critical blade locations we can determine perform crack propagation using experimental techniques. Algera and

Iyyer [5] developed an architecture called Technical Data Analysis (TDA), where they present the tracking system of its rotary wing dynamic component structural life. They used a web-based user interface to determine remaining rotary life cycles for distinct helicopter flight conditions. Moon and Phan [6] studied the latest in wireless sensor technology in order to determine Condition Based Maintenance (CBM). Their main goal was to eliminate the usage of a wired slip ring, in which has limited monitoring capacities, and improve the problem of wireless battery maintenance. These most experimental works, as are most of experimental techniques, are cumbersome and expensive due to destructive testing on the helicopter blade.

Although researcher have widely studied experimental techniques involving the use of data acquisition sensors to determine the remaining duty cycles of helicopter rotor blades, at the best of the authors knowledge little is known on a robust and accurate computational method to determine critical crack locations and predict mixed-mode crack propagation in rotating blades. Hence, the main goal of this work is to determine the life expectancy of rotating blades subjected to leading single edged-crack using mixed-mode fracture techniques.

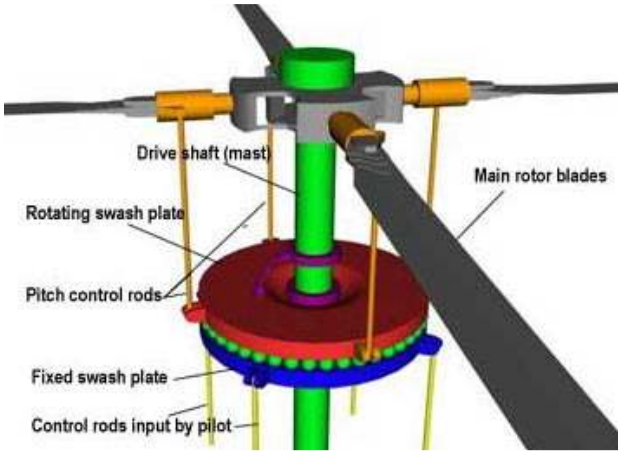

Figure 1.4: Illustration of rotor blade with hub main hub [7].

1.2: PROBLEM DESCRIPTION

In this work, we focus our attention on the modeling and simulating of horizontally rotating blades revolving around a translational stationary axis. Figure 1.4 illustrates helicopter blades connected to its main hub. As previously mentioned, helicopter rotor blades are exposed to fatigue do to loadings such as lift, drag, and thrust. Also, turbulence development on trailing edge section creates unnecessary vibrations, which may lead to crack propagation and, therefore, complete structural failure. Although we generally study the life expectancy of helicopter rotor blades at the design stages, there is a need of a more robust computational model that can predict the direction of crack propagation given the original location of the crack.

Although the maintenance of helicopter rotor blades is crucial, knowing the actual conditions on rotor blades during real flight could make the difference between having a catastrophe landing or a safe one. Factors like cargo weight, *g*-force, and excessive centrifugal forces can cause rotor blades, which passed maintenance inspection, fracture on flight. Aviation companies will spend less money on destructive blade testing and preliminary computational results at the designing process can be used for faster rotary blade prototyping.

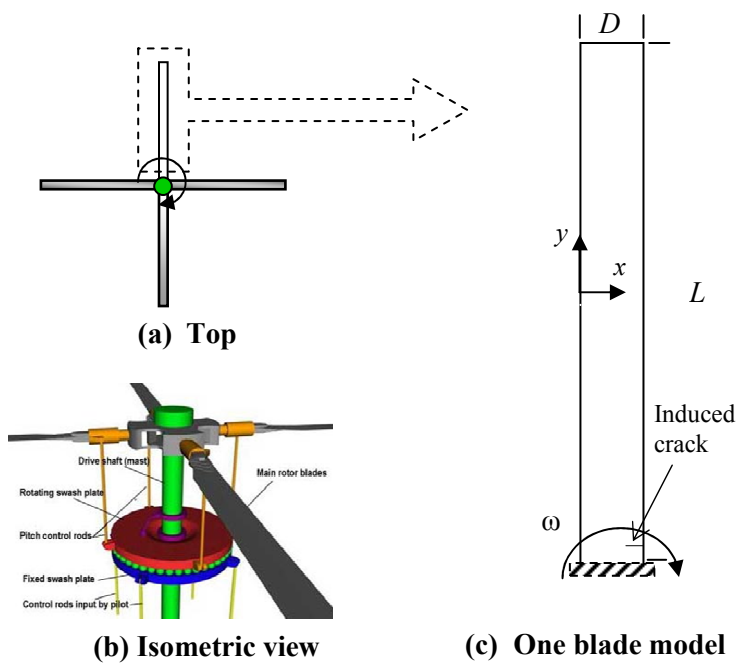

(a) Top **(b) Isometric view** **(c) One blade model**

Figure 1.5: General schematic for the blade model we plan to use throughout this work.

1.2.1: ROTOR BLADE SPECIFICATIONS

For the purposes of this work, we used helicopter blade parameters used by Fries [8], where he studied vibrational analysis done on the helicopter's cockpit due to main rotor damage. Figure 1.5 illustrates the main schematic of our rotating blade. Although helicopters or turbine fans usually have more two or more blades, here we will conduct our study on one rotating blade. The blade will not encounter eccentricity problems by analyzing it alone because we are assuming no eccentricity effect in this work. The blade is 321.96 inches long with a chord of 20.74 inches. These dimensions are representative of a UH-60 military helicopter vibrational analysis conducted by the Army Research Laboratory.

Table 1.1 and Table 1.2 give important rotor blade parameters and rotor characteristics, respectively. The material we used for our rotating blade was Ti-6Al-4V alloy because widely used as the major structural component of the UH-60 main rotor blade [9]. Table 1.3 illustrates the physical properties of the rotor blade alloy we used in this work.

Table 1.1: Main Rotor Parameters.

Parameter	Value
Number of Blades	4
Radius	26.83 ft
Rotor Blade Area	186.9 ft^2

Table 1.2: UH-60 Main Rotor Capabilities.

Parameter	Max Capacity
Thrust	52,000 lbs
Hub Force	15,000 lbs
(Combined Axial/Side Force) Hub Moment	50,000 ft-lbs
(Combined Pitch/Roll Moment) Torque	165,000 ft-lbs

Table 1.3: Mechanical properties of Ti-6Al-4V alloy [10].

Parameter		Value
Modulus of Elasticity		16500 ksi
Poisson's Ratio		0.342
Fracture Toughness		68.3 ksi-in$^{1/2}$
Tensile Strength, Yield		128 ksi
Tensile Strength, Ultimate		138 ksi
Density		0.16 lb/in^{3}
Fatigue crack growth (Paris Law constants)	*A*	1.6777e-22 psi $^{-3.6}$*in$^{-0.8}$
	n	3.6
Fracture Toughness		68.3e3 psi*in$^{0.5}$
Endurance Stress limit, S_e'		74 ksi

1.2.2: ROTATIONAL SPEED

Fluctuating cyclic loading, as those shown in Figure 1.6(a), are encountered in real life flight. These changes in rotational velocity can occur in indefinable number of ways during flight; can be causes by sudden acceleration in flight or by sudden changes in direction. In Figure 1.6(a), "*actual duty cycles*" vary depending on the helicopter flight time. Each flight time has a different velocity profiles and this affect the remaining life cycles of rotating blades. Figure 1.6(b) shows a more simplified duty cycle. In this figure it is assumed that equal flight velocity profiles are repeated in every duty cycle. For the sake of this work, we will assume a steady constant angular velocity of the rotor, shown in Figure 1.6(c). In this figure, one "*ideal duty cycle*" will include an increase in acceleration, then a constant velocity over a period of time. In this work, we will not consider changes in velocity we will only analysis a rotating helicopter blade at constant velocity.

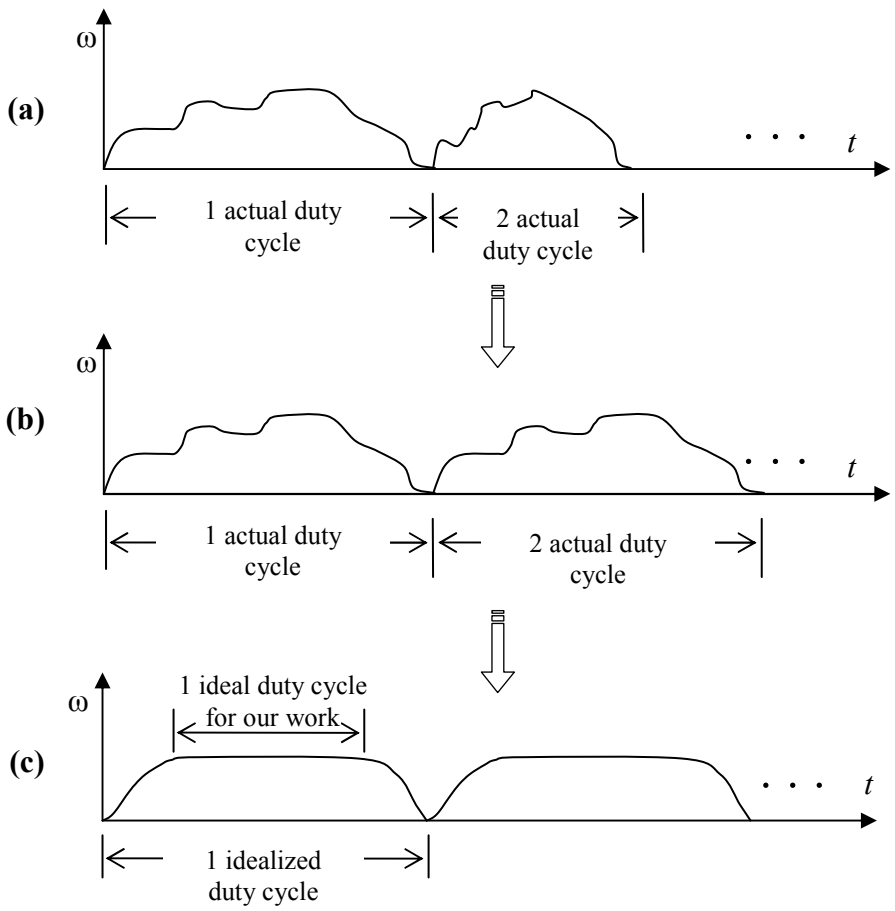

Figure 1.6: Actual and idealized cyclic angular speed.

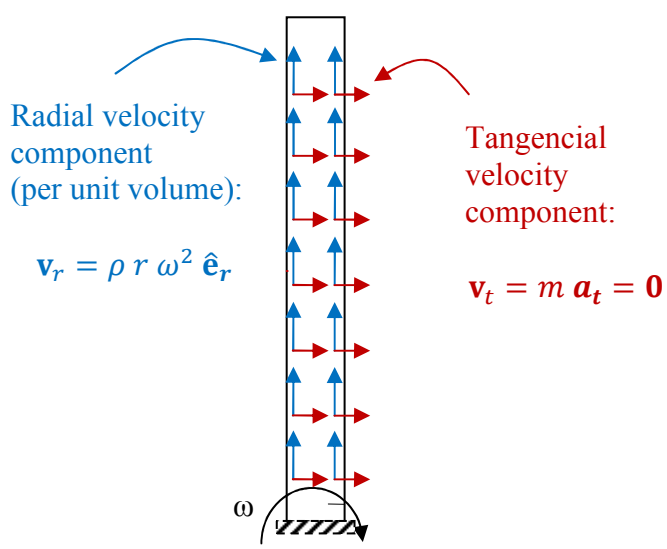

Figure 1.7: Body forces considered for this work.

Flight pattern shown in Figure 1.6(c) does not exist in an actual helicopter flight. Even at a steady helicopter flight, slight changes in rotational velocity are present when affected by cyclic loading, discussed earlier. Figure 1.7 shows the two velocity components acting on the blade: (i) tangential component, and (ii) centrifugal component. Since we are not considering any speed changes (Figure 1.6(c)), centrifugal or radial velocity component will be nonzero while the tangential component will become zero.

1.2.3: ASSUMPTIONS

Throughout this work we made the following assumptions:

1. Ignore the aeroelasticity effects on the blades. Blades are subject to both elastic and aerodynamic loads, especially wind effects from other blades. A complete study must include all these effects. However, for the sake of simplicity and to show the present technique we are ignoring these effects.

2. There are no changes in the rotational velocity. Structures with rotating blades undergo speed changes. However, during a steady rotation we may neglect these changes allowing us to assume a zero tangential acceleration. For a more complete study on rotating blades, we must include the dynamic rotational speed as a function of time. Although the inclusion of speed change may be important it does not stop us from developing the failure methods for steady speed which we may further expand.

3. Ignore bending effects on the rotating blade. The inclusion of bending, which is mainly produced by lift, would bring transverse displacements and thus strains and stresses into the picture. Hence, it would make the problem a three-dimensional one. Since we want to study crack propagation in the blade's plane, we will be working on a two-dimensional problem and this would not allow us taking into account bending effects. In addition, bending is an important factor in rotating beams and the techniques we will be developing may be expanded to three-dimensions. However, we will focus our attention on a two-dimensional blade, assuming that the effects in the thickness direction may be neglected. The inclusion of bending may draw new and interesting results.

4. The blade can be modeled as a single rotating beam, plate strip with in-plane shear and no out-of-plane shear effects. Actually, eccentricity in the rotating blades can occur if another blade suffers from fracture and fails. This eccentricity due to the loss of mass equilibrium will cause that the other helicopter blades, which were not affected by a propagating crack, to fail catastrophically. In this work, we only consider only in-plane shear of the rotating beam, which is caused either by accelerations that cause torque effect on the blade or by drag forces due to the helicopter translational speed. Out-of-plane shear effects are caused by lift forces which causes bending on the helicopter blades. Since we do not include bending effects in our work, we can safely neglect the out-of-plane shear.

5. Blade is subject to a single-crack and not multi-cracks (Figure 1.8). A typical rotating blade may be subject to more than one crack which may or may not propagate simultaneously. Furthermore, they may even interact with each other. Although this is an important consideration, we will be focusing on single-crack techniques.

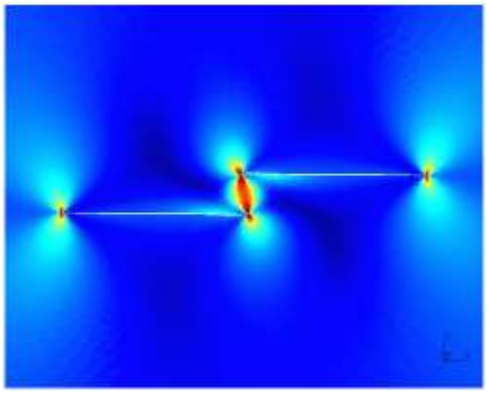

Figure 1.8: Multi-crack interaction.

6. Crack propagation does not consider branching. Dynamic crack branching occurs when the propagating crack departs from its original straight trajectory and curve of split into two or more branches (Figure 1.9). Dynamic crack branching simulations give more realistic crack propagation profiles that can be directly compared to experimental results.

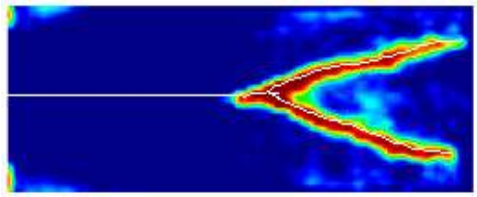

Figure 1.9: Crack branching.

7. Linear Elastic Fracture Mechanics (LEFM) is valid throughout this work. One basic assumption in LEFM is that the size of the plastic zone is small compared to the crack length. The assumption is widely accepted although for rotating blades nonlinear elastic fracture mechanics might produce newer insights.

8. We neglected contact after crack propagates. At crack propagation stage, the split structure behind the crack-tip area may come into contact with each other. This can create an increase in stiffness at the already split structure and therefore will affect remaining life cycles of the studied structure.

1.3: GOALS

1.3.1: OVERALL OBJECTIVES

The following statements summarize the goals of the current work:

1. Add the body force calculation into the Extended Finite Element Method (XFEM).
2. Determine the most critical location for crack propagation in a rotating blade subject to a constant rotational speed.
3. Use XFEM to determine how the crack would propagate at the critical location of a rotating blade using a mixed-mode formulation.
4. Include static fatigue analysis into the current XFEM.

1.3.2: INTELLECTUAL MERIT OF THIS WORK

Nowadays, many aerospace engineers and scientists have the interest in developing robust crack propagation techniques for aerospace structures. The military and private sectors use rotating blade elements in their designs every day. Those who work in this field will greatly benefit from this research because here we propose a more complete *mixed-mode* fatigue analysis in blades rotating at constant rotational velocity. This works as a framework for more complex analysis such as interactions of multi-cracks, branching effects, the use of composite materials, inclusion of wind turbulence, bending effects caused by lift forces, among others. Also, we provide an alternative method to the conventional Finite Element Method (FEM), the XFEM which runs does not require remeshing after each crack propagation step; thus, decreasing computational cost. Finally, with this model, experimental researchers may use our computational model to obtain initial blade manufacturing prototyping parameters.

1.3.3: BROADER IMPACT OF THIS WORK

This work will enrich the field of fracture mechanics, allowing young engineers and/or scientists to learn these newer techniques and putting them a step ahead of the current trend of technology in fracture mechanics. This will have a positive influence over the Hispanic community, as it will encourage young Hispanic scientists to continue to contribute to the field of crack propagation and fatigue analysis of aerospace structures.

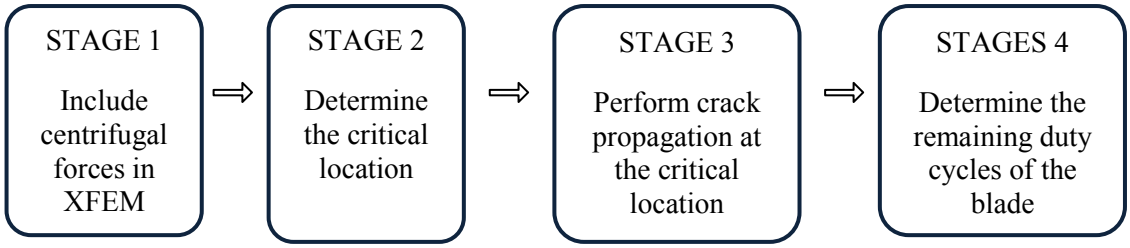

Figure 1.10: Proposed general approach for this work.

1.4: APPROACH

Figure 1.10 illustrates the approach for this work. We used LEFM and XFEM to predict the remaining duty cycles of a rotating blade at a constant speed. In order to accomplish this task, we divided the work in four stages, shown in Figure 1.10. We compared and/or validated all our results against those obtained by ANSYS Workbench [11], and Bordas et al. [12-16].

1.4.1: STAGE 1: BODY FORCE CALCULATION

First, we included the body force calculation into the extended finite element formulation. We used the weak form of the blades' equations of motion and discretize them using both the standard and the enriched shape functions. This gave us the discretized body force term that we implemented it in the code. The MATLAB-based [17] program did the preprocessing, processing and post processing. Once the XFEM code was ready, validated it against theoretical results of one-dimensional case and reproduced some results available in the literature.

1.4.2: STAGE 2: DETERMINE CRITICAL LOCATION

Figure 1.11 illustrates how we determined the critical location of the blade. There are two parts to this stage: (i) semi-analytically via XFEM determine the critical location, (ii) verify the location using ANSYS Workbench with LS-DYNA as explicit solver. We located a single-edged crack at various locations, as shown in Figure 1.11, and determined the stress and displacement profiles which helped us in identifying the critical location.

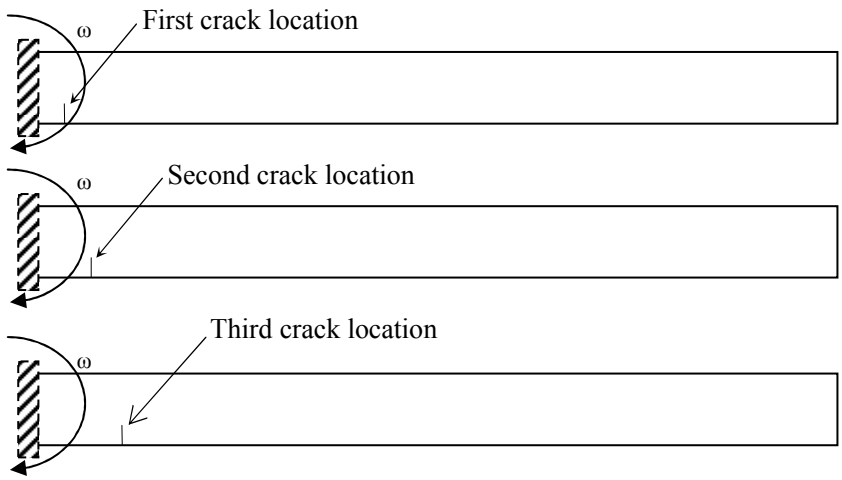

Figure 1.11: Schematic of crack indentation procedure.

1.4.3: STAGE 3: CRACK PROPAGATION AT THE CRITICAL LOCATION

XFEM is a numerical technique that enables the approximation of non-smooth solutions with optimal accuracy. This is achieved by a local enrichment of the approximation space such that the special solution properties are considered appropriately. We added into the XFEM mixed-mode formulation in order to better represent the crack propagation and fatigue analysis. Thus, we obtained *mode I* and *mode II*, and *mixed-mode* (*I* and *II*) Stress Intensity Factor (SIF) for a crack being localized along the entire blade profile.

1.4.4: STAGE 4: FATIGUE AT THE CRITICAL LOCATION

For the static fatigue analysis, we used the Goodman criterion (widely used) to determine the equivalent fatigue stress and thus determine the remaining static life cycles. Finally, we determined the remaining duty cycles of the blade until crack has fully propagated.

1.5: THESIS OUTLINE

Figure 1.12 shows the general thesis outline for this work. *Chapter 1* provides a complete understanding of what is the problem we plan to solve and what is the motivation behind it. *Chapter 2* provides the literature survey of previous works as related our problem and their drawbacks. This chapter also explains how we plan to include mixed-mode fracture analysis using XFEM. In *Chapter 3*, we explain one-dimensional applications of XFEM. *Chapter 4* provides the two-dimensional applications of XFEM. Lastly, in *Chapter 5* we conclude and give ideas on how to further expand this work.

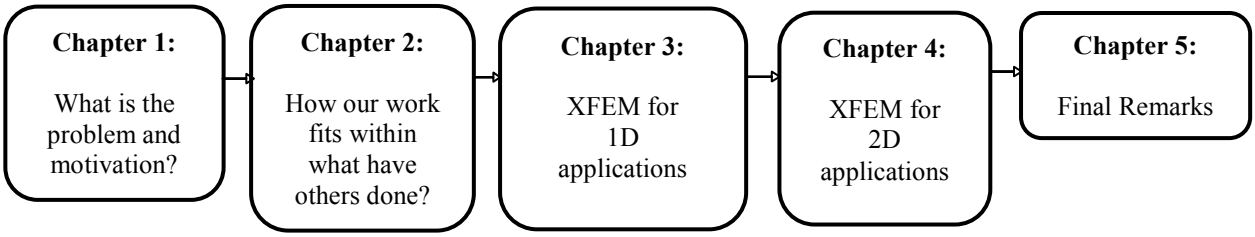

Figure 1.12: Thesis outline.

CHAPTER 2: MIXED-MODE CRACK PROPAGATION USING XFEM

In the classical finite element method (FEM), it is necessary to refine the mesh near the crack tip and thus remeshing is a must even after crack propagation. Hence, the FEM is computationally cumbersome. However, some of the newer techniques, such as the extended finite element method (XFEM), do not require remeshing to predict crack propagation. In the XFEM, the finite element formulation is enriched by the crack tip asymptotic displacements and by a Heaviside function to account for discontinuity in the displacement. In this chapter, we will discuss previous work done by other researchers and how our work will bring contribution to the field.

2.1: FROM FEM TO XFEM

2.1.1: EARLY STAGES OF FEM IN COMPUTATIONAL FRACTURE MECHANICS

The classical, overall objective of fracture mechanics is the determination of the rate of change of the shape of an existing crack [18]. The fundamental question is: will it propagate under given loading and environmental conditions, and, if it does propagate, at what rate and into what configuration? The traditional role of computational fracture mechanics (CFM) would be to find the *Mode I* stress intensity factor (SIF) and its rate with respect to crack length. Most traditional approaches require tens-of-thousands of degrees-of-freedom (DOF) and tons of computing time, making the analysis not practical and/or very costly [19].

If the material behavior is linear and some geometrical restrictions are met, the field solution becomes straightforward with analytical or traditional computational techniques [20]. However, when the material and geometric behavior is nonlinear, the solution is severely limited and traditional numerical approaches become even more computationally expensive [21].

There are currently two main computational approaches: (i) those that do not require spatial Discretization with continuous element of volume such as meshfree methods [22], and those that require discretization but modify the mesh to conform to evolutionary geometry of the crack such as *adaptive FEM* [23]. Adaptive FEM approaches permit completely arbitrary

geometry of both structure and cracks by updating the mesh to conform to the evolving crack geometry. This approach relies on current state-of-the-art FE formulations for the solution function, and in the advance technology in automatic surface and volume mesh generation and in mapping state information from old to new mesh segments. Simulation of crack growth is more complicated than many other applications of computational mechanics because the geometry of the structure evolves during the simulation [24]. For this reason, we prefer a geometric description of the body that is independent of any numerical discretization and can be maintained and updated as part of the simulation process.

On a non-geometrical approach, the material stiffness is appropriately degraded locally to mimic the displacement discontinuity created by a crack, while we keep unchanged the underlying geometry and the mesh models [25]. The kinematic approach is a FE method in which crack representation is embedded in the local finite element approximants, and consequently appears as changes in the strain-displacement matrix, or in the Jacobian.

2.1.2: CHOESIVE ZONES AND XFEM

The goal of this task will be to develop advanced fracture techniques as alternative to the cohesive zone model (CZM) techniques into the existing fracture mechanic's models in commercially available finite element codes [26-32]. A more comprehensive tool consisting of application of advanced fracture models could increase the survivability envelope and speed up the development process of new rotating blades. Cracking is a major cause of structural degradation, which is a primary source of costly repair work on metal structures.

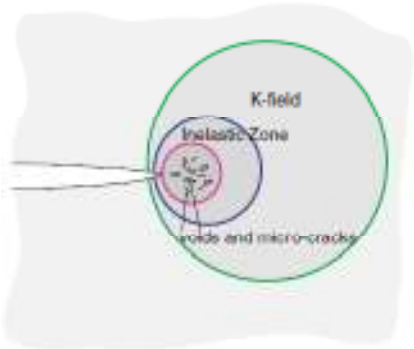

Figure 2.1: Schematic representation of crack tip zones with different material response characteristics.

A realistic fracture model that is physics-based and is adaptable simultaneously to experimental calibration and numerical implementation remains elusive. A schematic drawing is shown in Figure 2.1 to describe three regions at the crack tip where different classes of material responses are dominant. The outer-ring represents the so-called *K*-field and relies on the classical approach based on linear elastic fracture mechanics (LEFM), where the material behavior is linear and stress and strain fields can be determined with a single parameter, typically the stress intensity factor or energy release rate. The intermediate ring is dominated by inelastic effects, e.g., the Hutchinson-Rice-Rosengren (HRR) field [33, 34] where the inelastic response is incorporated. For the inner ring, which is very close to the crack tip, the microstructure of material, e.g., distribution of microcracks and voids will significantly influence the material response due to effects such as void nucleation. In continuum mechanics, the Gurson model [35] successfully incorporates these effects into the constitutive model for ductile materials, however, the large number of parameters that must be calibrated pose a strong challenge for using the model widely. There are a few shortcomings with the above-referenced approaches. First, whether only LEFM model is used to describe a crack tip field or more complicated phenomena incorporated, an external criterion is required for the crack to propagate, and the crack propagation direction is also imposed. Second, phenomena such as fracture instability (which is not yet thoroughly understood), cannot be simulated with a purely phenomenological model. Third, crack branching and fragmentation that usually occur in impact loading events cannot be properly simulated. Finally, the classical approaches require preexisting, crack-like flaws. The nucleation of voids can be treated in Gurson model; however, as explained above, the wide usage of this model remains problematic.

Xu and Needleman [36, 37] investigated dynamic behavior of fast crack growth in brittle solids and demonstrated that the model is capable of simulating many dynamic fracture phenomena such as crack branching, dependence of crack speed on impact velocity, and abrupt crack arrest. However, a consequent drawback with a higher initial stiffness is that smaller elements and smaller time step are required to produce stable results. Camacho and Ortiz [38] investigated damage in brittle materials. Simulation of severe fragmentation under high velocity impact loading was carried out, in which thermal effects and rate dependence were also considered. Park et al. [39] proposed a generalized potential-based CZM, which was largely motivated by the fact that the existing potential-based CZMs, e.g., Xu and Needleman's model [36], do not successfully handle mixed-mode fracture with different Mode-I and Mode-II fracture

energies. CZMs such as Xu and Needleman's model [36] are unable to adjust initial stiffness slope, which is critical in controlling artificial compliance. The generalized potential for mixed-mode fracture, called the Park-Paulino-Roesler potential, allows are different fracture energies in *mode I* and *mode II* [39]. This versatile model is capable of characterizing different fracture energies, considering different cohesive strengths, and describing various material softening behaviors in order to represent a wide range of material failure responses.

Standard methods such as element deletion or remeshing, although easy to use and implement, are not robust tools for this type of simulation essentially because they do not enable one to assess local energy conservation. Standard cohesive zone models behave much better when the crack's path is known in advance, but are difficult to use when the crack's path is unknown. The simplest method which consists in placing the cohesive segments along the sides of the finite elements leads to crack trajectories which are mesh-sensitive. The adaptive cohesive element formulation, which adds new cohesive elements when the crack propagates, is shown to have the proper energy conservation properties during remeshing. An excellent alternative to these methods is the growing XFEM which is considered a good candidate for the simulation of complex dynamic crack propagation.

2.1.3: WHY USE XFEM?

Some advantages of XFEM is that we do not need to conform the finite element mesh to the internal boundaries (cracks, material interfaces, voids, etc.), and hence a single mesh suffices for modeling as well as capturing the evolution of material interfaces and cracks in two-and three-dimensions [40]. The main advantages are that we retain the finite element framework (sparsity and symmetry of the stiffness matrix), and use a single-field variational principle. The extended finite element method (XFEM) was developed by Ted Belytschko [41] to help alleviate the shortcomings of the finite element method and has been used to model the propagation of various discontinuities: strong (cracks) and weak (material interfaces). The idea behind XFEM is to retain most advantages of meshfree methods while alleviating their negative sides. The extended finite element method was developed to ease difficulties in solving problems with localized features that are not efficiently resolved by mesh refinement. One of the initial applications was the modeling of fractures in a material. In this original implementation, discontinuous basis functions are added to

standard polynomial basis functions for nodes that belonged to elements that are intersected by a crack to provide a basis that included crack opening displacements. A key advantage of XFEM is that in such problems the finite element mesh does not need to be updated to track the crack path. Subsequent research has illustrated the more general use of the method for problems involving singularities, material interfaces, regular meshing of microstructural features such as voids, and other problems where a localized feature can be described by an appropriate set of basic functions.

Simulating the propagation of cracks using traditional finite element methods is challenging because the topology of the domain changes continuously. Although FEM has evolved to new applications [42], reducing computational costs due to remeshing procedures in FEM is a major concern [43]. In classical FEM, remeshing is done at each crack propagation step, thus making the numerical simulations computationally costly.

Moës et. al [44] used XFEM to create a technique for simulating crack propagation without remeshing the domain. In XFEM, if an adequate initial mesh in relation with the crack size is constructed, remeshing is not needed for each propagation step. When no meshing is required, this results is great computational saving. XFEM has also been combined with other techniques to increase performance and accuracy [45] and has been used in combination with Level Set methods to track the moving discontinuity sets [13]. However, the XFEM approach carries its own technical challenges [46]. It is important to highlight that current XFEM involves using modern remeshing techniques to further enhance the solution without affecting the computational cost [15, 47].

2.2: CRACK PROPAGATION IN XFEM

Since XFEM is based on the theory of fracture mechanics, let us proceed to highlight the most important aspects if Linear Elastic Fracture Mechanics (LEFM) used throughout this work. The objective of Fracture Mechanics analysis is to determine if small flaws, or cracks, will grow into large enough cracks to cause the component to fail catastrophically. Figure 2.2 shows the three modes of fracture, from which we will only focus on mode I and mode II. Let us assume: (i) the blade remains in the elastic regime everywhere even during crack propagation, (ii) small-strain yielding conditions prevail in the vicinity of the crack front, (iii) the material is considered

isotropic linear elastic with temperature-independent properties, (iv) and the simulations may be carried out under the assumptions of the linear elastic fracture mechanics (LEFM).

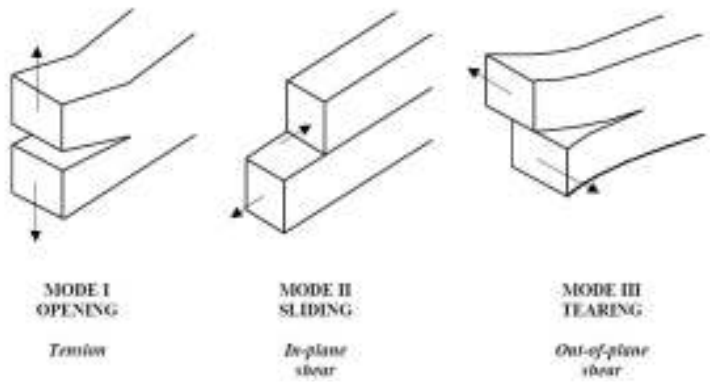

Figure 2.2: Modes of fracture.

2.2.1: MIXED-MODE ANALYSIS USING XFEM

Many researchers have used mixed-mode fracture mechanics [48-52]. The main drawback, as previously mentioned, is the remeshing. Recently, there is a growing interest to add mixed-mode fracture mechanics in XFEM [53-55]. Also, XFEM's mixed-mode analysis has been successfully incorporated into ABAQUS. Xu and Yuan [56] used XFEM using ABAQUS software to simulate fatigue crack propagation under mixed-mode loading conditions. Others have compared XFEM using experimental test data to study three-dimensional problems [57]. Ayhan [57] used tetrahedral elements to simulate an inclined embedded penny-shaped crack in a large medium under uniform tensile load. He used ANSYS™ and FRAC3D to obtain numerical simulation. His results were compared to experimental results obtained in literature. Still, other works concerning crack propagation in composite materials have being made using XFEM [58, 59]. Work done by Mohammadi and Motamedi consisted in two-dimensional dynamic simulation analysis of cracks in orthotropic media using XFEM. In this work, mixed-mode fracture analysis was determined based on evaluation of the *J*-integral. His numerical results show that this approach was not sensitive to the effects of different time-steps or Gauss points. Also, the values of the *J*-integral and SIF become independent from the domain size. Finally, XFEM have evolved into the area of bio-

engineering [60]. In Budyn and Hoc work, they modeled multiple crack growth in cortical bone under pure tension using XFEM. Now, work has being done not only to facilitate meshing procedures within a finite element analysis, but to better explain XFEM theory and its applications [14, 61].

Although the key advantage of XFEM in crack propagation problems arises when the finite element mesh does not need to be updated to track the crack path, there is no work for rotating structural elements in two-dimensions. Our work presents XFFEM crack propagation in two-dimensions when applied a constant rotational velocity in the structure.

2.2.2: STRESS INTENSITY FACTORS

We calculate the stress intensity factors for modes I and II as follows:

$$K_I = C_I\, \sigma_{yy}\sqrt{\pi a} \tag{2.1}$$

$$K_{II} = C_{II}\, \sigma_{xy}\sqrt{\pi a} \tag{2.2}$$

where C_I and C_{II} is the dimensionless quantity accounting for the plate/specimen geometry and relative crack size for mode I and mode II, respectively; a is the crack length; σ is the stress (σ_{xx}, σ_{xy}) if no crack were present; and K_I and K_{II} is the stress intensity factors for modes I and II, respectively. In this work, *mode I* static fracture analysis is taken into consideration because at a constant rotational velocity, the blade would feel a tension loading. Therefore, *mode I* SIF is a dominant factor on our crack propagation analysis. Figure 2.3 shows how we calculate C_I [62]. We define the critical SIF for modes I and II, as follows:

$$K_{Ic} = C_I\, s_y\sqrt{\pi a} \tag{2.3}$$

$$K_{IIc} = \frac{\sqrt{3}}{2} K_{Ic} \tag{2.4}$$

where K_{Ic} is a material property and S_y is the yield stress of the material.

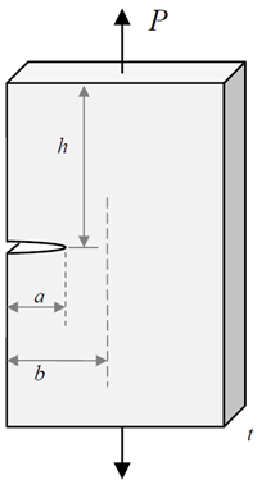

$$C_I = 0.265\,(1-\alpha)^4 + \frac{0.857 + 0.265\,\alpha}{(1-\alpha)^{1.5}}$$

$$C_{II} \approx 1$$

$$\alpha = \frac{a}{b}$$

Figure 2.3: Dimensionless quantity accounting for the plate/specimen geometry and relative crack size for mode I.

2.2.3: MARGIN OF SAFETY

There are cases where the crack is not only subjected to tensile stresses, but also to in-plane shear stresses. When a crack is exposed to both tension and shear stresses, this leads to mixed mode cracking, *mode I* and *mode II*. In the literature, we find various mixed mode criteria for crack growth based on experimental data. The following is a common mixed-mode criterion for static fracture [63]:

$$f = \sqrt{\left(\frac{K_I}{K_{Ic}}\right)^2 + \left(\frac{K_{II}}{K_{IIc}}\right)^2} \qquad \textbf{(2.5)}$$

where f is a nondimensional quantity that has values between 0 and 1. What this means is that the crack will not propagate if $0 < f < 1$; crack initiation occurs when $f = 1$. The margin of safety is:

$$MS = 1 - f \qquad \textbf{(2.6)}$$

If we want to determine the effective SIF for mixed-mode formulation, we may use the following relationship:

$$K_{\text{eff}} = K_{Ic}\, f \tag{2.7}$$

2.2.4: CRACK PROPAGATION LAW

When we talk about crack propagation we are trying to simulate how a crack will induce in a system. The most important event is that of identifying the direction of crack propagation because the crack propagates from one point to another (a step-by-step procedure). In this work, the maximum circumferential stress (hoop stress) criterion is used to determine crack's direction for propagation. The propagation direction is computed such that in the direction $\theta = \theta_c$ the circumferential stress $\sigma_{\theta\theta}$ is the maximum. Using Figure 2.4 and the analytical expression of the stress and displacements fields for *mode I* and *mode II* [64], the hoops stress may be expressed as follows:

$$\sigma_{\theta\theta} = \frac{1}{4}\frac{K_I}{\sqrt{2\pi r}}\left[3\cos\frac{\theta}{2} + \cos\frac{3\theta}{2}\right] + \frac{1}{4}\frac{K_{II}}{\sqrt{2\pi r}}\left[-3\sin\frac{\theta}{2} - 3\sin\frac{3\theta}{2}\right] \tag{2.8}$$

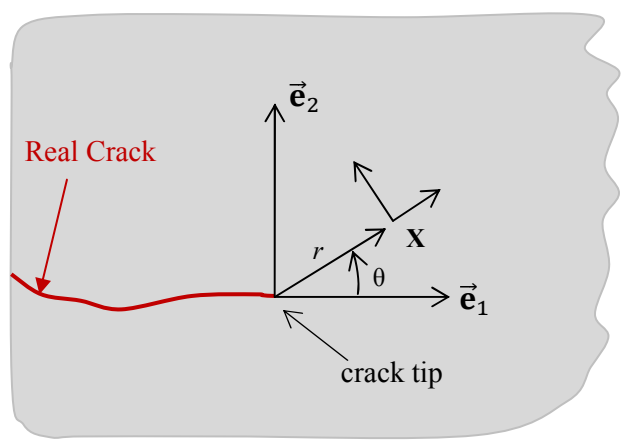

Figure 2.4: Polar coordinate system associated to the crack tip.

The critical angle for propagation direction (details shown in Appendix A.5):

$$\theta_c = 2\tan^{-1}\left[\frac{-2\left(\frac{K_{II}}{K_I}\right)}{1+\sqrt{1+8\left(\frac{K_{II}}{K_I}\right)^2}}\right] \tag{2.9}$$

2.2.5: ENERGY RELEASE RATE

The theories and laws of the linear elastic fracture mechanics (LEFM) can only be applicable to materials which behave in a linear elastic manner. But all the materials do not follow the same rule and specially the ductile materials, like steel and titanium. In ductile materials due to increase in load, a plastic zone develops behind the crack tip which might be of the same order of magnitude as the crack size. Thus, in such a case as the load increases the crack size increases, at the same time the plastic zone increases, which increase the plastic energy dissipation. Hence, the fracture resistance of the material also increases with increasing crack size. Therefore it was necessary to take into account plasticity effects in evaluating the fracture strength of the material.

In order to take into account these effects, Rice [65] developed a way to compute the energy release rate, the so called *J*-integral. The *J*-integral also known as conservation integral represents a way to compute the strain energy release rate for the material where the crack tip deformation is such that it does not obey linear elastic laws. The approach is to identify a line integral which has the same value for all integration paths surrounding the crack tip. The *J*-integral is related to the stress intensity factors (K_I, K_{II}) for plane stress mixed-mode failure is:

$$J = \frac{K_I^2}{E} + \frac{K_{II}^2}{E} \tag{2.10}$$

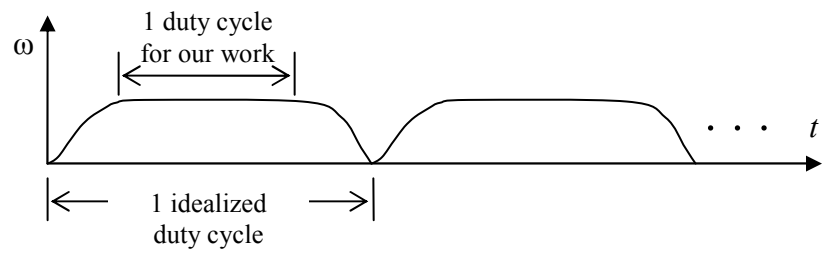

Figure 2.5: Cyclic load representation for this work.

2.3: FATIGUE ANALYSIS

Failure due to fatigue begins with minute cracks at critical areas and propagates under cyclic stresses. Bordas et al [14] developed an XFEM program that simulates a three-dimensional damage tolerance assessment result for a complex aerospace component, the *Boeing 757 EE Access Door*. Fatigue failure may occur at stress levels far below the endurance limit of the material after thousands or millions of cycles [66]. Cyclic stresses are time-dependent functions were the variation is such that the stress sequence repeats itself. Throughout this work we are calculating stresses that result from fluctuating angular velocities, shown in Figure 2.5.

2.3.1: LIFE CYCLES

In order to obtain the remaining duty cycles of a two-dimensional system with an initial crack, using the stress-cycles diagram, we use the following expression [67]:

$$N = \left(\frac{S_{\text{eq}}}{a_0}\right)^{\frac{1}{a_1}} \tag{2.11}$$

where the constants are

$$a_1 = \frac{1}{-3}\log\left(\frac{0.8\,S_{ut}}{S_e}\right), a_0 = \frac{0.8\,S_{ut}}{10^{3a_1}} \tag{2.12}$$

and S_{eq} is equivalent stress from Modified Goodman criterion, S_e is the modified endurance stress, and S_{ut} is the ultimate stress of the material.

In this work, the term *duty cycles* is a general term used in fatigue analysis to determine remaining life cycles of any system. If we wanted to change from *duty cycles* to remaining "helicopter hub revolutions" we have to make the following conversion seen in Eq. (2.13).

$$xx \text{ duty cycles} \left(\frac{\text{flight time(hrs)}}{\text{1duty cycle}}\right)\left(\frac{60 \text{ min}}{\text{1hr}}\right)\left(\text{hub speed in} \left[\frac{\text{rev}}{\text{min}}\right]\right) \qquad \textbf{(2.13)}$$

2.3.2: MODIFIED ENDURANCE LIMIT STRESS

It is unrealistic to expect the endurance limit of a mechanical or structural member to match the values obtained in a laboratory; therefore, Joseph Marin identified factors that quantified the effects of surface condition, size. loading, temperature, and miscellaneous items [68].

$$k_\infty = k_l \, k_t \, k_{sr} \, k_r \, k_g \, k_e \qquad \textbf{(2.14)}$$

where k_l is the loading factor (=1), k_t is the temperature factor (=1), k_{sr} is the surface finish factor (=1), k_r is the reliability of the probability of survival factor (=0.753), k_g is the gradient size factor (=1), and k_e is miscellaneous factor (=0.99). Hence, the endurance limit will be:

$$S_e = k_\infty \, S_e' \qquad \textbf{(2.15)}$$

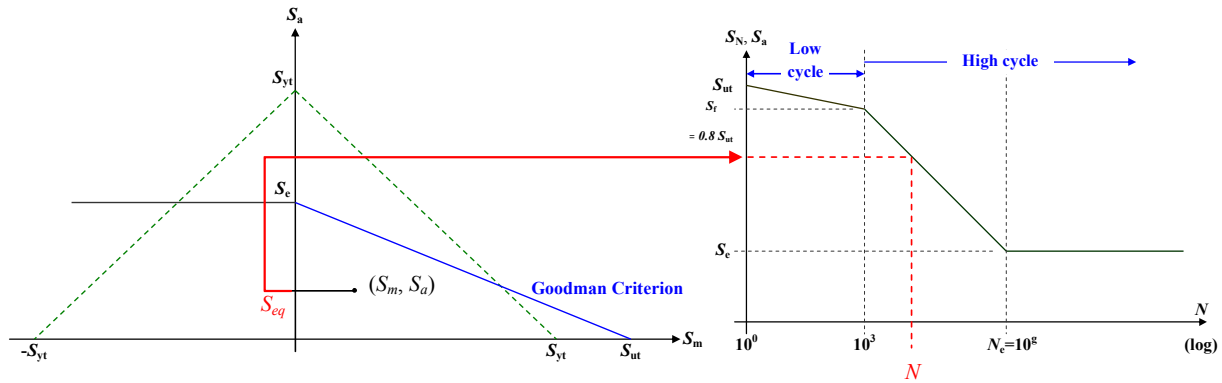

Figure 2.6: Determine life cycle for static fatigue analysis.

2.3.3: GOODMAN CRITERION

Among the all fatigue theories, the Modified Goodman theory is the one widely used [68]. Fatigue equivalent stress can be computed as follows:

$$S_{eq} = \frac{S_a}{1 - \frac{S_m}{S_{ut}}} \tag{2.16}$$

where S_a (= $\eta_{sf}\,\sigma_a$) is the alternate von Mises stress, S_m (= $\eta_{sf}\,\sigma_m$) is the mean von Mises stress, η_{sf} is the factor of safety (=1.25). Figure 2.6 shows how we calculate remaining life for static fatigue analysis. This will be the initial value for fatigue analysis, as crack propagates.

2.3.4: FATIGUE ANALYSIS

In order to understand crack propagation fatigue analysis, we need to explain crack growth rate *(da/dN)*. Crack growth rate is the change in crack size with respect to the change in life cycles. Figure 2.7 shows a superpose plot of different stress range plotted on a Log-Log scale. We can identify three important regions in the plot, these are very important to understand especially when the equations derived from *Region II* are related to LEFM.

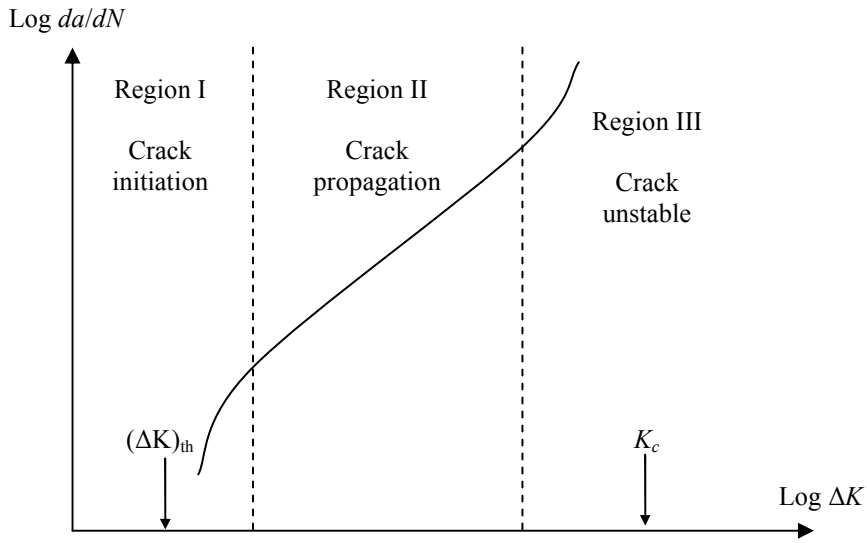

Figure 2.7: *da/dN* plotted on loglog coordinates for a metallic alloy.

If we assume that a crack is discovered early in *Region II*, the crack growth can be approximated by the *Paris equation*, which is of the form [69]

$$\frac{da}{dN} = A\,(\Delta K_{\text{eff}})^n \tag{2.17}$$

where A and n are empirical material constants and we find these values in Table 1.3. In order to obtain ΔK_{eff}, first consider the stress to be fluctuating between the limits of σ_{min} and σ_{max}, where the stress range is defined as $\Delta\sigma = \sigma_{max} - \sigma_{min}$. Hence,

$$\Delta K_{\text{I}} = C_I\,\Delta\sigma_{xx}\sqrt{\pi a}, \quad \Delta K_{\text{II}} = C_{II}\Delta\sigma_{xy}\sqrt{\pi a} \tag{2.18}$$

Using Eq. (2.5)

$$\Delta f = \left(\frac{\partial f}{\partial K_I}\Delta K_{\text{I}} + \frac{\partial f}{\partial K_{II}}\Delta K_{\text{II}}\right) \tag{2.19}$$

Hence, for mixed-mode,

$$\Delta K_{\text{eff}} = K_{Ic}\,\Delta f \tag{2.20}$$

For mixed-mode, the Paris Law is:

$$\Delta N_f = \int_{a_i}^{a_f} \frac{da}{A\,(\Delta K_{\text{eff}})^n} \tag{2.21}$$

and for pure mode one, we have the Paris Law reduces to:

$$\Delta N_f = \int_{a_i}^{a_f} \frac{da}{A\left(C_I\,(\sigma_{\max} - \sigma_{\min})\,\sqrt{\pi a}\right)^n} \tag{2.22}$$

where a_i is the initial crack length, a_f is the final crack length corresponding to failure, ΔN_f is the number of duty cycles to produce a failure after the initial crack if formed. Important to note that the geometric constant C_I may vary depending on the ratio α discussed in Figure 2.3. Also, $\Delta\sigma$ are the maximum and minimum applied stresses for every cycle.

Figure 2.8 shows an algorithm suggested Reemsnyder [1] which we used in order to obtain the total number of duty cycles on your system. For the first propagation step, a_i and a_f are known. Transitional crack length is a material based property that we used to know the crack length that our blade needed for it to fail by fracture and not by yielding. Important to understand the C_I (geometric factor) changes with every propagation step. Also, if $a_f = a_i$ means that crack stopped propagating and blade failed.

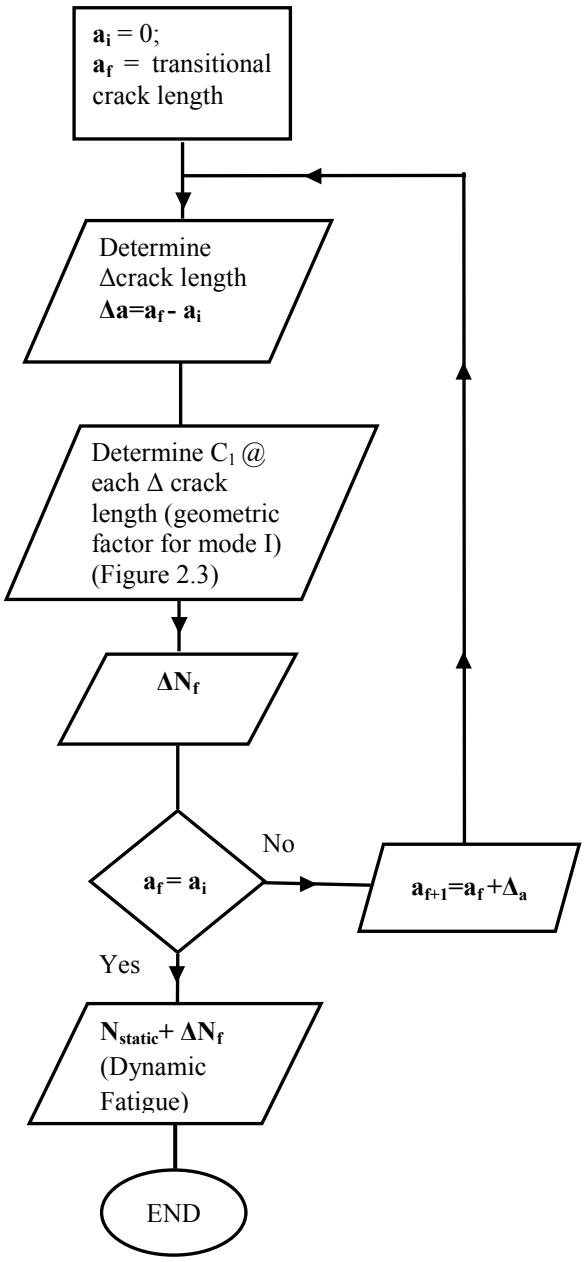

Figure 2.8: Reemsnyder [1] algorithm to determine Dynamic Fatigue Analysis.

CHAPTER 3: 1D XFEM FOR DISCONTINUITIES

Now, we proceed to modify the existent XFEM code by Bordas et al. [12-14, 16]. The code has the ability to run with or without crack. When no crack exists there are no enriched nodes; hence, the code is identical to that of a typical FEM code. Figure 3.1 provides a flowchart on how the code works. As input given by the user, this XFEM code consists in applying any size crack and location of any two-dimensional structure. Also, the user can modify the mesh size as well as the crack propagation steps. One drawback of this code is that it assumes no further contact after crack propagation. In order to better understand the code, we will first explain a one-dimensional example.

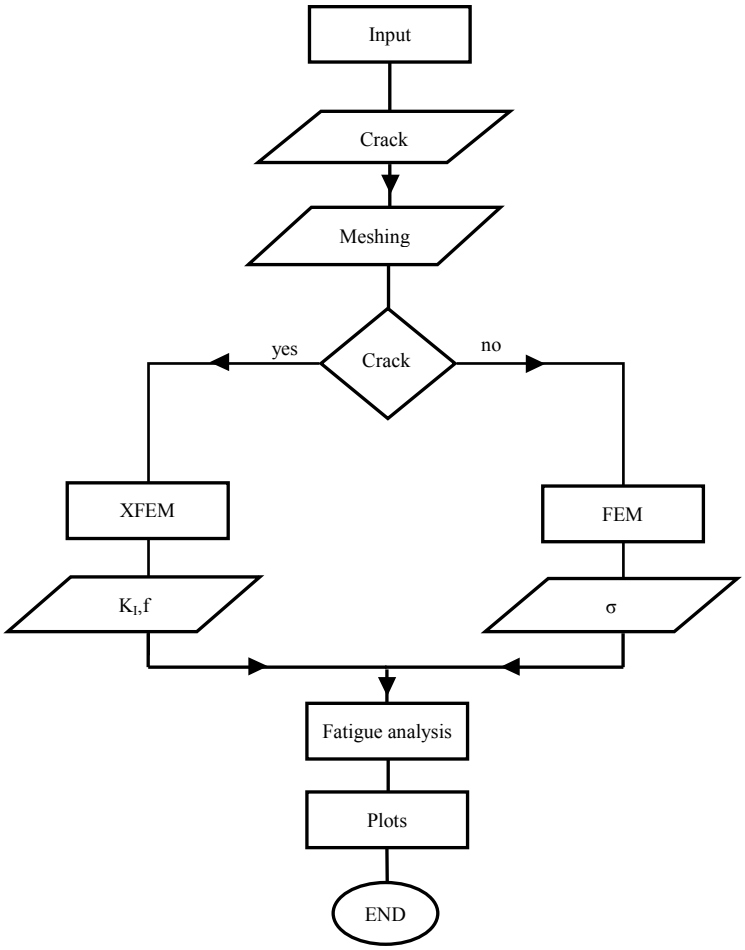

Figure 3.1: General flowchart of code for one-dimensional problem.

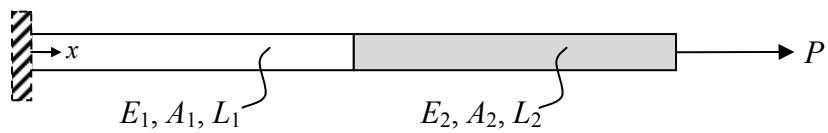

Figure 3.2: One-dimensional elastic bar example with a weak discontinuity.

3.1: WEAK DISCONTINUITY

In order to understand the extended finite element formulation, let us consider a bi-material elastic axial bar example. Throughout the following example we will highlight the main differences between the FEM and XFEM. We plan to solve this problem using one, three and five elements. Three and five element results will include: exact solution, standard XFEM solution and *modified* XFEM solution (discussed within example). Figure 3.2 shows an isotropic elastic axial bar fixed at $x = 0$ and subject to a point load P (= 1) at $x = L$ (the tip). The geometric properties are $L_1 = 0.5$ and $L_2 = 0.5$; and the mechanical properties are $E_1 = 1$ and $E_2 = 5$. The material interface is assumed $x_b = 0.5$ because it is the location of the discontinuity. The cross-sectional areas $A_1 = 1$ and $A_2 = 1$. We are interested to determine the displacement profile using XFEM and then compared against the traditional FEM displacements values.

3.1.1: ONE-ELEMENT SOLUTION USING STANDARD XFEM

Displacement Profile

The displacement profile for a one-dimensional elastic axial bar is:

$$\begin{aligned} U(x,y,z) &= u(x) \\ V(x,yz) &= 0 \\ W(x,y,z) &= 0 \end{aligned} \tag{3.1}$$

In the finite element method, we assume a linear axial displacement profile as follows:

$$u(x) = N_1 u_1 + N_2 u_2 \tag{3.2}$$

where u_1 and u_2 are the nodal displacements and $N(x)$'s are the shape functions, defined as

$$N_1(x) = 1 - \frac{x}{L_e}, \quad N_2(x) = \frac{x}{L_e} \tag{3.3}$$

In the extended finite element method we approximate the displacement field using enriched nodes. We identify u_1 and u_2 as the standard nodal displacements and a_1 and a_2 as the enriched nodal displacements, seen in Figure 3.3.

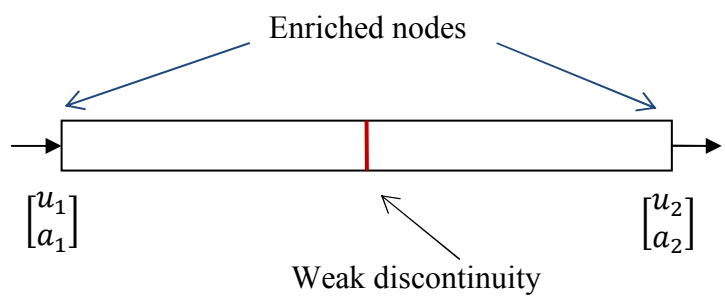

Figure 3.3: One-element schematic example with a weak discontinuity.

For each enriched degree of freedom we will have an associated enriched shape function. Now, the XFEM displacement approximation for this example will be:

$$u(x) = N_1 u_1 + N_2 u_2 + N_3 a_1 + N_4 a_2 \tag{3.4}$$

where u_1 and u_2 are displacements due to regular degrees of freedom and a_1 and a_2 are nodal displacements due to the enriched degrees of freedom. Also, N_1 and N_2 are the standard shape functions, and N_3 and N_4 are the enriched shape functions, which are defined as follows:

$$N_3(x) = N_1 \left(\underbrace{|\xi(x)| - |\xi(x_1)|}_{\substack{\text{Enriched function in} \\ \text{one-dim}}} \right) = N_1 \Psi_1 \tag{3.5}$$

$$N_4(x) = N_2\left(\underbrace{|\xi(x)| - |\xi(x_2)|}_{\substack{\text{Enriched function in} \\ \text{one-dim}}}\right) = N_2\Psi_2 \tag{3.6}$$

where

$$\xi(x) = |x - x_b| \tag{3.7}$$

In the above equation $\xi(x)$ is the level set function for one-dimensional problem, x_b is the location of the interface from the left end (we assumed $x_b = 0.5$), x_1 is the location at the fixed end (x_1=0), and x_2 is the location at the tip ($x_2 = 1$). Hence, the enriched shape functions for our example are:

$$N_3(x) = \left(1 - \frac{x}{L_e}\right)(|x - 0.5| - |0 - 0.5|) \tag{3.8}$$

$$N_4(x) = \left(\frac{x}{L_e}\right)(|x - 0.5| - |1 - 0.5|) \tag{3.9}$$

Figure 3.4 shows the plots of the standard and enriched shape functions a one-dimensional axial bar with $x_b = 0.5$. The approximate displacement in matrix form is

$$u(x) = \begin{bmatrix} N_1 & N_2 & N_3 & N_4 \end{bmatrix} \begin{Bmatrix} u_1 \\ u_2 \\ a_1 \\ a_2 \end{Bmatrix} = [N]\{q\} \tag{3.10}$$

where $[N]$ is the XFEM shape function matrix and $\{q\}$ is the XFEM nodal displacement vector. We can write these matrices and vectors as follows:

$$u(x) = \begin{bmatrix} N_{\text{fem}} & N_{\text{enr}} \end{bmatrix} \begin{Bmatrix} q_{\text{fem}} \\ q_{\text{enr}} \end{Bmatrix} \tag{3.11}$$

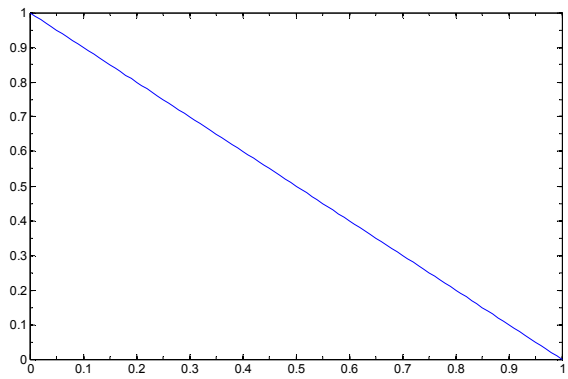

$$N_1(x) = 1 - \frac{x}{L_e}$$

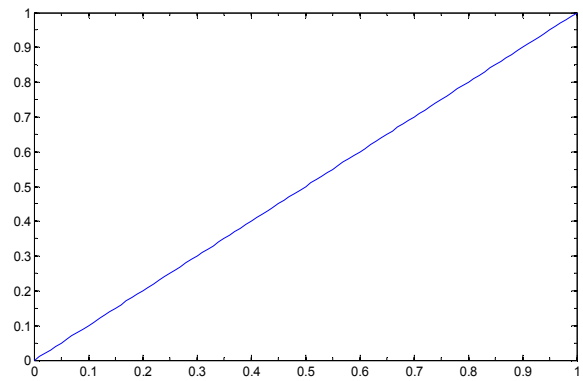

$$N_2(x) = \frac{x}{L_e}$$

(a) Standard shape functions

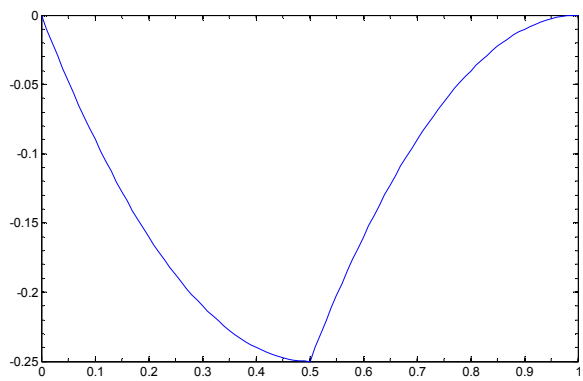

$$N_3(x) = N_1(|\xi(x)| - |\xi(x_1)|)$$

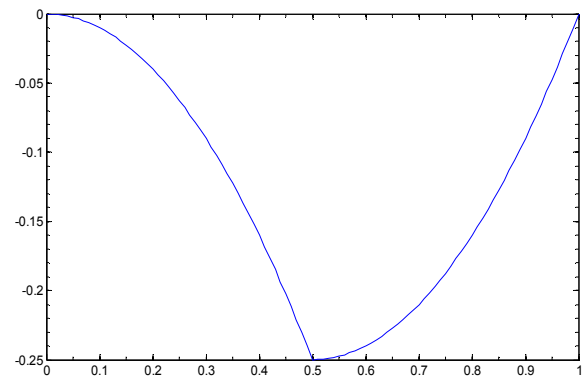

$$N_4(x) = N_2(|\xi(x)| - |\xi(x_2)|)$$

(b) Enriched shape functions

Figure 3.4: Shape functions for one-dim XFEM.

Strains and Stresses

The only nonzero strains for an axial bar are

$$u(x) = [N_{\text{fem}} \quad N_{\text{enr}}] \begin{Bmatrix} q_{\text{fem}} \\ q_{\text{enr}} \end{Bmatrix} \tag{3.12}$$

$$e_{xx} = \frac{\partial U}{\partial x} \quad \rightarrow \quad \varepsilon_{xx} = \frac{\partial u}{\partial x} \tag{3.13}$$

Hence, the XFEM strain approximation is

$$\varepsilon_{xx} = \frac{\partial u}{\partial x} = \frac{\partial N_1}{\partial x} u_1 + \frac{\partial N_2}{\partial x} u_2 + \frac{\partial N_3}{\partial x} a_1 + \frac{\partial N_4}{\partial x} a_2 \tag{3.14}$$

$$\begin{aligned} \varepsilon_{xx} &= \begin{bmatrix} \frac{\partial N_1}{\partial x} & \frac{\partial N_2}{\partial x} & \vdots & \frac{\partial N_3}{\partial x} & \frac{\partial N_4}{\partial x} \end{bmatrix} \begin{Bmatrix} u_1 \\ u_2 \\ a_1 \\ a_2 \end{Bmatrix} = [B]\{q\} \\ &= [\mathbf{B}_{\text{fem}} \quad \mathbf{B}_{\text{enr}}] \begin{Bmatrix} q_{\text{fem}} \\ q_{\text{enr}} \end{Bmatrix} \end{aligned} \tag{3.15}$$

where $[B]$ is the XFEM strain-displacement matrix. Now we calculate the derivatives:

$$\frac{\partial N_1}{\partial x} = -\frac{1}{L_e}, \quad \frac{\partial N_2}{\partial x} = \frac{1}{L_e} \tag{3.16}$$

The derivatives of the enriched shape functions are a bit trickier. First note that the shape functions are

$$\begin{aligned} N_3(x) &= \left(1 - \frac{x}{L_e}\right)(|x - x_b| - |x_1 - x_b|) \\ &= \left(1 - \frac{x}{L_e}\right)(|x - x_b| - |x_b|) \end{aligned} \tag{3.17}$$

$$\begin{aligned} N_4(x) &= \left(\frac{x}{L_e}\right)(|x - x_b| - |x_2 - x_b|) \\ &= \left(\frac{x}{L_e}\right)(|x - x_b| - |L_e - x_b|) \end{aligned} \tag{3.18}$$

For our example, the derivatives of the enriched shape functions with respect to the *x* are:

$$\frac{\partial N_3}{\partial x} = \frac{1}{2} + \left(-2x + \frac{3}{2}\right) \text{Sign}\left[x - \frac{1}{2}\right] \tag{3.19}$$

$$\frac{\partial N_4}{\partial x} = -\frac{1}{2} + \left(\frac{1}{2}\right) \text{Sign}\left[x - \frac{1}{2}\right] \tag{3.20}$$

Hence, the standard FEM strain-displacement matrix $\mathbf{B}_{\text{fem}}$ is

$$\mathbf{B}_{\text{fem}}^{(1)} = \mathbf{B}_{\text{fem}}^{(2)} = \begin{bmatrix} -1 & 1 \end{bmatrix} \tag{3.21}$$

and the enriched XFEM strain-displacement matrix $\mathbf{B}_{\text{enr}}$ is

$$\mathbf{B}_{\text{enr}}^{(1)} = \begin{bmatrix} 2x - 1 & -2x \end{bmatrix} \tag{3.22}$$

$$\mathbf{B}_{\text{enr}}^{(2)} = \begin{bmatrix} -2x + 2 & 2x - 1 \end{bmatrix} \tag{3.23}$$

The XFEM strain-displacement matrix for the second material is found using the procedure. Now, the strains displacement matrices may be calculated as follow:

$$\mathbf{B}^{(1)} = \begin{bmatrix} -1 & 1 & 2x - 1 & -2x \end{bmatrix} \tag{3.24}$$

$$\mathbf{B}^{(2)} = \begin{bmatrix} -1 & 1 & -2x + 2 & 2x - 1 \end{bmatrix} \tag{3.25}$$

We calculate the stresses using the Hooke's Law for isotropic materials:

$$\mathbf{S}^{(1)} = \mathbf{D}^{(1)}\, \mathbf{E}^{(1)} = [\mathrm{E}_1]\, \mathbf{B}^{(1)}\, \mathbf{q}^{(1)} \tag{3.26}$$

$$\mathbf{S}^{(2)} = \mathbf{D}^{(2)}\, \mathbf{E}^{(2)} = [\mathrm{E}_2]\, \mathbf{B}^{(2)}\, \mathbf{q}^{(2)} \tag{3.27}$$

Since we are working with a one-element solution: $\mathbf{q} = \mathbf{q}^{(1)} = \mathbf{q}^{(2)}$. Hence,

$$\mathbf{S}^{(1)} = \mathbf{D}^{(1)}\,\mathbf{E}^{(1)} = [\mathrm{E}_1]\,\mathbf{B}^{(1)}\,\mathbf{q} \tag{3.28}$$

$$\mathbf{S}^{(2)} = \mathbf{D}^{(2)}\,\mathbf{E}^{(2)} = [\mathrm{E}_2]\,\mathbf{B}^{(2)}\,\mathbf{q} \tag{3.29}$$

Discretizing the Equations of Motion

Using the principle of virtual work, our boundary value problem becomes

$$\int_{\Omega} \mathbf{S}^{\mathbf{T}}\,\boldsymbol{\delta}\mathbf{E}\,\mathrm{d}\Omega = \int_{\Omega} \mathbf{f_b}^{\mathbf{T}}\,\boldsymbol{\delta}\mathbf{d}\,\mathrm{d}\Omega + \int_{\Gamma} \mathbf{f_t}^{\mathbf{T}}\,\boldsymbol{\delta}\mathbf{d}\,\mathrm{d}\Gamma \tag{3.30}$$

where **S** is the stress vector, $\mathbf{f_b}$ and $\mathbf{f_t}$ are the body force and external traction vectors, respectively. Discretization of Eq. (3.30) using the XFEM procedure results in a discrete system of linear equilibrium equations:

$$\int_{\Omega} \mathbf{q}^{\mathbf{T}}\,\mathbf{B}^{\mathbf{T}}\mathbf{D}^{\mathbf{T}}\,\mathbf{B}\,\boldsymbol{\delta}\mathbf{q}\,\mathrm{d}\Omega = \int_{\Omega} \mathbf{f_b}^{\mathbf{T}}\,\mathbf{N}\,\boldsymbol{\delta}\mathbf{q}\,\mathrm{d}\Omega + \int_{\Gamma} \mathbf{f_t}^{\mathbf{T}}\,\mathbf{N}\,\boldsymbol{\delta}\mathbf{q}\,\mathrm{d}\Gamma \tag{3.31}$$

For all values of $\boldsymbol{\delta}\mathbf{q}$, we find our stiffness matrix:

$$\mathbf{K} = \int_{\mathrm{S}} \mathbf{B}^{\mathbf{T}}\mathbf{D}^{\mathbf{T}}\,\mathbf{B}\;\mathbf{A}\,\mathrm{d}x \tag{3.32}$$

Now note that because of the discontinuity all integrals must be separated in two domains:

$$\mathbf{K} = \underbrace{\int_{0}^{x_b} \left[\mathbf{B}^{(1)}\right]^{\mathbf{T}}[\mathrm{E}_1\mathrm{A}_1]\mathbf{B}^{(1)}\;\mathrm{d}x}_{\mathrm{K}_1} + \underbrace{\int_{x_b}^{L} \left[\mathbf{B}^{(2)}\right]^{\mathbf{T}}[\mathrm{E}_2\mathrm{A}_2]\,\mathbf{B}^{(2)}\,\mathrm{d}x}_{\mathrm{K}_2} \tag{3.33}$$

where

$$\mathbf{K_1} = \int_{0}^{x_b} \left[\mathbf{B}^{(1)}\right]^{\mathbf{T}}[\mathrm{E}_1\mathrm{A}_1]\left[\mathbf{B}^{(1)}\right]\;\mathrm{d}x$$

$$= \begin{bmatrix} 0.5 & -0.5 & 0.25 & 0.25 \\ -0.5 & 0.5 & -0.25 & -0.25 \\ 0.25 & -0.25 & 0.167 & 0.083 \\ 0.25 & -0.25 & 0.083 & 0.167 \end{bmatrix} \tag{3.34}$$

$$\mathbf{K_2} = \int_{x_b}^{L} \left[\mathbf{B}^{(2)}\right]^{\mathbf{T}} [\mathrm{E}_2\mathrm{A}_2] \left[\,\mathbf{B}^{(2)}\right] \mathrm{d}x \;= \begin{bmatrix} 1 & -1 & -0.5 & -0.5 \\ -1 & 1 & 0.5 & 0.5 \\ -0.5 & 0.5 & 0.3333 & 0.1667 \\ -0.5 & 0.5 & 0.1667 & 0.3333 \end{bmatrix} \tag{3.35}$$

Therefore, the global stiffness matrix for one element solution is

$$\mathbf{K_g} = \begin{bmatrix} 1.5 & -1.5 & -0.25 & -0.25 \\ -1.5 & 1.5 & 0.25 & 0.25 \\ -0.25 & 0.25 & 0.5 & 0.25 \\ -0.25 & 0.25 & 0.25 & 0.5 \end{bmatrix} \tag{3.36}$$

The linear system of equations is:

$$\begin{bmatrix} 1.5 & -1.5 & -0.25 & -0.25 \\ -1.5 & 1.5 & 0.25 & 0.25 \\ -0.25 & 0.25 & 0.5 & 0.25 \\ -0.25 & 0.25 & 0.25 & 0.5 \end{bmatrix} \begin{Bmatrix} u_1 \\ u_2 \\ a_1 \\ a_2 \end{Bmatrix} = \begin{Bmatrix} F_1 \\ 1 \\ 0 \\ 0 \end{Bmatrix} \tag{3.37}$$

We solve this system using the typical finite element approach. Figure 3.5 shows the displacement profile for one-element. The solution matches with the exact solution. We can immediately see the advantage of XFEM, one element is sufficient. FEM would give the same answer but with three elements!

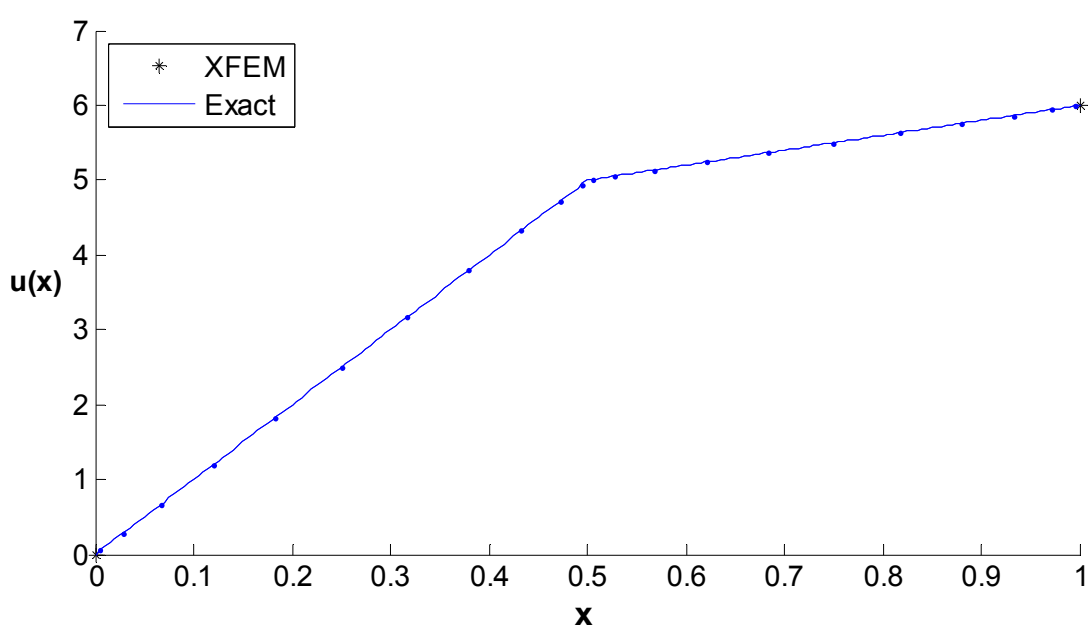

Figure 3.5: One-element displacement profile for weak discontinuity of bimetalic bar.

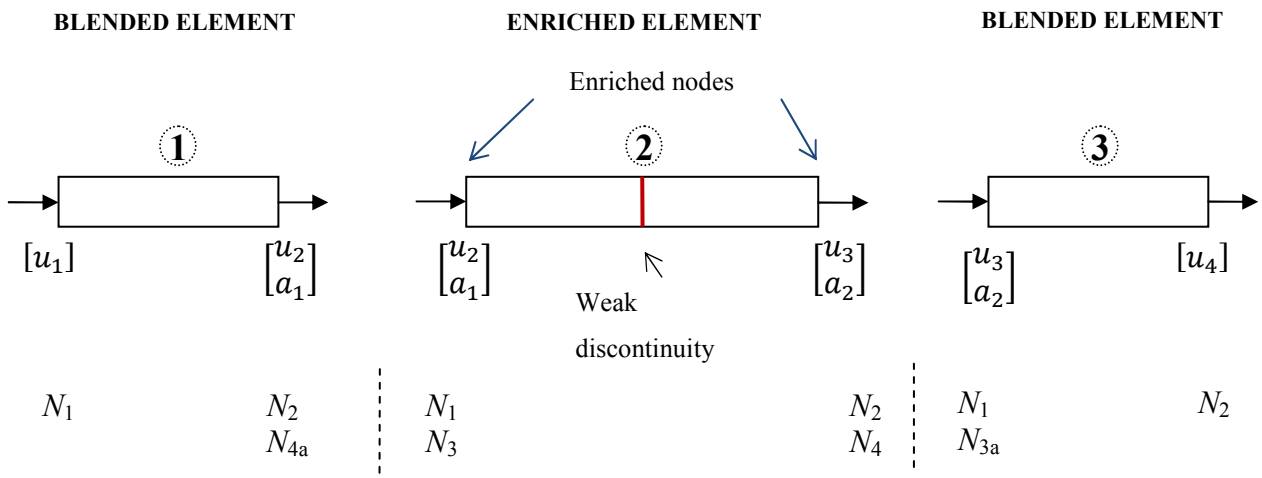

Figure 3.6: Three-element schematic for one-dimensional example with a weak discontinuity.

3.1.2: THREE-ELEMENT SOLUTION USING STANDARD XFEM

Figure 3.6 shows three elements discretization of the bimaterial elastic axial bar example. The geometric properties are $L_1 = L_2 = L_3 = 1/3$; and the mechanical properties are $E_1 = 1$ and $E_2 = 5$. The material interface is assumed $x_b = 0.5$ because it is the location of the discontinuity. The cross-sectional areas $A_1 = A_2 = A_3 = 1$. We express the axial displacement profile as follows:

$$u_1(x) = N_1 u_1 + N_2 u_2 + N_{4a} a_1 \tag{3.38}$$

$$u_2(x) = N_1 u_2 + N_2 u_3 + N_3 a_1 + N_4 a_2 \tag{3.39}$$

$$u_3(x) = N_1 u_3 + N_2 u_4 + N_{3a} a_2 \tag{3.40}$$

where u_1, u_2, u_3, u_4 are the nodal displacements; a_1, a_2 as the enriched nodal displacements; and the shape functions are

$$N_1(x) = 1 - \frac{x}{L_e}, \quad N_2(x) = \frac{x}{L_e}$$

$$N_3(x) = N_1 \left(\underbrace{|\xi(x)| - |\xi(x_1)|}_{\substack{\text{Enriched function in} \\ \text{one-dim}}} \right) = N_1 \Psi_1 \tag{3.41}$$

$$N_4(x) = N_2\left(\underbrace{|\xi(x)| - |\xi(x_2)|}_{\substack{\text{Enriched function in} \\ \text{one-dim}}}\right) = N_2\Psi_2 \tag{3.42}$$

where

$$\xi(x) = |x - x_b| \tag{3.43}$$

In the above equation $\xi(x)$ is the level set function for one-dimensional problem, x_b is the location of the interface from the left end (we assumed $x_b = 0.5\ Le_2$), x_1 is the location at the fixed end (x_1=0), and x_2 is the location at the tip ($x_2 = Le_2$). Hence, the enriched shape functions for our example are:

$$N_3(x) = \left(1 - \frac{x}{L_e}\right)(|x - 0.5L_{e2}| - |0 - 0.5\ L_{e2}|) \tag{3.44}$$

$$N_4(x) = \left(\frac{x}{L_e}\right)(|x - 0.5L_{e2}| - |L_{e2} - 0.5L_{e2}|) \tag{3.45}$$

However, for the blended shape functions for our example are:

$$N_{4a}(x) = \left(\frac{\bar{x}}{L_e}\right)(|\bar{x} - 0.5L_{e2}| - |L_{e2} - 0.5L_{e2}|) \quad \text{where}$$

$$\bar{x} = x - L_{e2} \tag{3.46}$$

$$N_{3a}(x) = \left(1 - \frac{\hat{x}}{L_e}\right)(|\hat{x} - 0.5L_{e2}| - |0 - 0.5\ L_{e2}|) \text{ where}$$

$$\hat{x} = x + L_{e2} \tag{3.47}$$

Figure 3.7 shows the enriched shape functions.

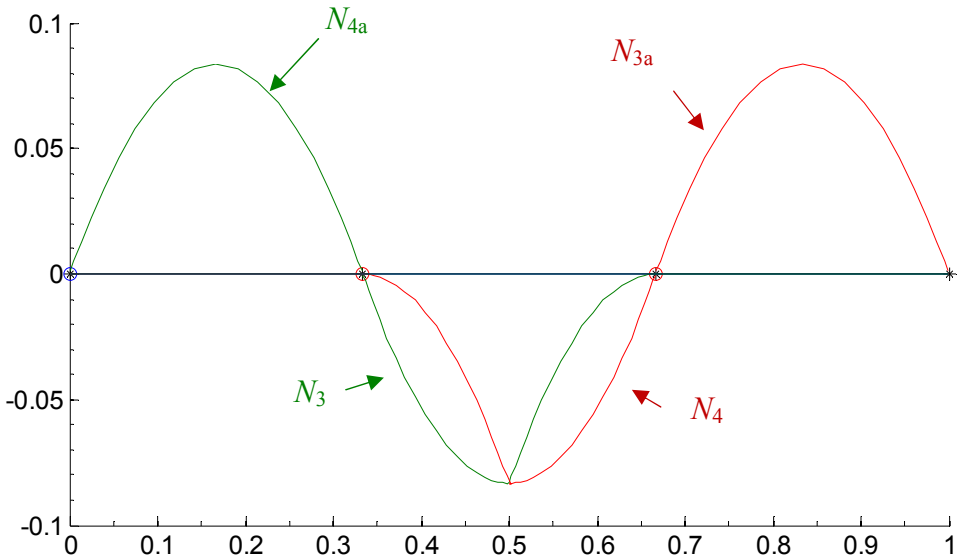

Figure 3.7: Enriched shape functions for a three-element solution using one-dimensional standard XFEM.

The only nonzero strains for an axial bar are

$$\varepsilon_{xx}^{(1)} = \begin{bmatrix} \frac{\partial N_1}{\partial x} & \frac{\partial N_2}{\partial x} & \vdots & \frac{\partial N_{4a}}{\partial x} \end{bmatrix} \begin{Bmatrix} u_1 \\ u_2 \\ a_1 \end{Bmatrix} = \mathbf{B}^{(1)} \begin{Bmatrix} u_1 \\ u_2 \\ a_1 \end{Bmatrix} \tag{3.48}$$

$$\varepsilon_{xx}^{(2)} = \begin{bmatrix} \frac{\partial N_1}{\partial x} & \frac{\partial N_2}{\partial x} & \vdots & \frac{\partial N_3}{\partial x} & \frac{\partial N_4}{\partial x} \end{bmatrix} \begin{Bmatrix} u_2 \\ u_3 \\ a_1 \\ a_2 \end{Bmatrix} = \begin{cases} \mathbf{B}_{\mathbf{1}}^{(2)} \begin{Bmatrix} u_2 \\ u_3 \\ a_1 \\ a_2 \end{Bmatrix}, & x < x_b \\ \mathbf{B}_{\mathbf{2}}^{(2)} \begin{Bmatrix} u_2 \\ u_3 \\ a_1 \\ a_2 \end{Bmatrix}, & x \geq x_b \end{cases} \tag{3.49}$$

$$\varepsilon_{xx}^{(3)} = \begin{bmatrix} \frac{\partial N_1}{\partial x} & \frac{\partial N_2}{\partial x} & \vdots & \frac{\partial N_{3a}}{\partial x} \end{bmatrix} \begin{Bmatrix} u_3 \\ u_4 \\ a_2 \end{Bmatrix} = \mathbf{B}^{(3)} \begin{Bmatrix} u_3 \\ u_4 \\ a_2 \end{Bmatrix} \tag{3.50}$$

We calculate the stresses using the Hooke's Law for isotropic materials:

$$\mathbf{S}^{(1)} = \mathbf{D}^{(1)}\,\mathbf{E}^{(1)} = [\mathrm{E}_1]\,\mathbf{B}^{(1)}\,\mathbf{q}^{(1)} \tag{3.51}$$

$$\mathbf{S}_1^{(2)} = \mathbf{D}_1^{(2)}\mathbf{E}_1^{(2)} = [\mathrm{E}_1]\,\mathbf{B}_1^{(2)}\,\mathbf{q}^{(2)}$$

$$\mathbf{S}_2^{(2)} = \mathbf{D}_2^{(2)}\mathbf{E}_2^{(2)} = [\mathrm{E}_2]\,\mathbf{B}_2^{(2)}\,\mathbf{q}^{(2)} \tag{3.52}$$

$$\mathbf{S}^{(3)} = \mathbf{D}^{(3)}\,\mathbf{E}^{(3)} = [\mathrm{E}_2]\,\mathbf{B}^{(3)}\,\mathbf{q}^{(3)} \tag{3.53}$$

Discretizating of the principle of virtual work, we find our elemental stiffness matrices

$$\mathbf{K}^{(1)} = \int_0^{L_{e1}} \left[\mathbf{B}^{(1)}\right]^{\mathbf{T}} [E_1A_1] \left[\mathbf{B}^{(1)}\right] \mathrm{d}x = \begin{bmatrix} 3 & -3 & 0 \\ -3 & 3 & 0 \\ 0 & 0 & 0.111 \end{bmatrix} \tag{3.54}$$

$$\mathbf{K}_1^{(2)} = \int_0^{x_b} \left[\mathbf{B}_1^{(2)}\right]^{\mathbf{T}} [E_1A_2] \left[\mathbf{B}_1^{(2)}\right] \mathrm{d}x = \begin{bmatrix} 1.5 & -1.5 & 0.25 & 0.25 \\ -1.5 & 1.5 & -0.25 & -0.25 \\ 0.25 & -0.25 & 0.0556 & 0.02778 \\ 0.25 & -0.25 & 0.02778 & 0.0556 \end{bmatrix}$$

$$\mathbf{K}_2^{(2)} = \int_{x_b}^{L_{e2}} \left[\mathbf{B}_2^{(2)}\right]^{\mathbf{T}} [E_2A_2] \left[\mathbf{B}_2^{(2)}\right] \mathrm{d}x = \begin{bmatrix} 3 & -3 & -0.5 & -0.5 \\ -3 & 3 & 0.5 & 0.5 \\ -0.5 & 0.5 & 0.1111 & 0.0556 \\ -0.5 & 0.5 & 0.0556 & 0.111 \end{bmatrix}$$

$$\mathbf{K}^{(2)} = \mathbf{K}_1^{(2)} + \mathbf{K}_2^{(2)} = \begin{bmatrix} 4.5 & -4.5 & -0.25 & -0.25 \\ -4.5 & 4.5 & 0.25 & 0.25 \\ -0.25 & 0.25 & 1.667 & 0.0833 \\ -0.25 & 0.25 & 0.0833 & 1.667 \end{bmatrix} \tag{3.55}$$

$$\mathbf{K}^{(3)} = \int_0^{L_{e3}} \left[\mathbf{B}^{(3)}\right]^{T} [E_2A_3] \left[\mathbf{B}^{(3)}\right] dx = \begin{bmatrix} 6 & -6 & 0 \\ -6 & 6 & 0 \\ 0 & 0 & 0.222 \end{bmatrix} \tag{3.56}$$

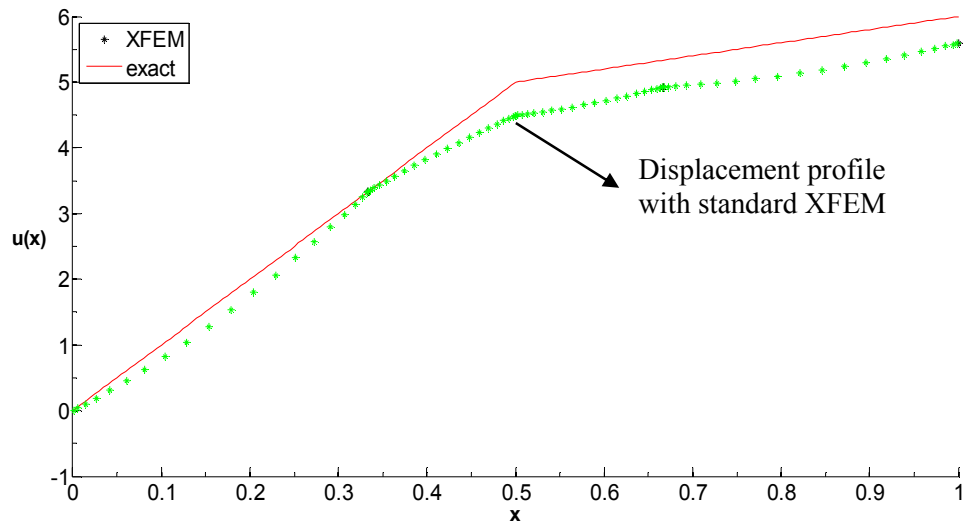

Figure 3.8: Three-element displacement profile for weak discontinuity of bimetalic bar using standard XFEM.

Therefore, the linear system of equations is

$$\begin{bmatrix} 3 & -3 & 0 & 0 & 0 & 0 \\ -3 & 7.5 & -4.5 & 0 & -0.25 & -0.25 \\ 0 & -4.5 & 10.5 & -6 & 0.25 & 0.25 \\ 0 & 0 & -6 & 6 & 0 & 0 \\ 0 & -0.25 & 0.25 & 0 & 0.2778 & 0.0833 \\ 0 & -0.25 & 0.25 & 0 & 0.0833 & 0.3889 \end{bmatrix} \begin{Bmatrix} u_1 \\ u_2 \\ u_3 \\ u_4 \\ a_1 \\ a_2 \end{Bmatrix} = \begin{Bmatrix} F_1 \\ 0 \\ 0 \\ 1 \\ 0 \\ 0 \end{Bmatrix} \tag{3.57}$$

Figure 3.8 shows the three-element displacement profile for weak discontinuity of bimetalic bar. The three-element XFEM solution does not match the exact solution whereas the one-element solution does. The results are quite intriguing but the answer is quite simple. In order to better explain this, we will call the previously used XFEM approach as the standard XFEM and the fix to the problem as the modified XFEM.

3.1.3: THREE-ELEMENT SOLUTION USING MODIFIED XFEM

In order to fix this problem, recall that we assumed the standard XFEM displacement approximation as follows:

$$u(x) = \sum_{I} N_i(x)u_i + \sum_{I^*} N_i(x)\Psi(x)a_i \tag{3.58}$$

where the second term consists on the enriched XFEM elements. In order to better explain this let us consider a two dimensional domain, as shown in Figure 3.9. The problem exists in the blending elements (elements 1 and 3 in the previous example). The conventional FEM elements are not enriched while the enriched XFEM elements are fully enriched and neither one of these elements create unwanted terms. However, blending elements have enriched and not-enriched nodes and this creates unwanted terms in the displacement profile, which will affect the solution. We can interpret this unwanted terms using the standard and enriched shape functions.

$$\begin{aligned} &\sum_{J^*} N_J^*(x) = 1 \quad \textbf{Enriched} \text{ elements} \\ &\sum_{I^*} N_I^*(x) \neq 1 \quad \textbf{Blending} \text{ elements} \end{aligned} \tag{3.59}$$

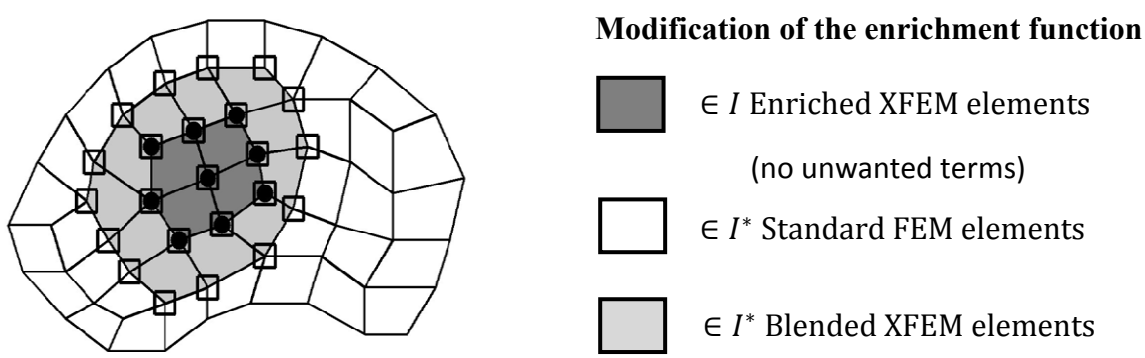

Figure 3.9: Two-dim representation of standard, enriched and blended elements.

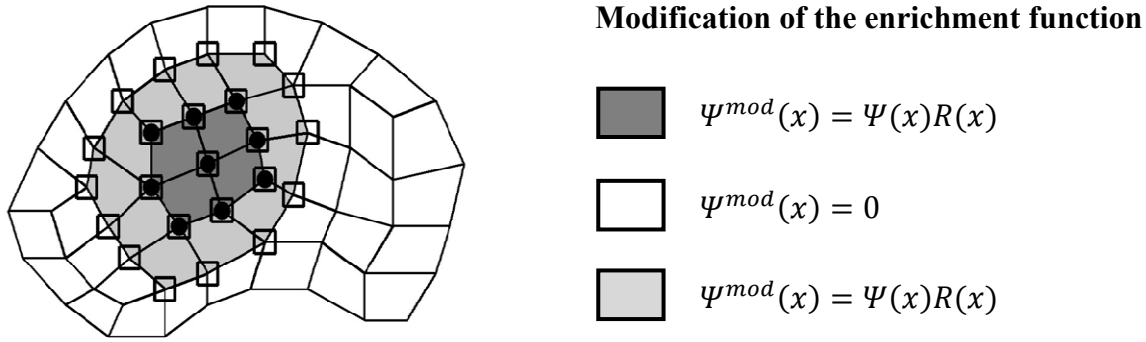

Figure 3.10: Standard, enriched and blended elements.

Typically, we expect the sum of all shape functions within an element be equal to one. This is true for standard FEM elements and enriched XFEM elements. However, for the blending elements this is not true for the standard XFEM. In order to fix this, we use the modification proposed by Moës et. al. [70]. We use a ramp function such that it is one within the enriched elements and zero within the blended ones, as shown in Figure 3.10. We call $R(x)$ the ramp function and define it as follows:

$$\boldsymbol{R}(\boldsymbol{x}) = \begin{cases} \mathbf{1}, & \in \boldsymbol{J}^* \\ \mathbf{0}, & \in \boldsymbol{I}^* \end{cases} \tag{3.60}$$

The modified enrichment function Ψ^{mod} is unchanged at the enriched elements, while it has zero value in standard finite elements. Implementing this modified enrichment function into Eq. (3.58), we get

$$u(x) = \sum_{I} N_i(x)u_i + \sum_{J^*} N_i^*(x)\Psi^{\mathrm{mod}}(x)a_i \tag{3.61}$$

Figure 3.11 shows the enriched shape functions, and we can observe that only the enriched elements are enriched by the enriched shape functions. Figure 3.12 shows the displacement profile with the modified XFEM. Compare to Figure 3.8, which contains unwanted terms that make the XFEM displacement profile not match the exact solution. Here, the displacement profile obtained using the modified XFEM matches exactly with the exact solution.

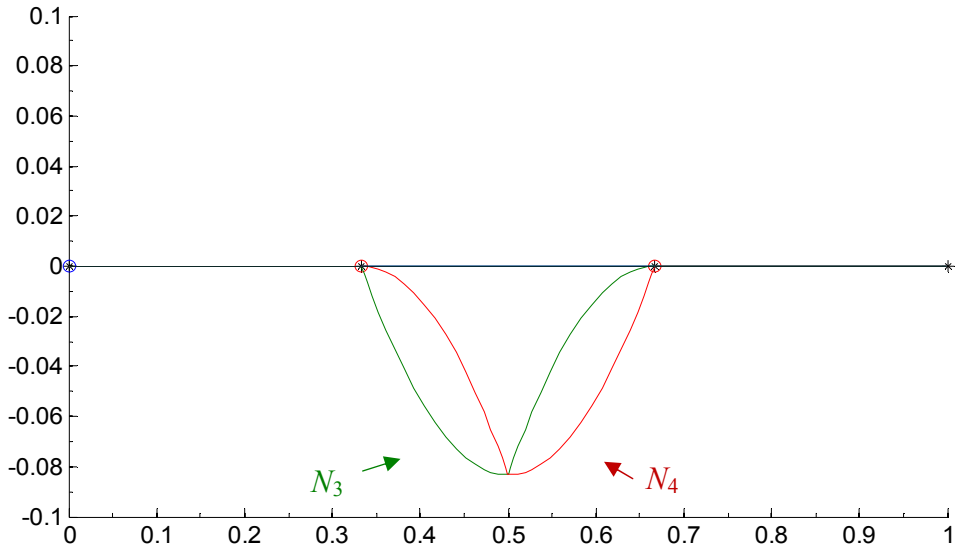

Figure 3.11: Enriched shape functions for a three-element solution using one-dimensional modified XFEM.

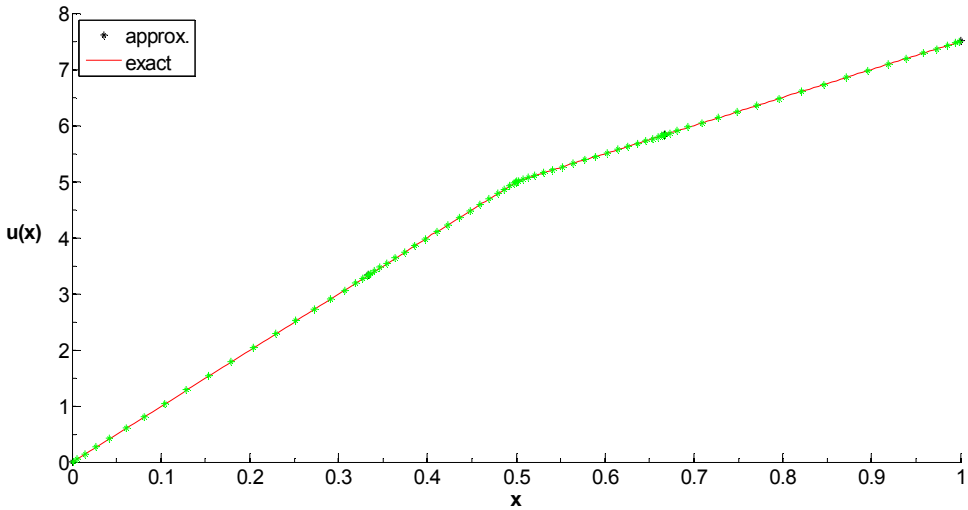

Figure 3.12: Three-element displacement profile for weak discontinuity of bimetalic bar using modified XFEM.

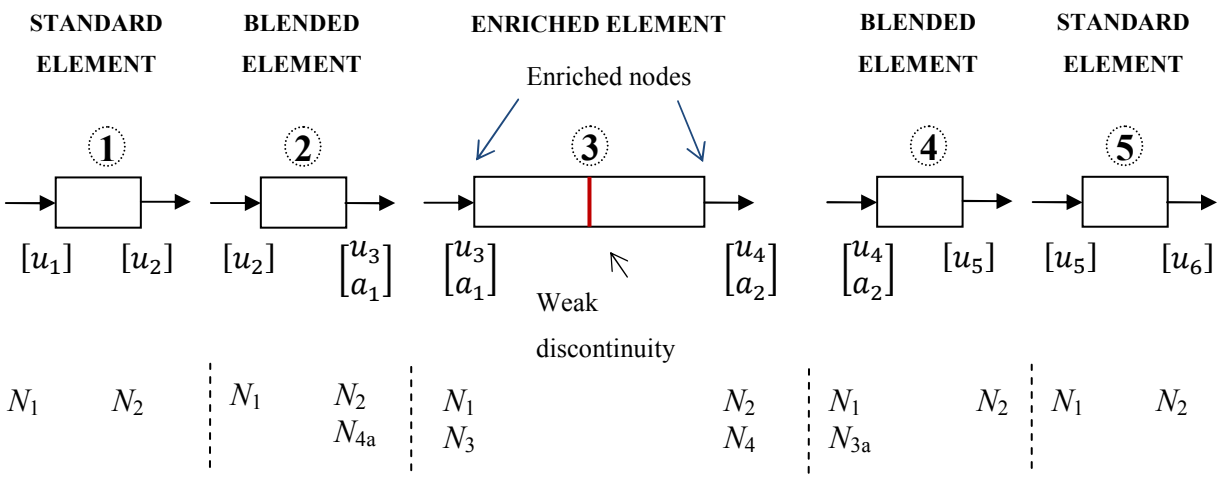

Figure 3.13: Five-element schematic for one-dim example.

3.1.4: FIVE-ELEMENT SOLUTION USING MODIFIED XFEM

Figure 3.13 shows three elements discretization of the bi-material elastic axial bar example. The geometric properties are $L_1 = L_2 = L_3 = L_4 = L_5 = 1/5$; and the mechanical properties are $E_1 = 1$ and $E_2 = 5$. The material interface is assumed $x_b = 0.5$ because it is the location of the discontinuity. The cross-sectional areas $A_1 = A_2 = A_3 = A_4 = A_5 = 1$. We express the axial displacement profile as follows:

$$u_1(x) = N_1 u_1 + N_2 u_2 \tag{3.62}$$

$$u_1(x) = N_1 u_1 + N_2 u_2 + N_{4a} a_1 \tag{3.63}$$

$$u_3(x) = N_1 u_3 + N_2 u_4 + N_3 a_1 + N_4 a_2 \tag{3.64}$$

$$u_4(x) = N_1 u_4 + N_2 u_5 + N_{3a} a_2 \tag{3.65}$$

$$u_5(x) = N_1 u_5 + N_2 u_6 \tag{3.66}$$

where u_1, u_2, u_3, u_4 are the nodal displacements; a_1, a_2 as the enriched nodal displacements; and the enriched shape functions are shown in Figure 3.14.

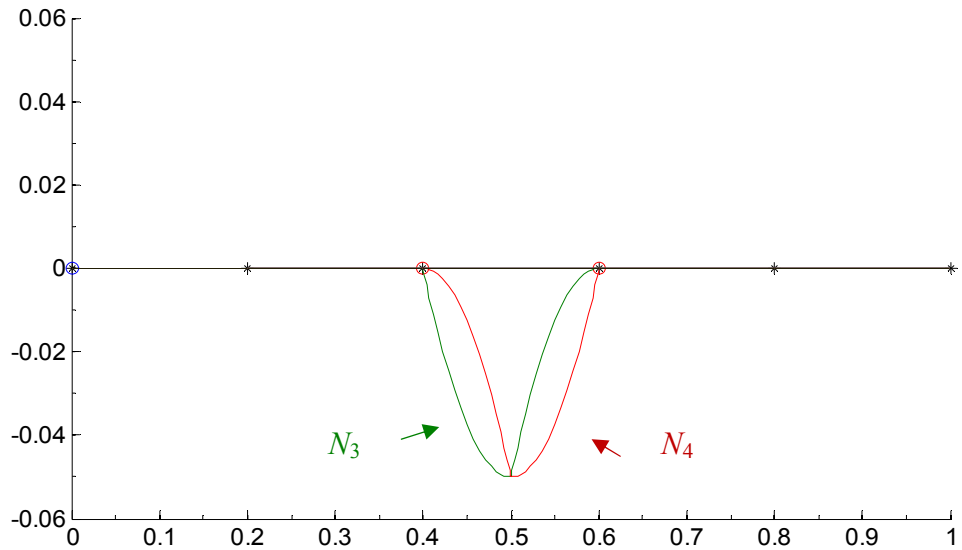

Figure 3.14: Enriched shape functions for a five-element solution using one-dimensional modified XFEM.

The only nonzero strains for an axial bar are

$$\varepsilon_{xx}^{(1)} = \begin{bmatrix} \frac{\partial N_1}{\partial x} & \frac{\partial N_2}{\partial x} \end{bmatrix} \begin{Bmatrix} u_1 \\ u_2 \end{Bmatrix} = \mathbf{B}^{(1)} \begin{Bmatrix} u_1 \\ u_2 \end{Bmatrix} \tag{3.67}$$

$$\varepsilon_{xx}^{(2)} = \begin{bmatrix} \frac{\partial N_1}{\partial x} & \frac{\partial N_2}{\partial x} & \vdots & \frac{\partial N_{4a}}{\partial x} \end{bmatrix} \begin{Bmatrix} u_1 \\ u_2 \\ a_1 \end{Bmatrix} \tag{3.68}$$

$$\varepsilon_{xx}^{(3)} = \begin{bmatrix} \frac{\partial N_1}{\partial x} & \frac{\partial N_2}{\partial x} & \vdots & \frac{\partial N_3}{\partial x} & \frac{\partial N_4}{\partial x} \end{bmatrix} \begin{Bmatrix} u_3 \\ u_4 \\ a_1 \\ a_2 \end{Bmatrix} = \begin{cases} \mathbf{B}_1^{(3)} \begin{Bmatrix} u_2 \\ u_3 \\ a_1 \\ a_2 \end{Bmatrix}, & x < x_b \\ \mathbf{B}_2^{(3)} \begin{Bmatrix} u_2 \\ u_3 \\ a_1 \\ a_2 \end{Bmatrix}, & x \geq x_b \end{cases} \tag{3.69}$$

$$\varepsilon_{xx}^{(4)} = \begin{bmatrix} \frac{\partial N_1}{\partial x} & \frac{\partial N_2}{\partial x} & \vdots & \frac{\partial N_{3a}}{\partial x} \end{bmatrix} \begin{Bmatrix} u_4 \\ u_5 \\ a_2 \end{Bmatrix} \tag{3.70}$$

$$\varepsilon_{xx}^{(5)} = \begin{bmatrix} \frac{\partial N_1}{\partial x} & \frac{\partial N_2}{\partial x} \end{bmatrix} \begin{Bmatrix} u_5 \\ u_6 \end{Bmatrix} \tag{3.71}$$

We calculate the stresses using the Hooke's Law for isotropic materials:

$$\mathbf{S}^{(1)} = \mathbf{D}^{(1)}\,\mathbf{E}^{(1)} = [\mathrm{E}_1]\,\mathbf{B}^{(1)}\,\mathbf{q}^{(1)} \tag{3.72}$$

$$\mathbf{S}^{(2)} = \mathbf{D}^{(2)}\,\mathbf{E}^{(2)} = [\mathrm{E}_1]\,\mathbf{B}^{(2)}\,\mathbf{q}^{(2)} \tag{3.73}$$

$$\mathbf{S}_1^{(3)} = \mathbf{D}_1^{(3)}\mathbf{E}_1^{(3)} = [\mathrm{E}_1]\,\mathbf{B}_1^{(3)}\,\mathbf{q}^{(3)}$$

$$\mathbf{S}_2^{(3)} = \mathbf{D}_2^{(3)}\mathbf{E}_2^{(3)} = [\mathrm{E}_2]\,\mathbf{B}_2^{(3)}\,\mathbf{q}^{(3)} \tag{3.74}$$

$$\mathbf{S}^{(4)} = \mathbf{D}^{(4)}\,\mathbf{E}^{(4)} = [\mathrm{E}_2]\,\mathbf{B}^{(4)}\,\mathbf{q}^{(4)} \tag{3.75}$$

$$\mathbf{S}^{(5)} = \mathbf{D}^{(5)}\,\mathbf{E}^{(5)} = [\mathrm{E}_2]\,\mathbf{B}^{(5)}\,\mathbf{q}^{(5)} \tag{3.76}$$

Using the principle of virtual work, we find the linear system of equations as follows:

$$\begin{bmatrix} 5 & -5 & 0 & 0 & 0 & 0 & 0 & 0 \\ -5 & 10 & -5 & 0 & 0 & 0 & 0 & 0 \\ 0 & -5 & 12.5 & -7.5 & 0 & 0 & -0.25 & -0.25 \\ 0 & 0 & -7.5 & 17.5 & -10 & 0 & 0.25 & 0.25 \\ 0 & 0 & 0 & -10 & 20 & -10 & 0 & 0 \\ 0 & 0 & 0 & 0 & -10 & 10 & 0 & 0 \\ 0 & 0 & -0.25 & 0.25 & 0 & 0 & 0.1667 & 0.05 \\ 0 & 0 & -0.25 & 0.25 & 0 & 0 & 0.05 & 0.2333 \end{bmatrix} \begin{Bmatrix} u_1 \\ u_2 \\ u_3 \\ u_4 \\ u_5 \\ u_6 \\ a_1 \\ a_2 \end{Bmatrix} = \begin{Bmatrix} F_1 \\ 0 \\ 0 \\ 0 \\ 0 \\ 1 \\ 0 \\ 0 \end{Bmatrix} \tag{3.77}$$

Figure 3.15 and Figure 3.16 show the displacement profiles. We can see that the modified XFEM produces the exact solution whereas the standard XFEM does not.

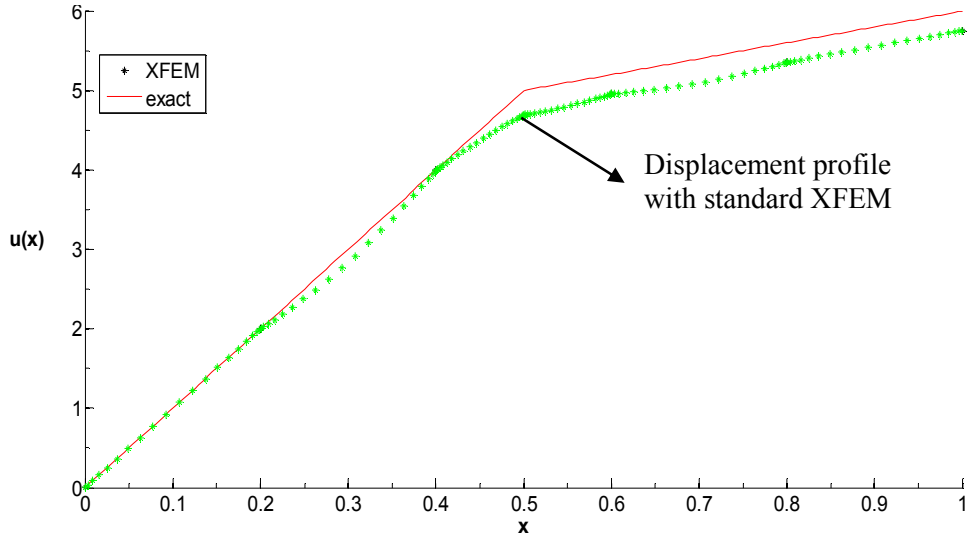

Figure 3.15: Five-element displacement profile for weak discontinuity of bimetalic bar using standard XFEM.

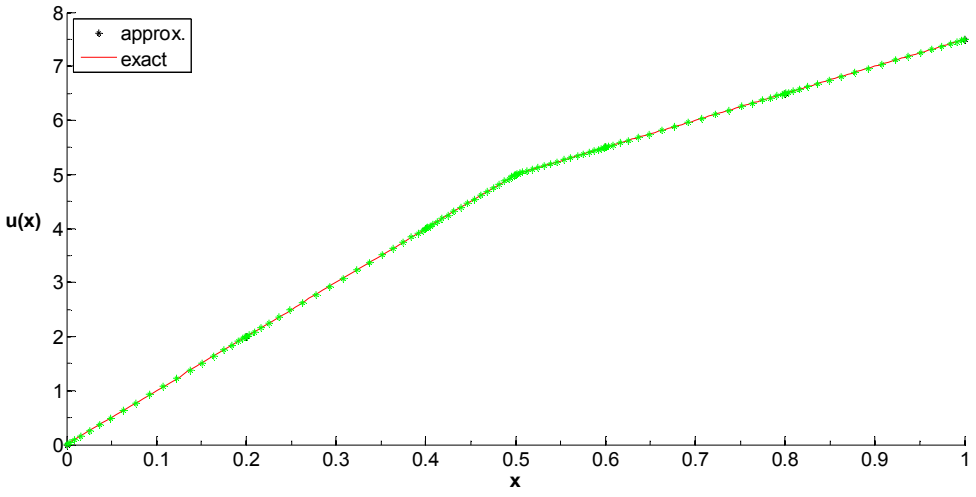

Figure 3.16: Five-element displacement profile for weak discontinuity of bimetalic bar using modified XFEM.

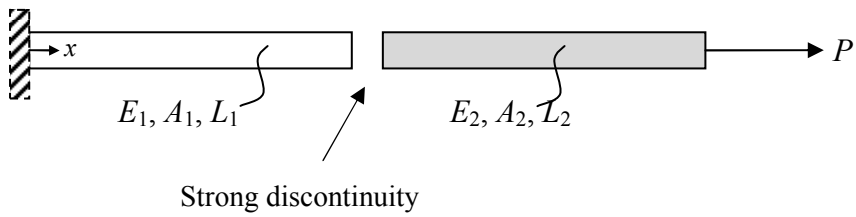

Figure 3.17: One-dimensional elastic bar example with a strong discontinuity.

3.2: EXAMPLE FOR STRONG DISCONTINUITY

Contrary to weak discontinuities which shows a continuous displacement profile in previous examples, strong discontinuities (such as in cracks) shows jumps in the displacement profile. Hence, in such cases we enrich the displacement field with a Heaviside, or a step, function. The resulting enriched function formed by multiplication of the enrichment function and the partition of unity shape function contains a jump at the interface and thus gives a better approximation to the field variable.

In order to understand these discontinuities, let us solve an elastic bar with a contained crack in the middle. Figure 3.17 shows an isotropic elastic axial bar fixed at $x = 0$ and subject to a point load P (=1) at $x = L$ (the tip). The geometric properties are $L_1 = L_2 = 0.5$; and the mechanical properties are $E_1 = E_2 = 1$. The material discontinuity is assumed $x_b = 0.5$. The cross-sectional areas $A_1 = A_2 = 1$. We are interested to determine the displacement profile using XFEM and then compared against the traditional FEM displacements values. Figure 3.18 shows the three-element discretization of the bi-material elastic axial bar example. The geometric properties are $L_1 = L_2 = L_3 = 1$.

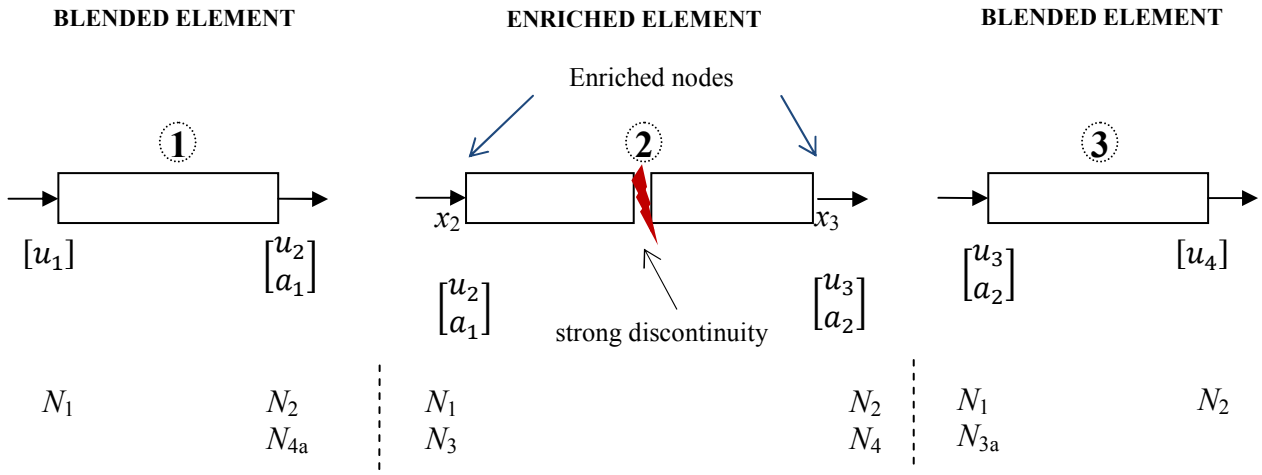

Figure 3.18: Three-element schematic for one-dimensional example with a strong discontinuity.

3.2.1: DISPLACEMENT PROFILE

In order to solve the problem using XFEM, we use the same non-aligned mesh discretization with three elements as shown in Figure 3.18. Since there is a strong discontinuity in the displacement field at the mid length of the bar, we used Heaviside function as an enrichment function. The standard degrees of freedom are denoted by u and enriched degrees of freedom are represented as a. There are four standard degrees of freedom, one at each node. The nodes x_2 and x_3 are cut by the crack; hence, we enriched these nodes with the Heaviside function. Therefore nodes x_2 and x_3 have two degree of freedoms each, one standard and one enriched. The structure now holds a total of six degrees of freedom, four standards and two enriched degree of freedoms. This is illustrated in Figure 3.18. We express the axial displacement profile as follows:

$$u_1(x) = N_1 u_1 + N_2 u_2 + N_4 a_1 \tag{3.78}$$

$$u_2(x) = N_1 u_2 + N_2 u_3 + N_3 a_1 + N_4 a_2 \tag{3.79}$$

$$u_3(x) = N_1 u_3 + N_2 u_4 + N_3 a_2 \tag{3.80}$$

where u_1, u_2, u_3, u_4 are the nodal displacements; a_1, a_2 as the enriched nodal displacements; and the shape functions are

$$N_1(x) = 1 - \frac{x}{L_e}, \quad N_2(x) = \frac{x}{L_e}$$

$$N_3(x) = N_1\Psi_1 \tag{3.81}$$

$$N_4(x) = N_2\Psi_2 \tag{3.82}$$

where Ψ is the Heaviside enrichment H function, shown in Figure 3.19.

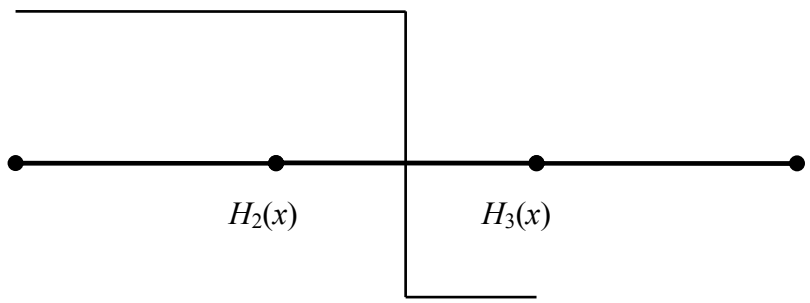

(a) Step function over the support of node x_2 shape function

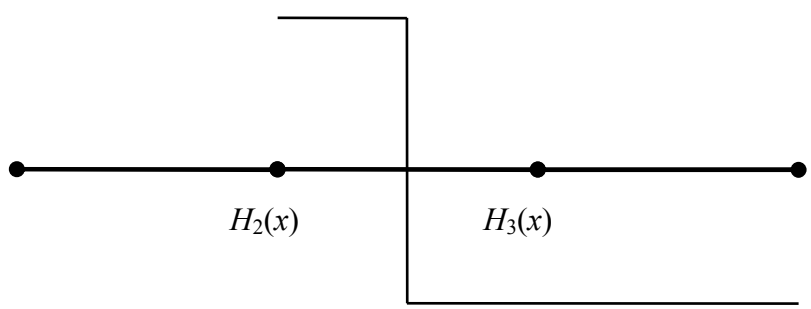

(b) Step function over the support of node x_3 shape function

Figure 3.19: 1 Heaviside Enrichment function for 1 dim bar.

3.2.2: STRAINS AND STRESSES

The only nonzero strains for an axial bar are

$$\varepsilon_{xx}^{(1)} = \begin{bmatrix} \frac{\partial N_1}{\partial x} & \frac{\partial N_2}{\partial x} & \vdots & \frac{\partial N_{4a}}{\partial x} \end{bmatrix} \begin{Bmatrix} u_1 \\ u_2 \\ a_1 \end{Bmatrix} = \mathbf{B}^{(1)} \begin{Bmatrix} u_1 \\ u_2 \\ a_1 \end{Bmatrix} \tag{3.83}$$

$$\varepsilon_{xx}^{(2)} = \begin{bmatrix} \frac{\partial N_1}{\partial x} & \frac{\partial N_2}{\partial x} & \vdots & \frac{\partial N_3}{\partial x} & \frac{\partial N_4}{\partial x} \end{bmatrix} \begin{Bmatrix} u_2 \\ u_3 \\ a_1 \\ a_2 \end{Bmatrix} = \begin{cases} \mathbf{B}_1^{(2)} \begin{Bmatrix} u_2 \\ u_3 \\ a_1 \\ a_2 \end{Bmatrix}, & x < x_b \\ \mathbf{B}_2^{(2)} \begin{Bmatrix} u_2 \\ u_3 \\ a_1 \\ a_2 \end{Bmatrix}, & x \geq x_b \end{cases} \tag{3.84}$$

$$\varepsilon_{xx}^{(3)} = \begin{bmatrix} \frac{\partial N_1}{\partial x} & \frac{\partial N_2}{\partial x} & \vdots & \frac{\partial N_{3a}}{\partial x} \end{bmatrix} \begin{Bmatrix} u_3 \\ u_4 \\ a_2 \end{Bmatrix} = \mathbf{B}^{(3)} \begin{Bmatrix} u_3 \\ u_4 \\ a_2 \end{Bmatrix} \tag{3.85}$$

We calculate the stresses using the Hooke's Law for isotropic materials:

$$\mathbf{S}^{(1)} = \mathbf{D}^{(1)}\, \mathbf{E}^{(1)} = [\mathrm{E}_1]\, \mathbf{B}^{(1)}\, \mathbf{q}^{(1)} \tag{3.86}$$

$$\mathbf{S}_1^{(2)} = \mathbf{D}_1^{(2)} \mathbf{E}_1^{(2)} = [\mathrm{E}_1]\, \mathbf{B}_1^{(2)}\, \mathbf{q}^{(2)}$$

$$\mathbf{S}_2^{(2)} = \mathbf{D}_2^{(2)} \mathbf{E}_2^{(2)} = [\mathrm{E}_2]\, \mathbf{B}_2^{(2)}\, \mathbf{q}^{(2)} \tag{3.87}$$

$$\mathbf{S}^{(3)} = \mathbf{D}^{(3)}\, \mathbf{E}^{(3)} = [\mathrm{E}_2]\, \mathbf{B}^{(3)}\, \mathbf{q}^{(3)} \tag{3.88}$$

3.2.3: DISCRETIZING THE EQUATIONS OF MOTION

After discretizing the principle of virtual work, we may express the elemental XFEM stiffness matrix as follows:

$$\mathbf{K}_{\mathrm{e}} = \begin{bmatrix} \mathbf{K}_{\mathrm{std,std}} & \mathbf{K}_{\mathrm{std,enr}} \\ \mathbf{K}_{\mathrm{enr,std}} & \mathbf{K}_{\mathrm{enr,enr}} \end{bmatrix} \tag{3.89}$$

In order to understand this, let us evaluate each one of the three elements:

1. **Element 1:** For element one, let us use the Heaviside function $H(x) = +1$, see Figure 3.19(a), in order to obtain our shape functions, and strain-displacement matrices:

$$\mathbf{N}_{\mathrm{std}} = \begin{bmatrix} 1 - \frac{x}{L} & \frac{x}{L} \end{bmatrix} \qquad \mathbf{N}_{\mathrm{enr}} = H\left[\frac{x}{L}\right] = \left[\frac{x}{L}\right] \tag{3.90}$$

$$\mathbf{B}_{\mathrm{std}}^{(1)} = \begin{bmatrix} \frac{-1}{L} & \frac{1}{L} \end{bmatrix} \qquad \mathbf{B}_{\mathrm{enr}}^{(1)} = H\left[\frac{1}{L}\right] = \left[\frac{1}{L}\right] \tag{3.91}$$

Hence,

$$\mathbf{K}_{\mathrm{std,std}} = \int_0^{L_{e1}} \left[\mathbf{B}_{std}^{(1)}\right]^{\mathbf{T}} [\mathrm{E}_1\mathrm{A}_1] \left[\mathbf{B}_{std}^{(1)}\right] \, \mathrm{d}x = \frac{\mathrm{E}_1\mathrm{A}_1}{\mathrm{L}} \begin{bmatrix} 1 & -1 \\ -1 & 1 \end{bmatrix} \tag{3.92}$$

$$\mathbf{K}_{\mathrm{std,enr}} = \mathbf{K}_{\mathrm{std,enr}}^{\mathrm{T}} = \int_0^{L_{e1}} \left[\mathbf{B}_{std}^{(1)}\right]^{\mathbf{T}} [\mathrm{E}_1\mathrm{A}_1] \left[\mathbf{B}_{enr}^{(1)}\right] \, \mathrm{d}x = \frac{\mathrm{E}_1\mathrm{A}_1}{\mathrm{L}} \begin{bmatrix} -1 \\ 1 \end{bmatrix} \tag{3.93}$$

$$\mathbf{K}_{\mathrm{enr,enr}} = \int_0^{L_{e1}} \left[\mathbf{B}_{enr}^{(1)}\right]^{\mathbf{T}} [\mathrm{E}_1\mathrm{A}_1] \left[\mathbf{B}_{enr}^{(1)}\right] \, \mathrm{d}x = \frac{\mathrm{E}_1\mathrm{A}_1}{\mathrm{L}} \tag{3.94}$$

$$\mathbf{K}^{(1)} = \begin{bmatrix} 1 & -1 & -1 \\ -1 & 1 & 1 \\ -1 & 1 & 1 \end{bmatrix} \tag{3.95}$$

2. **Element 2:** For element two, the Heaviside function $H(x)$ has two values (one before the crack and one after the crack) and is defined as follows:

$$H(x) = \begin{Bmatrix} +1 \text{ for } x < x_{\mathrm{b}} \\ -1 \text{ for } x > x_{\mathrm{b}} \end{Bmatrix} \tag{3.96}$$

The shape functions, and strain-displacement matrices are:

$$\mathbf{N}_{\mathrm{std}} = \begin{bmatrix} 1 - \frac{x}{L} & \frac{x}{L} \end{bmatrix} \qquad \mathbf{N}_{\mathrm{enr}} = H \begin{bmatrix} 1 - \frac{x}{L} & \frac{x}{L} \end{bmatrix} \tag{3.97}$$

$$\mathbf{B}_{\mathrm{std}}^{(2)} = \begin{bmatrix} \frac{-1}{L} & \frac{1}{L} \end{bmatrix} \qquad \mathbf{B}_{\mathrm{enr}}^{(2)} = H \begin{bmatrix} \frac{-1}{L} & \frac{1}{L} \end{bmatrix} \tag{3.98}$$

As it was in the case of weak discontinuities, we need to integrate the enriched terms on both sides (Ω_2^+ and Ω_2^-) of the discontinuity separately because this element contains a discontinuity. Hence,

$$\mathbf{K}_{\mathrm{std,std}}^{(2)} = \int_0^{L_{e2}} \left[\mathbf{B}_{\mathrm{std}}^{(2)}\right]^{\mathbf{T}} [\mathrm{E}_1\mathrm{A}_1] \left[\mathbf{B}_{\mathrm{std}}^{(2)}\right] \, \mathrm{d}x \tag{3.99}$$

$$\begin{aligned} \mathbf{K}_{\mathrm{std,enr}}^{(2)} = & \underbrace{\int_0^{x_b} \left[\mathbf{B}_{\mathrm{std}}^{(2)}\right]^{\mathbf{T}} [\mathrm{E}_1\mathrm{A}_1] \left[\mathbf{B}_{\mathrm{enr}}^{(2)}\right] \, \mathrm{d}x}_{H(x)=+1} \\ & + \underbrace{\int_{x_b}^{L_{e2}} \left[\mathbf{B}_{\mathrm{std}}^{(2)}\right]^{\mathbf{T}} [\mathrm{E}_2\mathrm{A}_2] \left[\mathbf{B}_{\mathrm{enr}}^{(2)}\right] \, \mathrm{d}x}_{H(x)=-1} \end{aligned} \tag{3.100}$$

$$\begin{aligned} \mathbf{K}_{\mathrm{enr,enr}}^{(2)} = & \underbrace{\int_0^{x_b} \left[\mathbf{B}_{\mathrm{enr}}^{(2)}\right]^{\mathbf{T}} [\mathrm{E}_1\mathrm{A}_1] \left[\mathbf{B}_{\mathrm{enr}}^{(2)}\right] \, \mathrm{d}x}_{H(x)=+1} \\ & + \underbrace{\int_{x_b}^{L_{e2}} \left[\mathbf{B}_{\mathrm{enr}}^{(2)}\right]^{\mathbf{T}} [\mathrm{E}_2\mathrm{A}_2] \left[\mathbf{B}_{\mathrm{enr}}^{(2)}\right] \, \mathrm{d}x}_{H(x)=-1} \end{aligned} \tag{3.101}$$

$$\mathbf{K}^{(2)} = \begin{bmatrix} 1 & -1 & 0 & 0 \\ -1 & 1 & 0 & 0 \\ 0 & 0 & 1 & -1 \\ 0 & 0 & -1 & 1 \end{bmatrix} \tag{3.102}$$

3. **Element 3:** For element three, we use the Heaviside function $H(x) = -1$, see Figure 3.19(b), in order to obtain our shape functions, and strain-displacement matrices:

$$\mathbf{N}_{\text{std}} = \left[1 - \frac{x}{L} \quad \frac{x}{L}\right] \qquad \mathbf{N}_{\text{enr}} = H\left[1 - \frac{x}{L}\right] = -\left[1 - \frac{x}{L}\right] \tag{3.103}$$

$$\mathbf{B}_{\text{std}}^{(3)} = \left[\frac{-1}{L} \quad \frac{1}{L}\right] \qquad \mathbf{B}_{\text{enr}}^{(3)} = H\left[\frac{-1}{L}\right] = \left[\frac{1}{L}\right] \tag{3.104}$$

Hence,

$$\mathbf{K}_{\text{std,std}} = \int_0^{L_{e3}} \left[\mathbf{B}_{std}^{(3)}\right]^{\mathbf{T}} [\mathrm{E}_2\mathrm{A}_2] \left[\mathbf{B}_{std}^{(3)}\right] \, \mathrm{d}x = \frac{\mathrm{E}_2\mathrm{A}_2}{\mathrm{L}} \begin{bmatrix} 1 & -1 \\ -1 & 1 \end{bmatrix} \tag{3.105}$$

$$\mathbf{K}_{\text{std,enr}} = \mathbf{K}_{\text{std,enr}}^{\mathrm{T}} = \int_0^{L_{e1}} \left[\mathbf{B}_{std}^{(2)}\right]^{\mathbf{T}} [\mathrm{E}_2\mathrm{A}_2] \left[\mathbf{B}_{enr}^{(2)}\right] \, \mathrm{d}x = \frac{\mathrm{E}_2\mathrm{A}_2}{\mathrm{L}} \left[\frac{-1}{1}\right] \tag{3.106}$$

$$\mathbf{K}_{\text{enr,enr}} = \int_0^{L_{e1}} \left[\mathbf{B}_{enr}^{(2)}\right]^{\mathbf{T}} [\mathrm{E}_2\mathrm{A}_2] \left[\mathbf{B}_{enr}^{(2)}\right] \, \mathrm{d}x = \frac{\mathrm{E}_2\mathrm{A}_2}{\mathrm{L}} \tag{3.107}$$

$$\mathbf{K}^{(3)} = \begin{bmatrix} 1 & -1 & -1 \\ -1 & 1 & 1 \\ -1 & 1 & 1 \end{bmatrix} \tag{3.108}$$

Hence, global stiffness matrix is

$$\mathbf{K} = \begin{bmatrix} 1 & -1 & 0 & 0 & -1 & 0 \\ -1 & 2 & -1 & 0 & 1 & 0 \\ 0 & -1 & 2 & -1 & 0 & -1 \\ 0 & 0 & -1 & 1 & 0 & 1 \\ -1 & 1 & 0 & 0 & 2 & -1 \\ 0 & 0 & -1 & 1 & -1 & 2 \end{bmatrix} \tag{3.109}$$

The displacement profile is plotted in Figure 3.20. The exact solution shows zero displacement from zero to 0.5 in, where the strong discontinuity is located in the bar. Due to the discontinuity in the plot at 0.5 one section has no displacement while the other section has a constant displacement after 0.5 in. Also, we can see the standard and enriched XFEM displacements profile. Finally, the summation of both displacements will match exactly the exact solution.

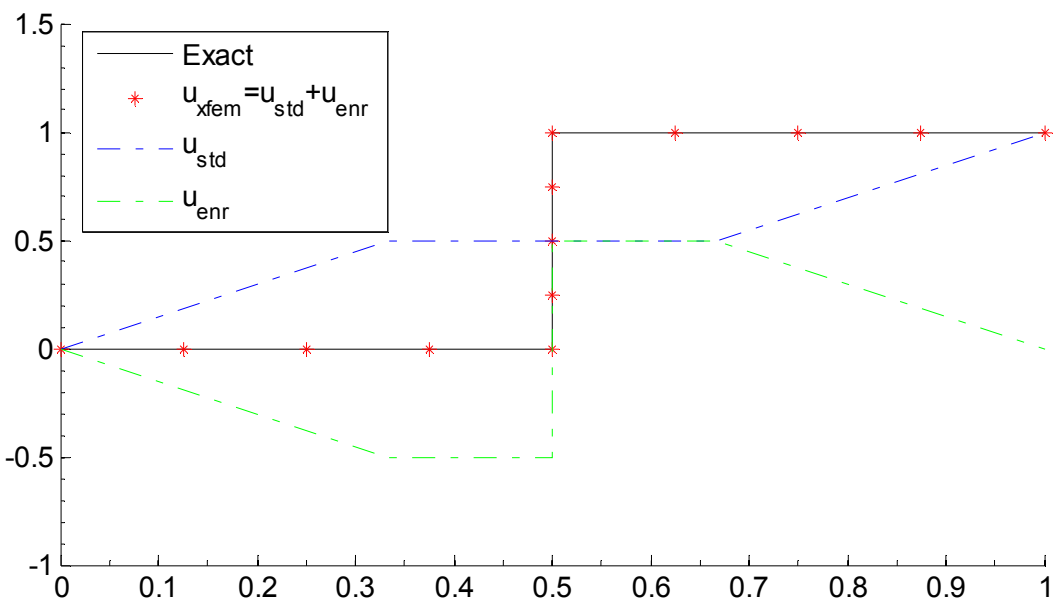

Figure 3.20: Numerical solution of displacement field using XFEM.

CHAPTER 4: 2D XFEM AS A MIXED-MODE FRACTURE AND FATIGUE TOOL

In Chapter 3, we explained the XFEM code for the one-dimensional case. Now that we have explained the basics of the XFEM using simple one-dimensional problems, let us proceed to explain the two-dimensional case using the one-dimensional as the base. Figure 3.1 provides a flowchart on how the code works. As input given by the user, this XFEM code consists in applying any size crack and location of any two-dimensional structure. Also, the user can modify the mesh size as well as the crack propagation steps.

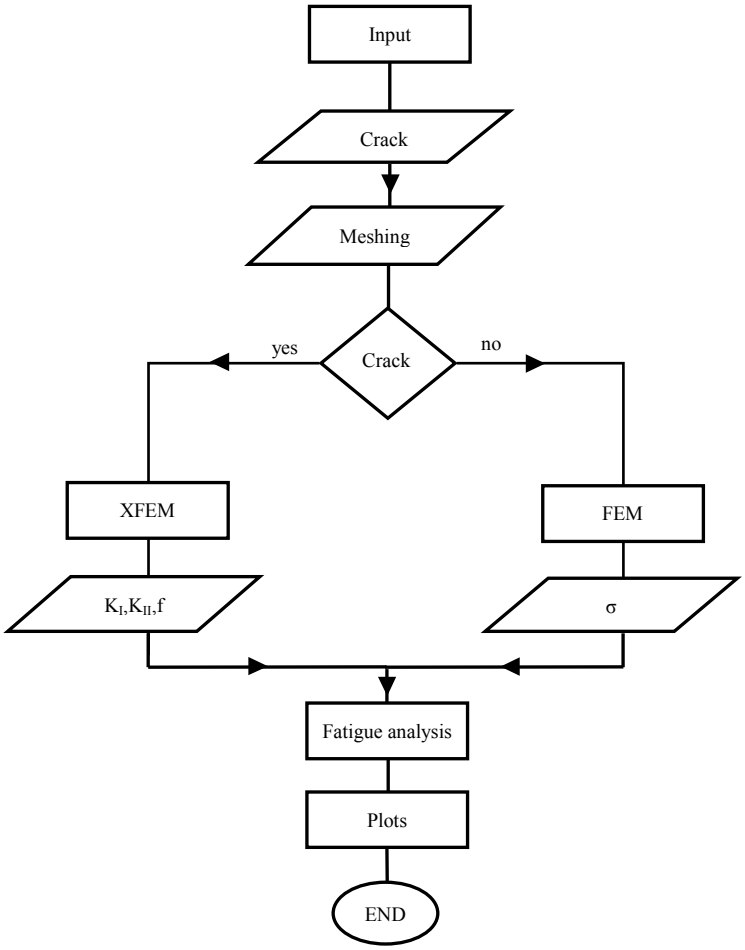

Figure 4.1: General flowchart of code.

4.1: FORMULATION

Figure 4.2 shows the two-dimensional schematic we plan to use to explain the 2D method. In the XFEM, we obtain the elemental matrices and vectors by evaluating each term at the nodes; i.e., the extended finite element procedure we use in this work is node-based. The enriched nodes are those nodes of the elements subject to discontinuities, such as cracks. There are two types of discontinuous elements: (i) *enriched XFEM elements*, which are elements through which the crack crosses the entire element (either by existence or propagation), (ii) and *enriched tip XFEM elements*, which are elements where the crack is subject to propagation. We need *blended XFEM elements* to ensure continuity of the degrees of freedom at each node. In the blended XFEM elements, we only enrich the nodes connected to the enriched elements. All other elements are treated as the standard finite elements. Through this work we plan to use bilinear quadrilateral elements, although we can expand the formulation to other two-dimensional elements. Figure 4.3 shows the some of the capabilities of XFEM. Figure 4.3(a) shows a two dimensional contour plot of an angled center crack with tension loading. Figure 4.3(b) shows the propagated center crack along the plate.

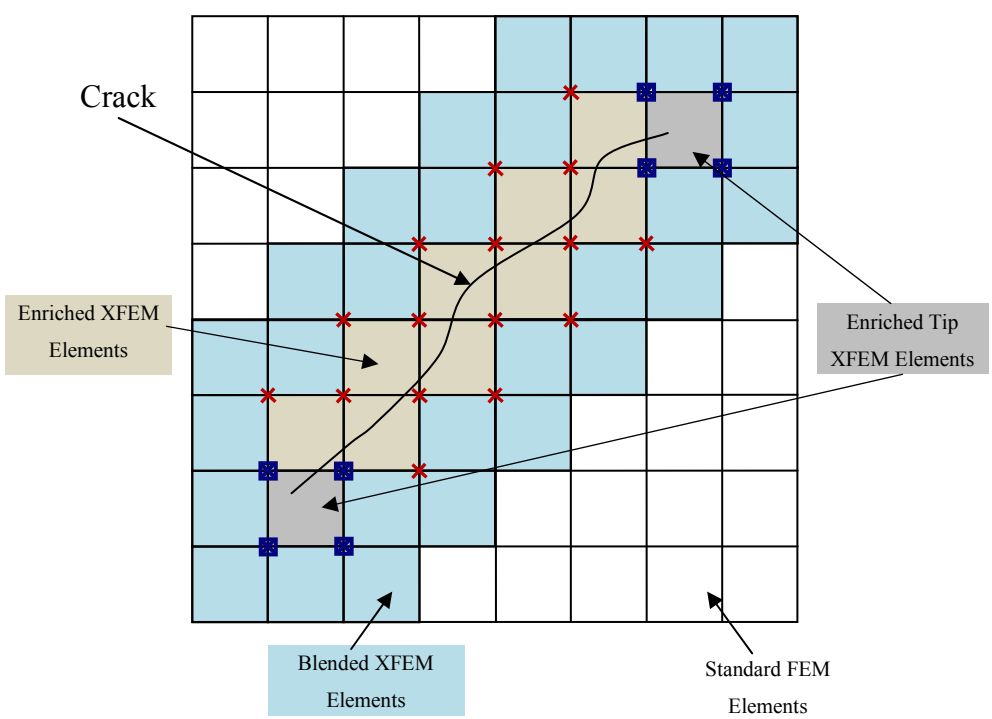

Figure 4.2: Two-dimensional schematic for the XFEM.

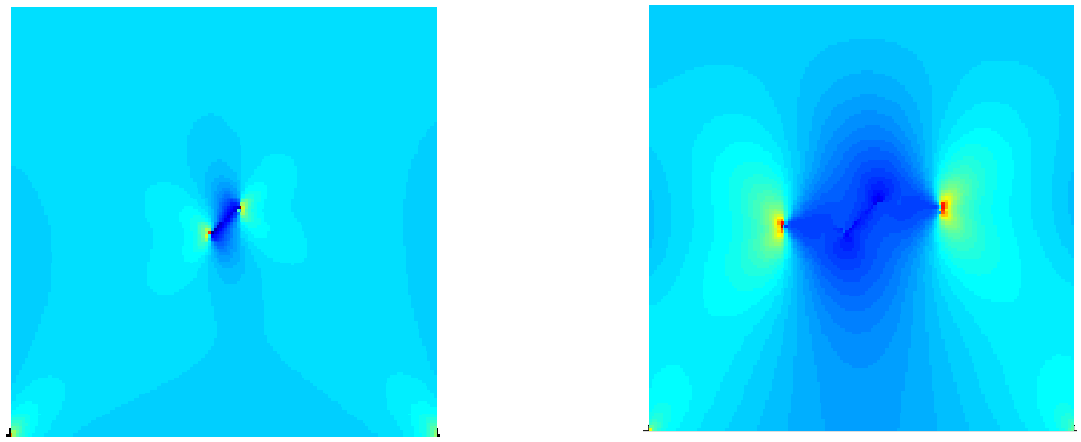

Figure 4.3: (a) XFEM contour stresses angled center crack. (b) Contour stresses of propagated angled center crack.

4.1.1: DISPLACEMENT PROFILE

The displacement profile for a two-dimensional elastic body is:

$$U(x,y,z) = u(x,y)$$

$$V(x,y,z) = v(x,y) \qquad \textbf{(4.1)}$$

$$W(x,y,z) = 0$$

XFEM provides a simple and efficient treatment of cracks where the element topologies do not conform to the crack geometry. In XFEM formulation, the displacement profile for the standard FEM elements (Figure 4.4 (a)) is obtained using the standard shape functions seen in Figure 4.4(b).

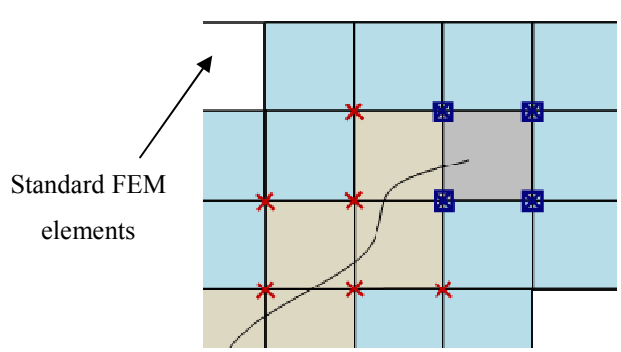

$$N_1 = \frac{1}{4}(1+r)(1+s)$$

$$N_2 = \frac{1}{4}(1-r)(1+s)$$

$$N_3 = \frac{1}{4}(1-r)(1-s)$$

$$N_4 = \frac{1}{4}(1+r)(1-s)$$

Figure 4.4: (a) Standard FEM elements. (b) Standard FEM shape functions.

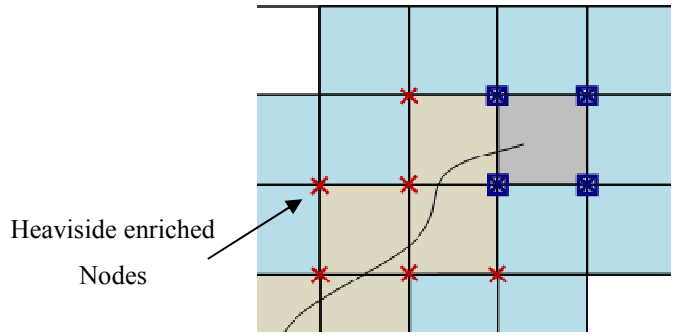

$$H(\underline{\mathbf{X}}) = \begin{cases} 1 & \text{for } (\underline{\mathbf{X}} - \underline{\mathbf{X}}^*).\underline{\mathbf{n}} \geq 0 \\ -1 & \text{for } (\underline{\mathbf{X}} - \underline{\mathbf{X}}^*).\underline{\mathbf{n}} < 0 \end{cases}$$

where $\underline{\mathbf{X}} = \{x,y\}$

Figure 4.5: (a) Heaviside enriched nodes. (b) Heaviside/step function for split enriched nodes.

In *enriched XFEM element*, elements are split by a discontinuity or a crack, and because of this, split nodes are enriched by using the enriched functions. This is shown in Figure 4.5(a). Enriched nodes are shown with an "*x*". We express the enriched functions as a function of the Heaviside/step function. The splitting of the domain by the crack causes a displacement jump and the Heaviside/step function gives the desired behavior to approximate the true field. This step function is defined in Figure 4.5(b). For more information, see Appendix A.5.1. In Figure 4.5(b), $\underline{\mathbf{X}}$ is the point under consideration, $\underline{\mathbf{X}}^*$ (lies on the crack) is the nearest point to the crack segment and $\underline{\mathbf{n}}$ is the unit outward normal to crack at $\underline{\mathbf{X}}^*$. A step function or Heaviside enrichment is good when the element is totally cut by the crack. Figure 4.6 shows a representative schematic of the Heaviside function [71].

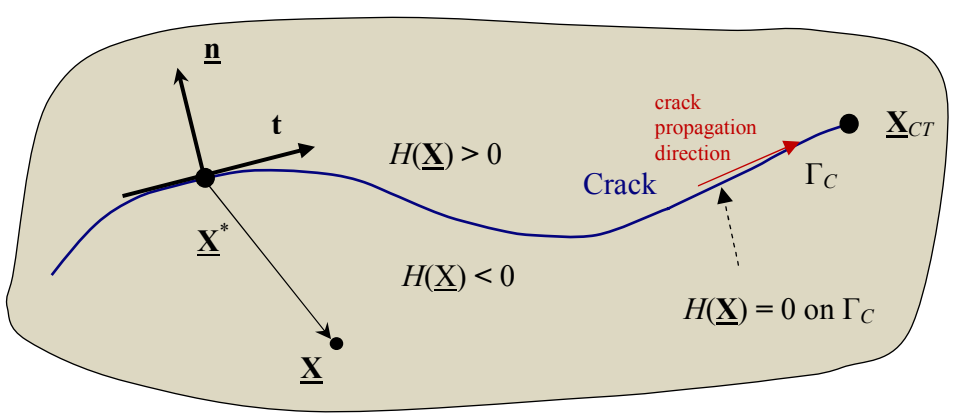

Figure 4.6: Illustration of the behavior of the Heaviside function.

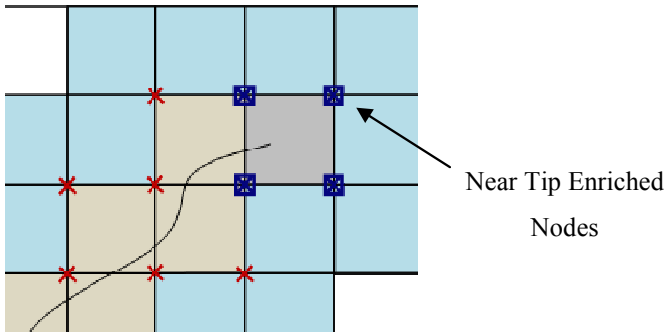

Figure 4.7: Near tip enriched nodes.

Hence, we define the enriched function as follows:

$$\psi = H(x,y) - H(x^*,y^*) \tag{4.2}$$

In case of the *enriched tip XFEM* elements, part of the element is cut and part of it not cut by the discontinuity or crack seen in Figure 4.7. Hence in such cases the step function cannot be used to enrich the domain. Near-tip enrichment functions, also known as branching functions, are used in order to evaluate the displacement field around the crack tip. These NT enriched functions are:

$$\mathbf{F}(r,\theta) = \left\{ \underbrace{\sqrt{r}\cos\left(\frac{\theta}{2}\right)}_{F_1} \quad \underbrace{\sqrt{r}\sin\left(\frac{\theta}{2}\right)}_{F_2} \quad \underbrace{\sqrt{r}\sin\left(\frac{\theta}{2}\right)\sin\theta}_{F_3} \quad \underbrace{\sqrt{r}\cos\left(\frac{\theta}{2}\right)\sin\theta}_{F_4} \right\} \tag{4.3}$$

where

$$r = \sqrt{x^2+y^2}, \text{ and } \theta = \tan^{-1}\left(\frac{y}{x}\right) \tag{4.4}$$

Hence, we define the near tip enriched functions as follows:

$$\varphi = \mathbf{F}(x,y) - \mathbf{F}(x^*,y^*) \tag{4.5}$$

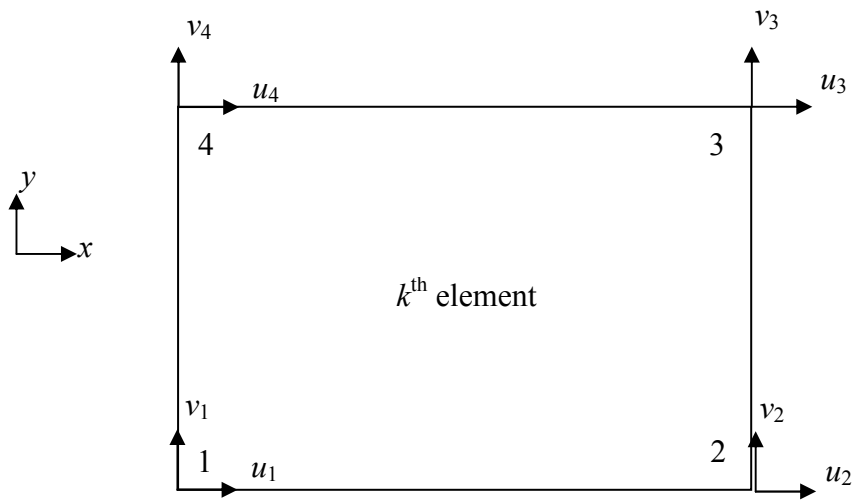

Figure 4.8: Node numbering for the kth element.

Equation (4.4) is defined in polar coordinates. This relationship ensures that the discontinuity does coincide with the geometry of the crack. These four functions are used for enriching the field near the crack tip, thus giving rise to four additional degrees of freedom in each direction at a node, in addition to standard degrees of freedom. Figure 4.8 shows the convention of the degrees of freedom. The discretized displacement field is given by the following expression:

$$u(x,y) = \underbrace{\sum_{i \in n_s} N_i\, u_i}_{\substack{\text{Standard FEA}\\ \text{nodes}}} + \underbrace{\sum_{i \in n_h} N_i\, \psi_i\, a_{x_i}}_{\substack{\text{Heaviside enriched}\\ \text{nodes}}} + \underbrace{\sum_{i \in n_f} \sum_{j=1}^{4} N_i\, \varphi_j\, b_{x_i}^{\,j}}_{\substack{\text{Near field tip}\\ \text{nodes}}} \tag{4.6}$$

$$v(x,y) = \underbrace{\sum_{i \in n_s} N_i\, v_i}_{\substack{\text{Standard FEA}\\ \text{nodes}}} + \underbrace{\sum_{i \in n_h} N_i\, \psi_i\, a_{y_i}}_{\substack{\text{Heaviside enriched}\\ \text{nodes}}} + \underbrace{\sum_{i \in n_f} \sum_{j=1}^{4} N_i\, \varphi_j\, b_{y_i}^{\,j}}_{\substack{\text{Near field tip}\\ \text{nodes}}} \tag{4.7}$$

where

- N_i are the standard finite element shape functions at node i
- φ_j are the Near Tip Enrichment functions at node i
- ψ_i are the Heaviside Enrichment functions at node i
- u_i, v_i are the classical degree of freedoms at the node i.
- a_i are the extra degree of freedoms for the discontinuity function.

- b_i^j are the extra degree of freedoms for the near tip enrichment function F_j
- n_s are the nodes per element
- n_h are the enriched nodes for the split elements
- n_f are the enriched nodes for enriched tip element

Since, $n_s = n_h = n_f = 4$

$$u(x,y) = \sum_{i=1}^{4} N_i \left(u_i + \psi_i \, a_{x_i} + \sum_{j=1}^{4} \varphi_j \, b_{x_i}^{\,j} \right) \tag{4.8}$$

$$v(x,y) = \sum_{i=1}^{4} N_i \left(v_i + \psi_i \, a_{y_i} + \sum_{j=1}^{4} \varphi_j \, b_{y_i}^{\,j} \right) \tag{4.9}$$

Hence, we express the displacement field for each element as follows:

$$\mathbf{d} = \underbrace{[\mathbf{N_{fem}} \vdots \mathbf{N_H} \vdots \mathbf{N_{NT}}]}_{\mathbf{N}} \underbrace{\begin{Bmatrix} \mathbf{q_{fem}} \\ \mathbf{q_H} \\ \mathbf{q_{NT}} \end{Bmatrix}}_{\mathbf{q}} \tag{4.10}$$

where **N** and **q** is the generalized shape function matrix and generalized degrees of freedom vector and are defined as follows:

$$\mathbf{N_{fem}} = \begin{bmatrix} N_1 & 0 & N_2 & 0 & N_{31} & 0 & N_4 & 0 \\ 0 & N_1 & 0 & N_2 & 0 & N_3 & 0 & N_4 \end{bmatrix}, \quad \mathbf{q_{fem}} = \begin{Bmatrix} u_1 \\ v_1 \\ u_2 \\ v_2 \\ u_3 \\ v_3 \\ u_4 \\ v_4 \end{Bmatrix} \tag{4.11}$$

$$\mathbf{N_H} = \begin{bmatrix} N_1\psi_1 & 0 & N_1\psi_1 & 0 & N_1\psi_1 & 0 & N_1\psi_1 & 0 \\ 0 & N_1\psi_1 & 0 & N_1\psi_1 & 0 & N_1\psi_1 & 0 & N_1\psi_1 \end{bmatrix}, \quad \mathbf{q_H} = \begin{Bmatrix} a_{x_1} \\ a_{y_1} \\ a_{x_2} \\ a_{y_2} \\ a_{x_3} \\ a_{x_3} \\ a_{x_4} \\ a_{x_4} \end{Bmatrix} \tag{4.12}$$

$$\mathbf{N_{NT}} = \begin{bmatrix} N_1\mathbf{\Phi} & 0 & N_1\mathbf{\Phi} & 0 & N_1\mathbf{\Phi} & 0 & N_1\mathbf{\Phi} & 0 \\ 0 & N_1\mathbf{\Phi} & 0 & N_1\mathbf{\Phi} & 0 & N_1\mathbf{\Phi} & 0 & N_1\mathbf{\Phi} \end{bmatrix}, \quad \mathbf{q_{NT}} = \begin{Bmatrix} \mathbf{b}_{x_1} \\ \mathbf{b}_{y_1} \\ \mathbf{b}_{x_2} \\ \mathbf{b}_{y_2} \\ \mathbf{b}_{x_3} \\ \mathbf{b}_{y_3} \\ \mathbf{b}_{x_4} \\ \mathbf{b}_{y_4} \end{Bmatrix} \tag{4.13}$$

In the above expression, for node one in the x-direction we get:

$$\sum_{j=1}^{4} \varphi_j \, b_{x_1}^{\,j} = \mathbf{\Phi}\, \mathbf{b}_{x_1}, \quad \mathbf{\Phi} = [\, \varphi_1 \quad \varphi_2 \quad \varphi_3 \quad \varphi_4], \quad \mathbf{b}_{x_1} = \begin{Bmatrix} b_{x_1}^1 \\ b_{x_1}^2 \\ b_{x_1}^3 \\ b_{x_1}^4 \end{Bmatrix} \tag{4.14}$$

There are eight degrees of freedom in the quadrilateral element when using the standard FEM approach. However, when the nodes are subject to Heaviside Enrichment functions, then there are eight additional degrees of freedom. The elements with a tip crack use Near Tip Enrichment functions which add thirty-two degrees of freedom. Note that when nodes are enriched by Near Tip Enrichment functions, the Heaviside Enrichment functions are not used.

4.1.2: STRAINS

The strains are not constant over the element and are calculated at the Gauss-Quadrature points. We define the strains as follow:

$$e_{xx} = \frac{\partial}{\partial x}[\mathbf{N_{fem}} \vdots \mathbf{N_H} \vdots \mathbf{N_{NT}}] \begin{Bmatrix} \mathbf{q_{fem}} \\ \mathbf{q_H} \\ \mathbf{q_{NT}} \end{Bmatrix} \tag{4.15}$$

$$e_{yy} = \frac{\partial}{\partial y}[\mathbf{N_{fem}} \vdots \mathbf{N_H} \vdots \mathbf{N_{NT}}] \begin{Bmatrix} \mathbf{q_{fem}} \\ \mathbf{q_H} \\ \mathbf{q_{NT}} \end{Bmatrix} \tag{4.16}$$

Hence,

$$\mathbf{E} = \begin{Bmatrix} e_{xx} \\ e_{yy} \end{Bmatrix} = \underbrace{[\mathbf{B_{fem}} \vdots \mathbf{B_H} \vdots \mathbf{B_{NT}}]}_{\mathbf{B}} \begin{Bmatrix} \mathbf{q_{fem}} \\ \mathbf{q_H} \\ \mathbf{q_{NT}} \end{Bmatrix} \tag{4.17}$$

4.1.3: STRESSES

The stresses are not constant over the element and are calculated at the Gauss-Quadrature points. We calculate the stresses using the Hooke's Law for isotropic materials:

$$\mathbf{S} = \mathbf{D}\,\mathbf{E} = \mathbf{D}\,\mathbf{B}\,\mathbf{q} = [\mathbf{D}]\,[\mathbf{B_{fem}} \vdots \mathbf{B_H} \vdots \mathbf{B_{NT}}] \begin{Bmatrix} \mathbf{q_{fem}} \\ \mathbf{q_H} \\ \mathbf{q_{NT}} \end{Bmatrix} \tag{4.18}$$

where ***D*** is the material constant matrix. For an isotropic two-dimensional element the matrix reduces to:

$$\mathbf{D} = \begin{bmatrix} D_{11} & D_{12} & 0 \\ D_{21} & D_{22} & 0 \\ 0 & 0 & D_{66} \end{bmatrix} \tag{4.19}$$

If we are using plane stress, $S_{zz} = 0$, the reduced material matrix ***D*** becomes:

$$\mathbf{D} = \frac{E}{1-\upsilon^2} \begin{bmatrix} 1 & \upsilon & 0 \\ \upsilon & 1 & 0 \\ 0 & 0 & \kappa\dfrac{1-\upsilon}{2} \end{bmatrix} \tag{4.20}$$

where κ is the shear correction factor and for our work we take $\kappa = 1$. If we are using plane strain, the reduced material matrix **D** becomes:

$$\mathbf{D} = \frac{E}{(1+\upsilon)(1-2\upsilon)} \begin{bmatrix} 1-\upsilon & \upsilon & 0 \\ \upsilon & 1-\upsilon & 0 \\ 0 & 0 & \kappa\dfrac{1-2\upsilon}{2} \end{bmatrix} \tag{4.21}$$

In this work, both *plane stress* and *plain strain* can be used on the XFEM code. Our results were using *plane stress* assumption is used because the thickness dimension is much smaller than the inplane dimensions. Also, inplane displacements, strains and stresses are uniform through the blades thickness and transverse stresses are negligible.

4.1.4: DISCRETIZING THE EQUATIONS OF MOTION

Using the principle of virtual work, our boundary value problem becomes

$$\int_{\Omega} \mathbf{S}^{\mathbf{T}}\, \boldsymbol{\delta}\mathbf{E}\, \mathrm{d}\Omega \;=\; \int_{\Omega} \mathbf{f_b}^{\mathbf{T}}\, \boldsymbol{\delta}\mathbf{d}\, \mathrm{d}\Omega \;+\; \int_{\Gamma} \mathbf{f_t}^{\mathbf{T}}\, \boldsymbol{\delta}\mathbf{d}\, \mathrm{d}\Gamma \tag{4.22}$$

where **S** is the stress vector, $\mathbf{f_b}$ and $\mathbf{f_t}$ are the body force and external traction vectors, respectively. Discretization of Eq. (4.22) using the XFEM procedure results in a discrete system of linear equilibrium equations:

$$\int_{\Omega} \mathbf{q}^{\mathbf{T}}\, \mathbf{B}^{\mathbf{T}}\mathbf{D}^{\mathbf{T}}\, \mathbf{B}\, \boldsymbol{\delta}\mathbf{q}\, \mathrm{d}\Omega \;=\; \int_{\Omega} \mathbf{f_b}^{\mathbf{T}}\, \mathbf{N}\, \boldsymbol{\delta}\mathbf{q}\, \mathrm{d}\Omega \;+\; \int_{\Gamma} \mathbf{f_t}^{\mathbf{T}}\, \mathbf{N}\, \boldsymbol{\delta}\mathbf{q}\, \mathrm{d}\Gamma \tag{4.23}$$

For all values of $\boldsymbol{\delta}\mathbf{q}$, we find our elemental stiffness matrix (per unit thickness):

$$\mathbf{K} = \int_{\Omega} \mathbf{B}^{\mathbf{T}}\mathbf{D}^{\mathbf{T}}\, \mathbf{B}\;\, \mathrm{d}\Omega \;=\; \int_{\Omega} \begin{Bmatrix} \mathbf{B_{fem}} \\ \mathbf{B_H} \\ \mathbf{B_{NT}} \end{Bmatrix} \mathbf{D}\, [\mathbf{B_{fem}} \,\vdots\, \mathbf{B_H} \,\vdots\, \mathbf{B_{NT}}]\;\, \mathrm{d}\Omega \tag{4.24}$$

or

$$\mathbf{K} = \begin{bmatrix} \mathbf{K_{fem,fem}} & \mathbf{K_{fem,H}} & \mathbf{K_{fem,NT}} \\ \mathbf{K_{H,fem}} & \mathbf{K_{H,H}} & \mathbf{K_{H,NT}} \\ \mathbf{K_{NT,fem}} & \mathbf{K_{NT,H}} & \mathbf{K_{NT,NT}} \end{bmatrix} \tag{4.25}$$

4.1.5: CENTRIFUGAL LOAD COMPUTATION

In this work, we assumed a constant angular velocity in order to create a body force. This body force per unit thickness was include into the MATLAB code, shown in Eq. (4.26). In Eq. (4.26), **N** is the shape function matrix, and $\bar{\mathbf{b}}$ is the centrifugal load per node being calculated defined in Eq.(4.27), where ρ is the material's density.

$$\mathbf{Q} = \int_{\Omega} \mathbf{f_b}^{\mathbf{T}}\, \mathbf{N}\, \boldsymbol{\delta}\mathbf{q}\, \mathrm{d}\Omega \;=\; \int_{\Omega} \mathbf{N}^{\mathbf{T}}\, \bar{\mathbf{b}}\, \mathbf{N}\, \boldsymbol{\delta}\mathbf{q}\, \mathrm{d}\Omega \tag{4.26}$$

$$\mathbf{b} = \begin{Bmatrix} \mathbf{b_{fem}} \\ \mathbf{b_H} \\ \mathbf{b_{NT}} \end{Bmatrix}, \quad \bar{\mathbf{b}}_{\mathbf{fem}} = \begin{Bmatrix} 0 \\ \rho\ \omega^2\ r \end{Bmatrix}, \quad r = [\mathbf{N_{fem}}] \begin{Bmatrix} r_1 \\ r_2 \\ r_3 \\ r_4 \end{Bmatrix}, \quad \bar{\mathbf{b}}_{\mathbf{H}} = \bar{\mathbf{b}}_{\mathbf{NT}} = \underline{\mathbf{0}} \tag{4.27}$$

Using XFEM formulation, r defined in Eq. (4.27) which only include standard FEM shape functions because body forces have to be implemented on physical nodes, therefore, enriched nodes contains zero body forces. Figure 4.9 shows the relationship between the quadratic node position and the distance from the rotating hub center. In this work, $r_1 = r_2$ and $r_3 = r_4$.

Also, as part of the original formulation of the code, XFEM computation was done node-wise, instead of using the more classical element-wise formulation. This means that instead of having different stiffness matrices for every element, our XFEM code calculates the stiffness elements for each node with its proper degree of freedom and assemblies the quantity directly into the global stiffness matrix. Same is true for the global load vector.

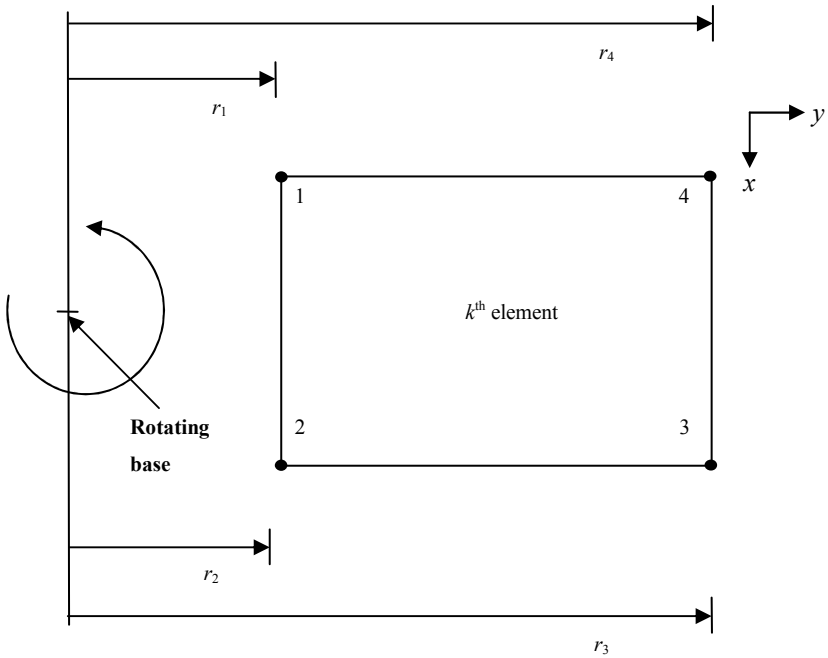

Figure 4.9: Centrifugal force node location schematic.

4.2: FATIGUE ANALYSIS

In order to determine the remaining life cycles of our system, we included a method to determine the fatigue analysis of rotating blades. We can summarize the steps as follows:

1. Determine von Mises stress.
2. Obtain "margin of safety" in order to justify failure by fracture, not by yielding.
3. Determine alternate and mean von Mises stresses.
4. Find exact node position where max alternate and mean stresses are located in blade.
5. Extract maximum mean stress and locate the alternate stress on same location.
6. Obtain fatigue analysis without any crack on blade.
7. Determine fatigue analysis for every crack propagation stage until blade failure.

In order to best describe the procedure of determining a fatigue analysis on our blade, we have to explain the previously mentioned steps. The first step was to determine the von Mises stresses. Equivalent stresses will take into account shear effects on our blade. Second step consists in the determination of the margin of safety. With the determination of margin of safety we justified failure by fracture, not by yielding. Mean and alternate stresses were determined taking into consideration that each of this two values had to be found the same node. Sounds trivial for a one-dimensional problem, but for these work some safety precaution had to be made in order to certify that this condition would be satisfied. After mean and alternate stresses have being determined, the next step is to calculate the remaining duty cycles of our blade for static fatigue analysis. In order to do this we used Goodman criterion. The last step was the determination of the remaining duty cycles for fatigue analysis. With this we identified crack propagation until failure. Figure 4.10 shows a flowchart that describes the steps taken for obtaining static fatigue analysis within our XFEM code. First, we applied one propagation step (*nstep = 1*), and computed static fatigue analysis using Goodman criterion. Remember that *nstep* is the total number of propagation steps on the system, and it is user defined. Also, *ipas* is the current propagation step. In order to determine the total fatigue life of our blade, we obtained the static fatigue for one propagation step and then summed it to the total changes in fatigue results.

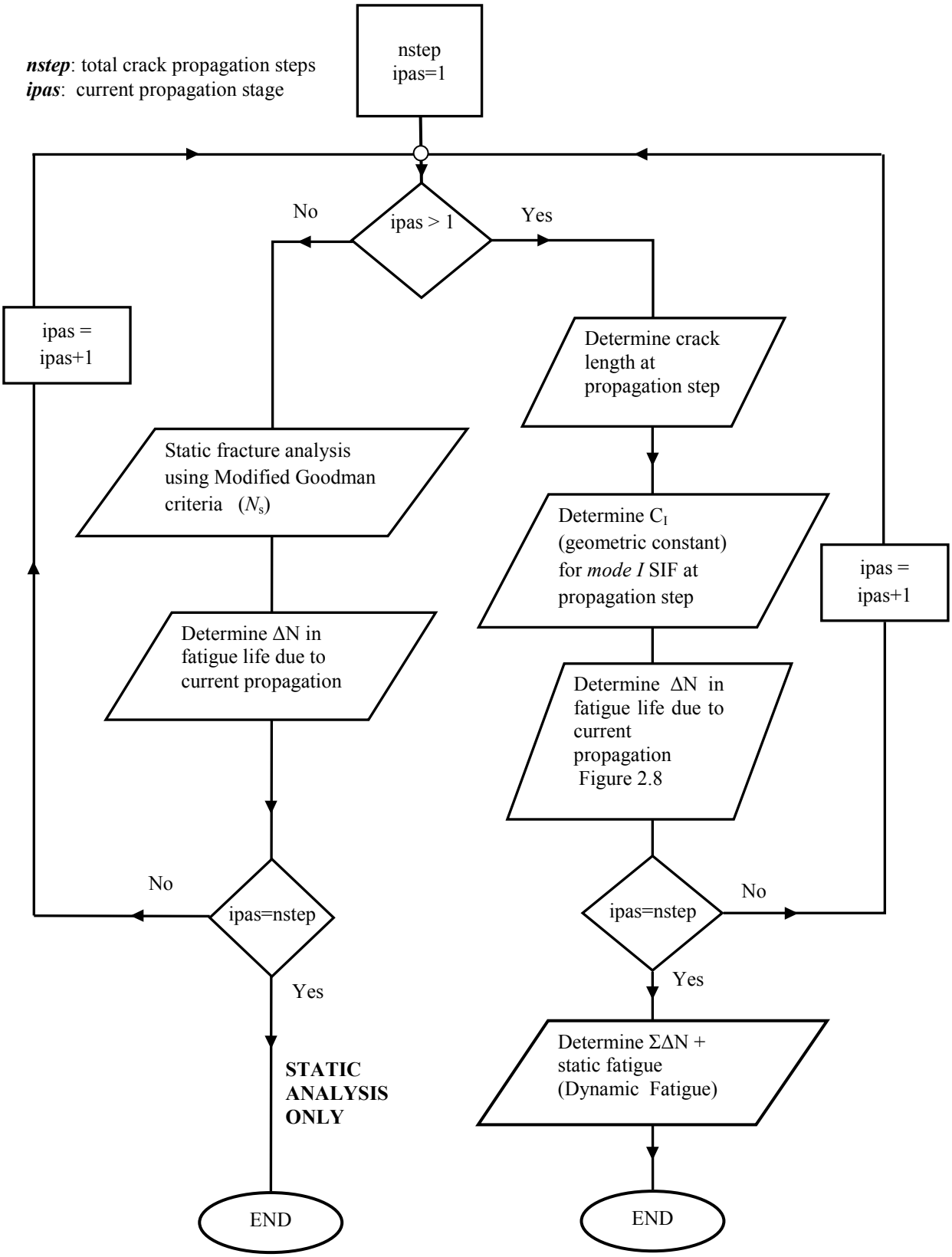

Figure 4.10: Flowchart of Fatigue Analysis procedure.

4.3: EXAMPLES

Here, we ran five different scenarios. The first three were used to validate our code and these are: (i) a fixed metal plate with no crack subject to a tensional stresses at the tip, (ii) a fixed metal plate with a single edged-crack subject to axial stresses due to centrifugal forces, (iii) a fixed metal plate with a single centered-crack at an angle subject to a tensional stresses at the tip. The last two cases are: (i) determination of the critical crack location, and (ii) fatigue analysis of the blade at the critical location.

4.3.1: CASE 1: FIXED PLATE WITH A TENSIONAL STRESS AND NO CRACK

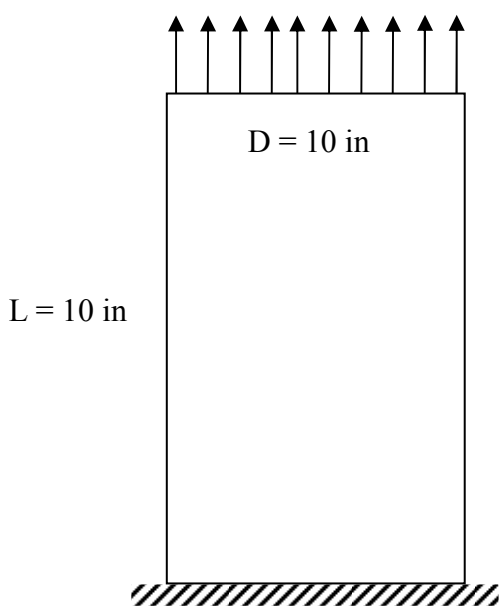

length (inches)	10
width (inches)	10
Modulus of Elasticity (psi)	2.9e7
Poisson's ratio	0.3

Figure 4.11: Fixed-plate with no crack and subject to a tensional stress load at the tip.

Figure 4.11 shows the problem we are running in XFEM. We ran this problem also in ANSYS Workbench. Figure 4.12 shows the von Mises stresses for this case. The results were identical to those from ANSYS. Maximum von-Misses stresses are located at the lower portion of the plate while zero stresses are reported at the top section of the plate. These lower nodes have a zero

translational degree of freedom (fixed end). The maximum von-Misses stresses value recorded was 32362 psi, which is identical to the value from ANSYS Workbench.

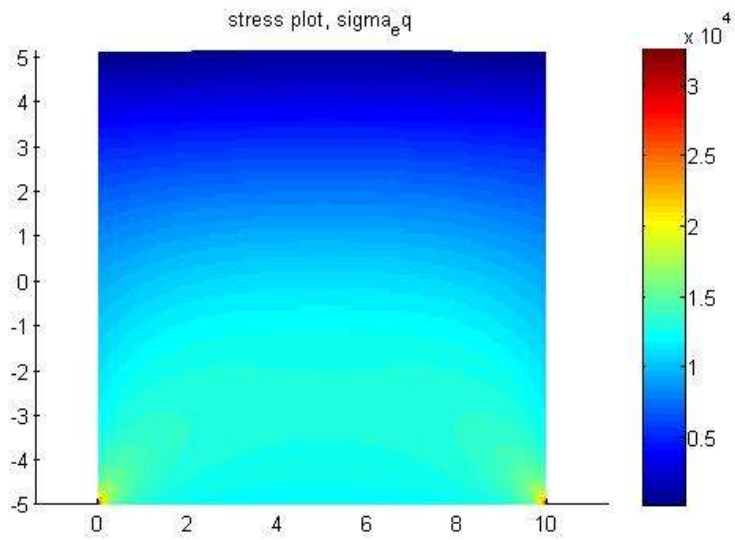

Figure 4.12: Results for case 1.

4.3.2: CASE 2: FIXED PLATE WITH CENTRIFUGAL FORCES AND A SINGLE EDGE-CRACK

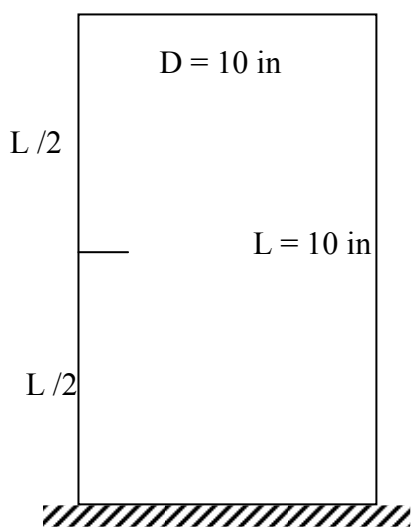

length (inches)	10
width (inches)	10
Modulus of Elasticity (psi)	2.9e7
Poisson's ratio	0.3
density (lb/in^3)	0.2836
rotational velocity (rpm)	300
transitional crack length (inches)	0.5709

Figure 4.13: Fixed-plate with a single edged-crack and subject to centrifugal forces.

Figure 4.13 shows a plate with an initial crack size of 0.5709 inches and this edge-crack is located 5 inches from the fixed end. For this case, no crack propagation was induced on the plate. The

main reason was to validate our XFEM code before moving forward. Figure 4.14 shows the contour plot of the von-Mises stress with a edged-crack. We can see from the figure where the initial crack was located. The maximum von Misses stress observed was of 45910 psi. In contrast with Figure 4.12, high stresses are located around the crack tip area while stresses at the lower portions of the blade decreases. Displacement values obtained from our XFEM code were also compared to those from ANSYS Workbench. Figure 4.15 illustrates a deformed mesh-grid of our plate. Deformation in the plate is minimal due to the combination of the blade's geometry and force being applied.

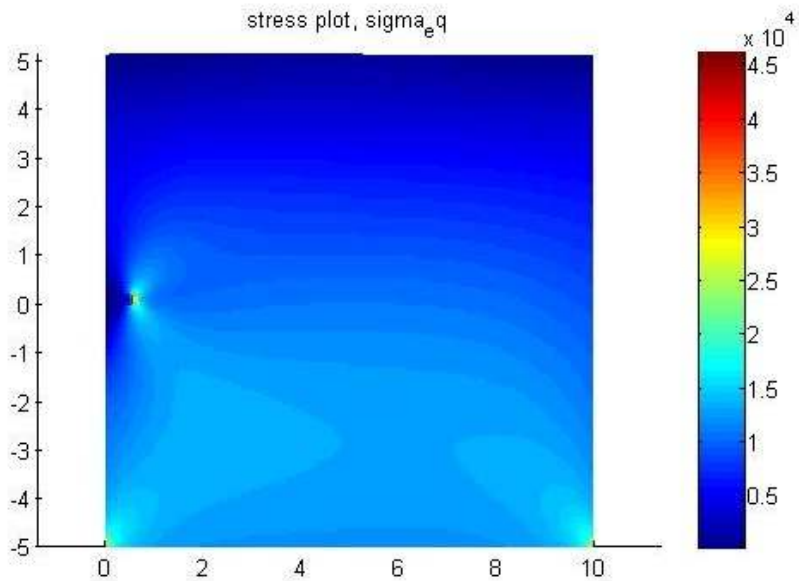

Figure 4.14: Contour plot for the von-Mises stresses for case 2.

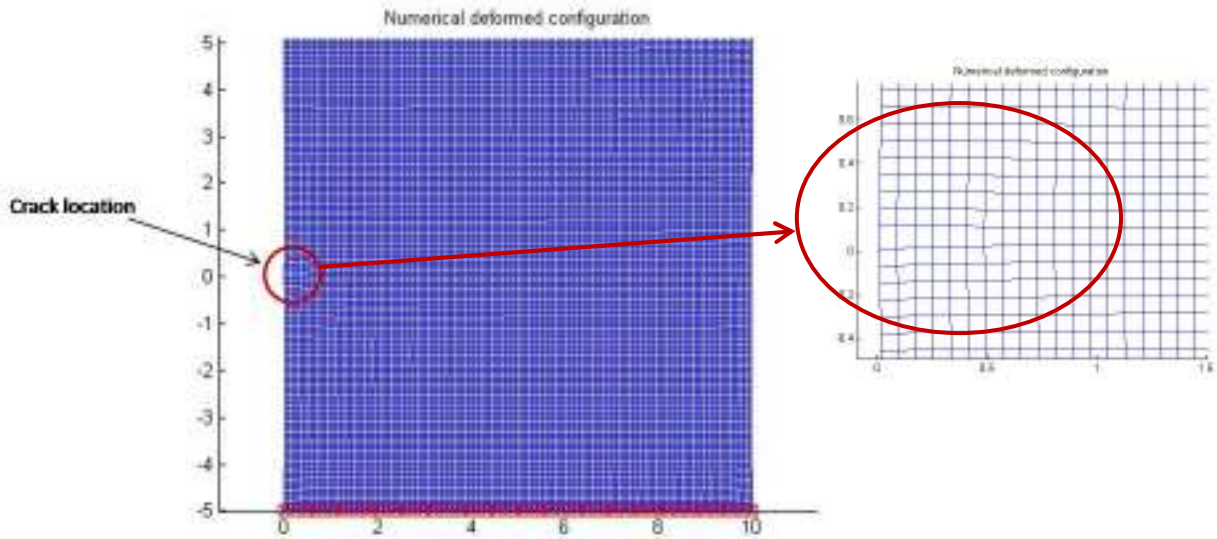

Figure 4.15: Deformation of meshed blade.

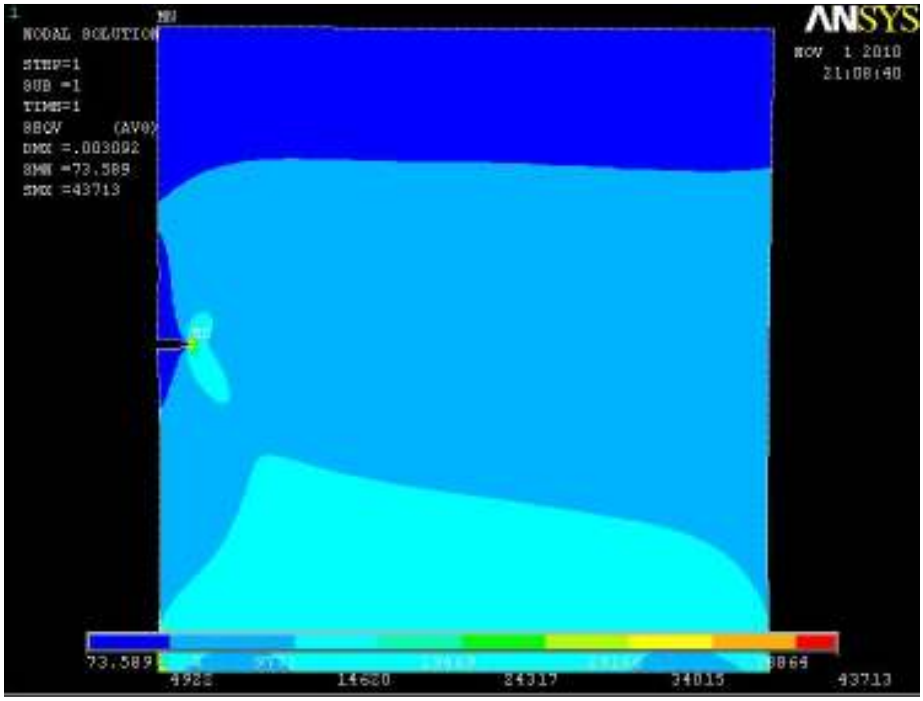

Figure 4.16: Computer simulation von-Misses stress.

Figure 4.16 illustrates von-Misses stress contour plot obtained using ANSYS Workbench. As expected, the maximum value is located around the crack tip area. We can see how the crack is been pulled, reflecting an axial force due to the rotational velocity of 300 rpm. This maximum value of von-Misses stress is 43713 psi. For a better appreciation of the crack tip area, the Figure 4.17 zooms in on Figure 4.16. From this figure we can see how the crack has been deformed, leaving a stress concentration location at the crack tip area. Figure 4.18 illustrates total deformation contour plot of our test blade. We can see that on the lower section of our blade there is zero deformation due to the fixed translational degree of freedom. The maximum deformation is located at the top section of the blade, and has a value of 0.003092 inches. Table 4.1 illustrates the stress and deformation values of both XFEM and simulation results.

The results are within 5% difference. The main difference could rely on the fact that the mesh size was not the same for both cases. If mesh size on both systems are not equal, nodes on crack tip area may not coincide with respect to the global coordinate system, therefore, w expect differences in stress and deformation values.

Table 4.1: XFEM and ANSYS results for case 2.

Quantity	**XFEM**	**ANSYS**
von-Misses stress (psi)	45910	43713
Total deformation (inches)	0.0033	0.0031

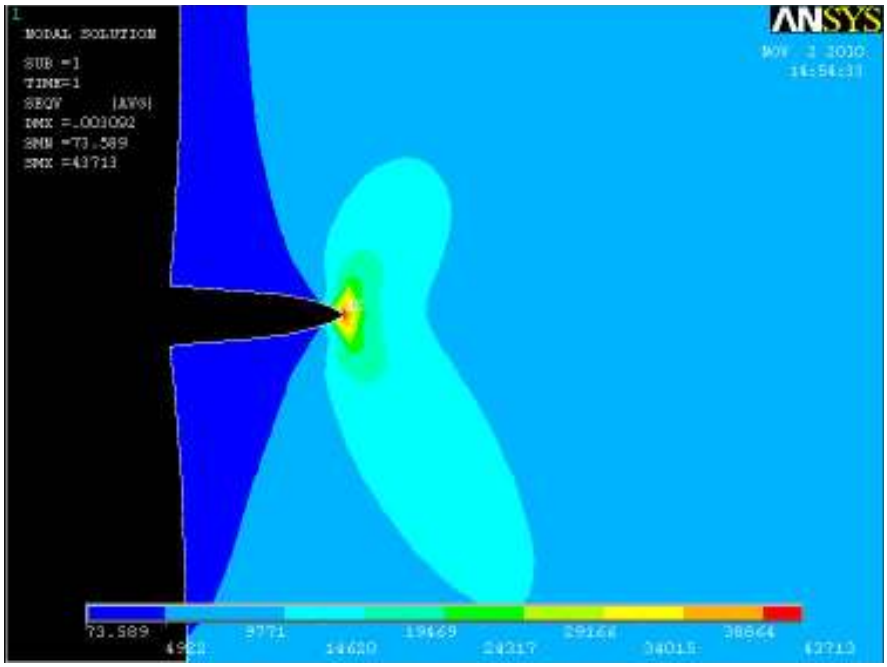

Figure 4.17: Zoom of computer simulation von-Misses stress.

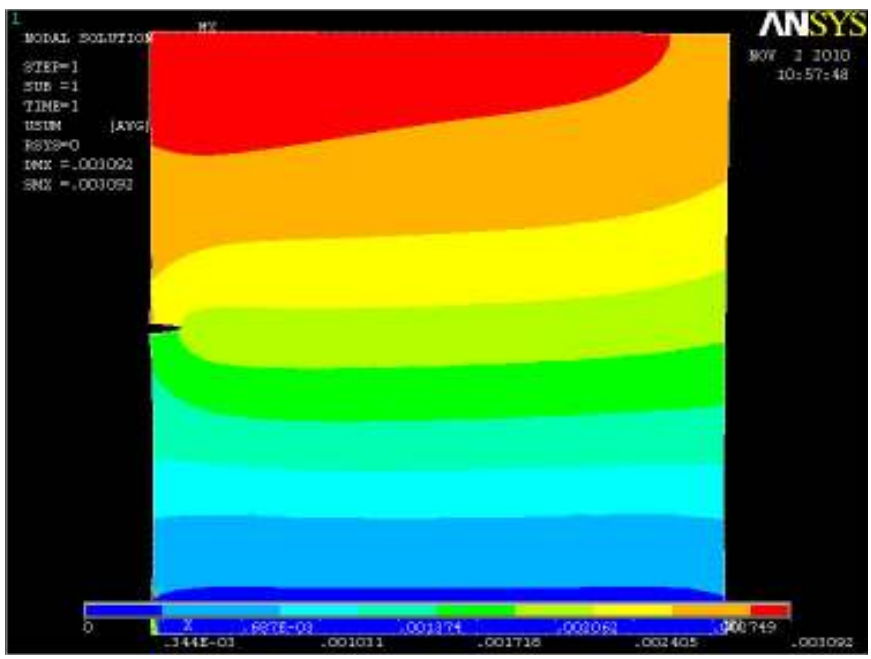

Figure 4.18: Total deformation.

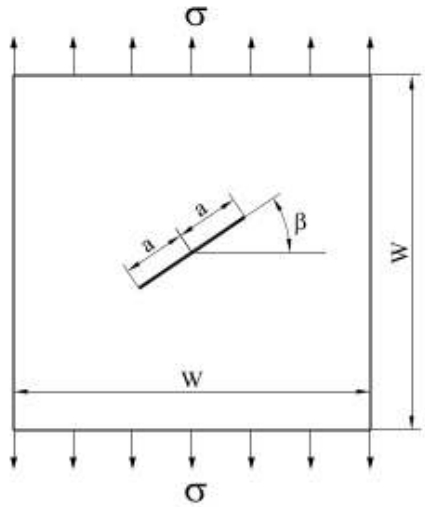

Figure 4.19: Inclined center crack in tension.

4.3.3: CASE 3: ANGLED CENTER CRACK

In order to validate our numerical SIF obtained on our XFEM code, we reproduced results obtained from a work done by Bordas [14]. Bordas created a two-dimensional plate with an angled center crack, as shown in Figure 4.19. Bordas showed that his numerical crack propagation profile were consistent with experimental data [72]. This is the main reason to use his work as means of comparison. The plate dimensions are taken to be w = 10 inches with a half crack length of a = 0.5 inches. As the plate dimensions are large in comparison to the crack length, the numerical solution can be compared to the solution for an infinite plate. For the given load shown, the exact stress intensity factors are given by:

$$K_I = \sigma\sqrt{\pi a}\cos^2\beta \qquad K_{II} = \sigma\sqrt{\pi a}\sin\beta\cos\beta \tag{4.28}$$

Figure 4.20, the normalized SIFs is compared to the exact solution. Excellent agreement between the numerical solution and the exact solution is obtained for the entire range of β. We can see how the maximum normalized exact and numeric K_{II} values are located at 45º. Also, maximum and minimum K_I and K_{II} values respectively are located when β is 0º.

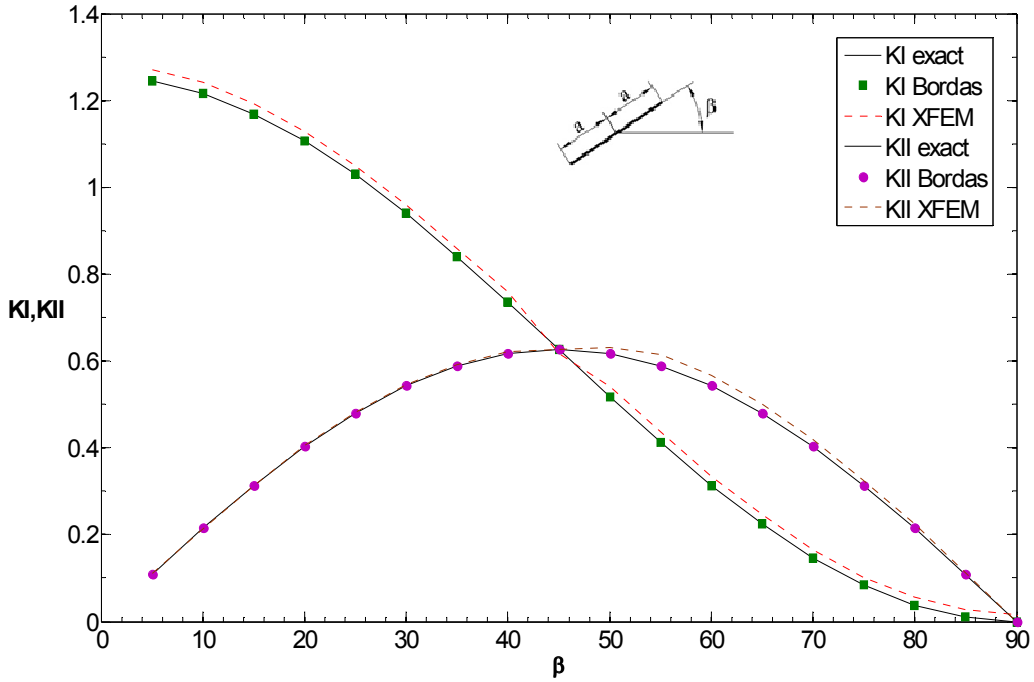

Figure 4.20: K_I and K_{II} vs. β for a plate with an angle center crack.

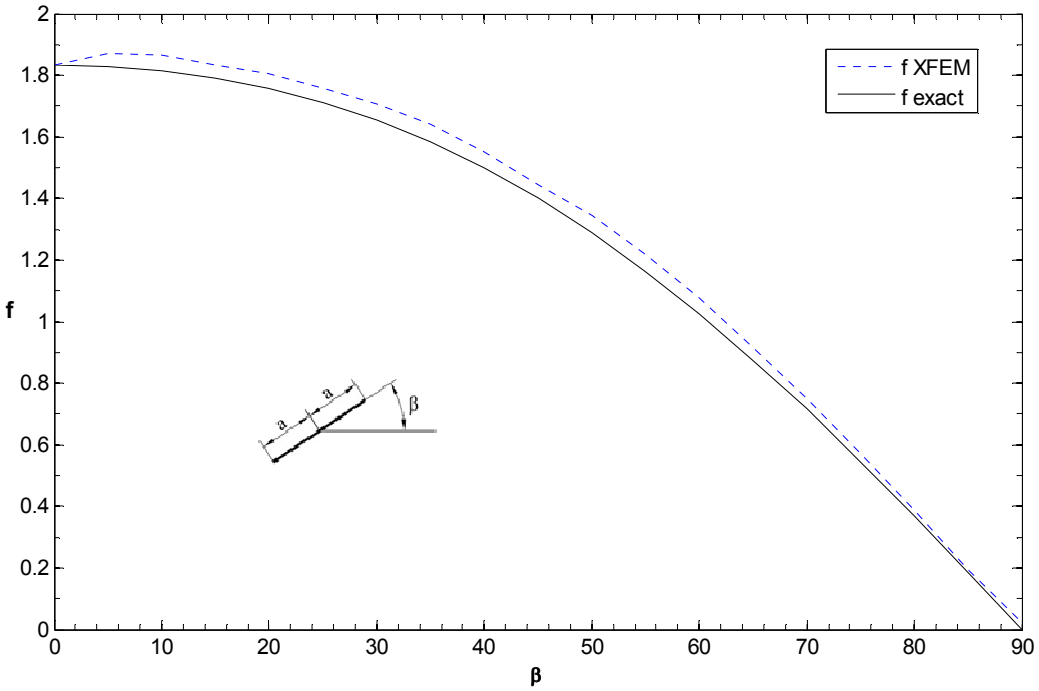

Figure 4.21: Mixed-mode dimensional stress intensity factor with respect to the angle β.

Figure 4.21 shows mixed-mode fatigue analysis on our angled center-crack with varying β using our XFEM code and analytical solution. The results show that the most critical angle is about zero degrees.

4.3.4: CASE 4: CRITICAL CRACK LOCATION IN ROTATING BLADE

Mixed mode static fatigue analysis is plotted with respect to the crack location along the blade. Also, in order to validate the most critical failure location in our blade obtained from our XFEM code we compared it against ANSYS. Because there are 321 crack intervals along the edge of the blade, a smooth stress curve can be appreciated and a critical stress location can be seen easily. For ANSYS, we applied a crack at twenty equally spaced locations throughout the blade and determine von Misses stresses. Figure 4.22 demonstrates is an estimate of where this critical location is located throughout the entire blade.

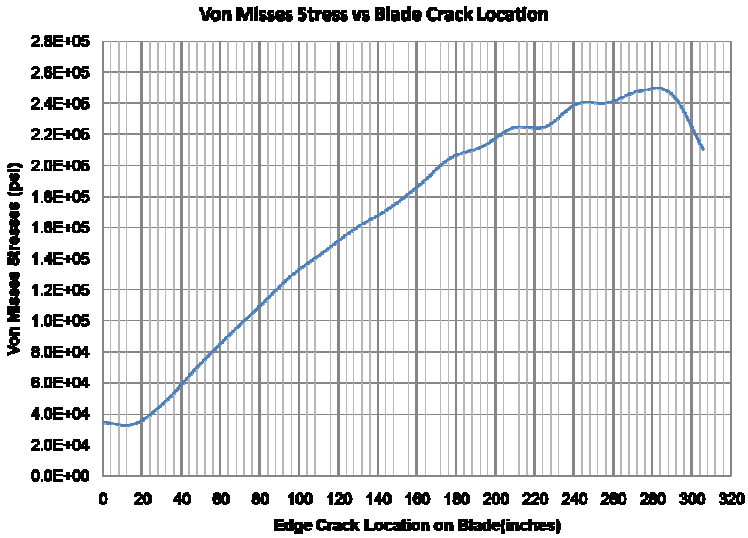

Figure 4.22: Von Misses stress vs. edge-crack location in Blade (inches).

On this smooth continuous curve, we can we can see that von Misses stresses are at its greater value at the location of the critical crack zone. The maximum Von Misses stress was around 280 inches. Although twenty equally spaced cracks along the blade gives you a rough estimate of the critical crack location when a centrifugal load is being applied, we can see this critical location being between 280 and 290 inches. As you can see from Figure 4.23, the blade's coordinate system is located at the edge of the blade. If the critical crack location ranges from 280 to 290 inches from the edge, the crack is located from 31.96 to 41.96 inches from the center hub (that would be about 11% from the center hub).

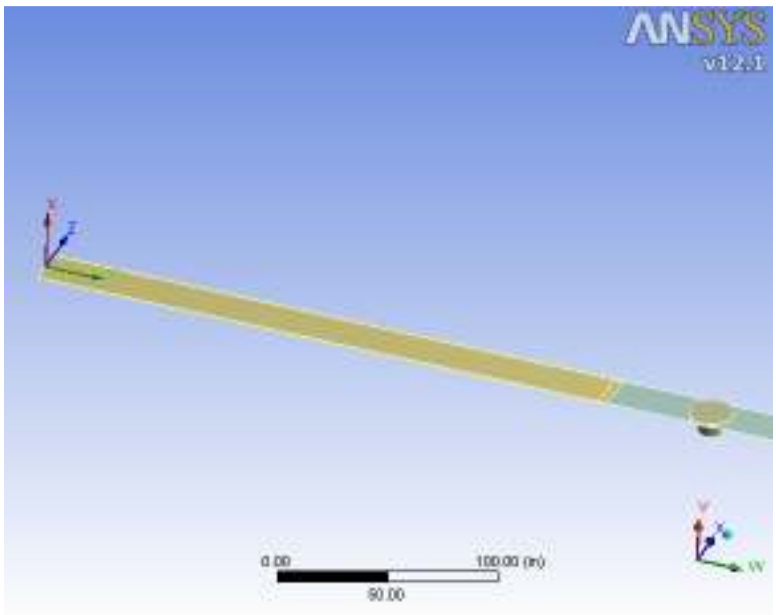

Figure 4.23: Blade coordinate system in ANSYS.

In order to find our critical crack location on our XFEM code, we determined mixed mode static fatigue analysis along the entire blade. Equation (2.5) shows the mixed-mode factor *f* that we used for our analytical expression. Important to highlight is that normalized values of the factor *f* as well as the blade length are used to create Figure 4.24. This plot illustrates mixed-mode *f* along the entire full length of the blade. As we can see, the curve has a maximum value at 0.8 (equivalent to 25.75 inches from the hub).

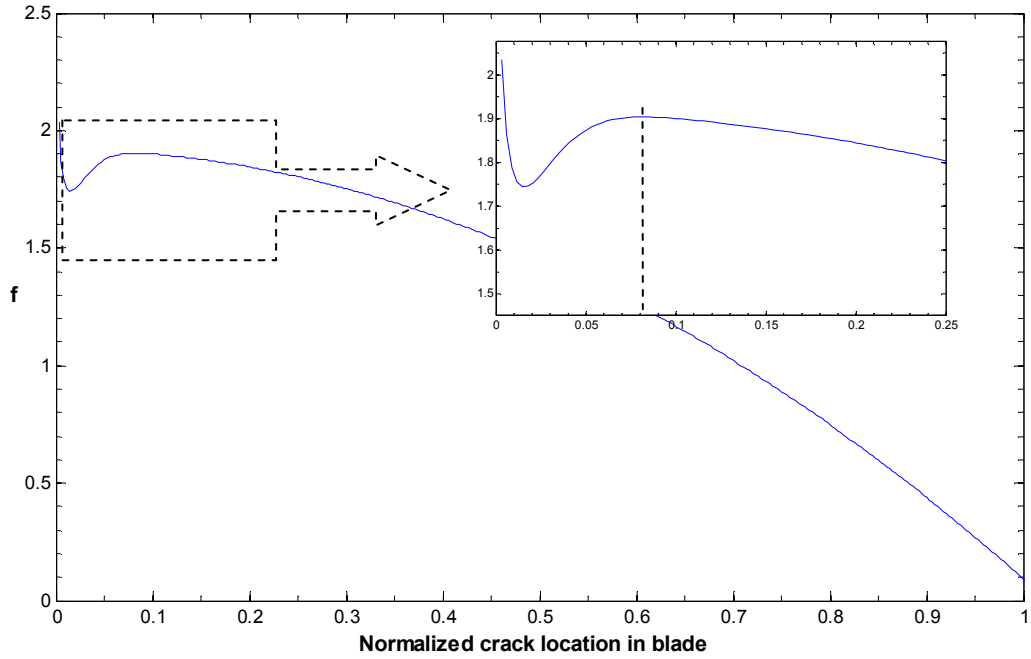

Figure 4.24: Mixed-mode static fatigue analysis.

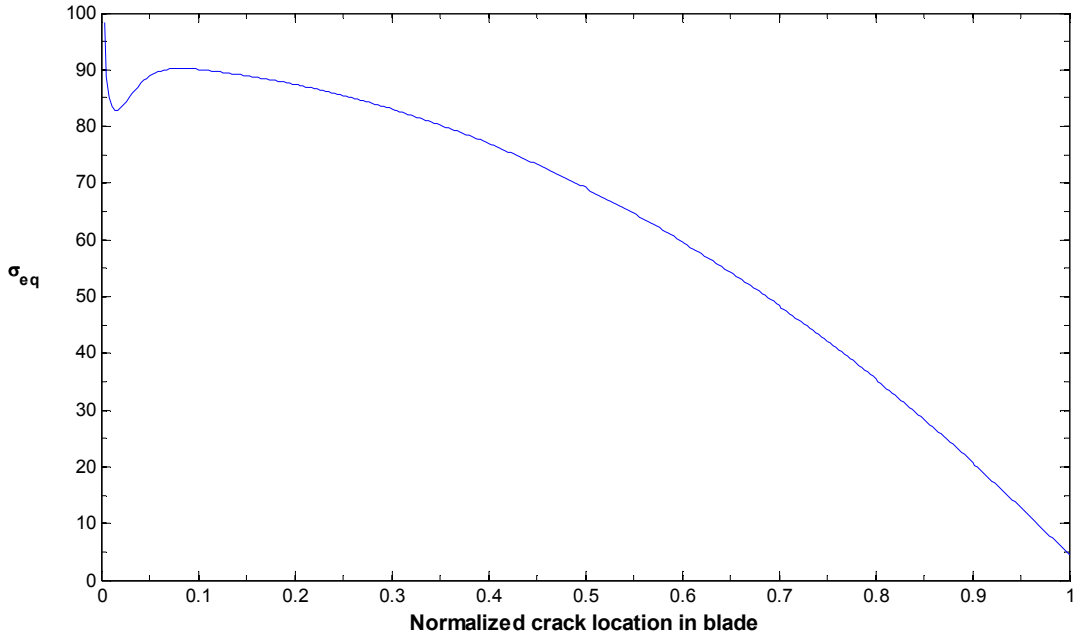

Figure 4.25: Von-Misses stress for edge-crack along entire length of blade.

A similar procedure was taken to generate Figure 4.25. This plot illustrates the von Misses stresses obtained from an edge-crack positioned along the entire blade's edge. As observed in Figure 4.24, the maximum equivalent stress is located at 0.08. This makes sense because the greater the equivalent stresses are, the less remaining duty cycles are available for failure to occur.

Figure 4.26 shows the shear stresses over crack location in blade. As we can see, even if we did not include any torsion loads on the blade (we assumed constant velocity), shear stress values appear close to the blade's center hub. This can be explained due to the shrinkage effect caused by the actual centrifugal load. As the blade rotates, it wants to stretch on the radial direction, but because the blade is fixed at the center hub, this prevents any shrinkage on the blade; therefore, shear stresses form in the fixed end of the blade.

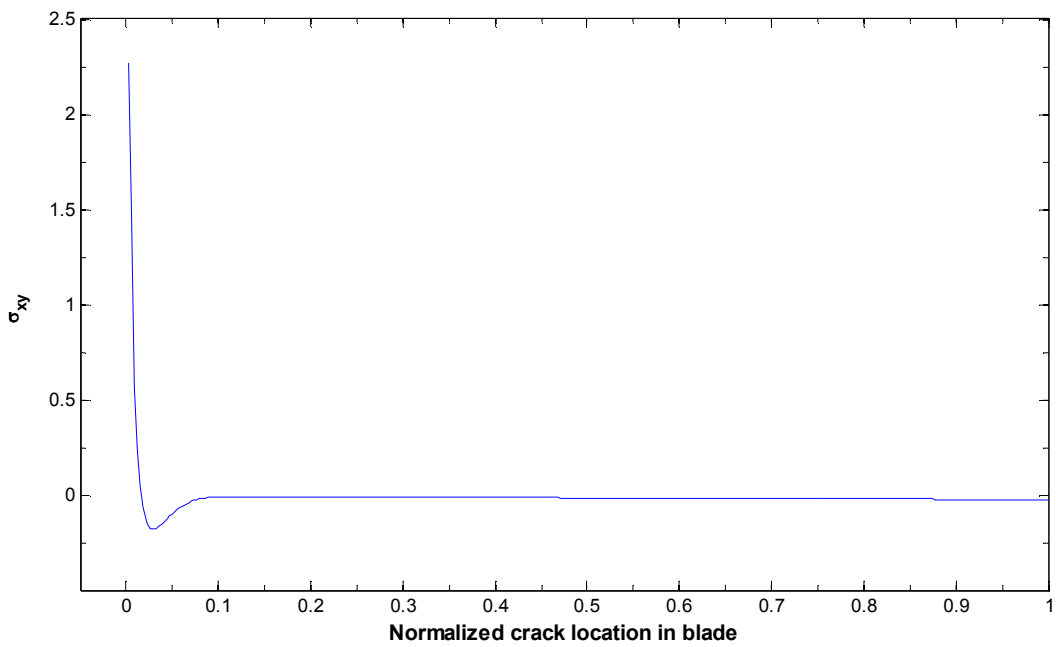

Figure 4.26: In-plane shear stress for edge-crack along entire length of blade.

Now that we have obtained the critical location for a single leading-edge crack to propagate, we plotted mixed-mode f for normalized loading with varying β, shown in Figure 4.27. We can see that because we assumed no shear effects on our blade, at $\beta = 0°$ the maximum f is obtained. We also can see this from Figure 4.28 and Figure 4.29. Maximum K_I is located at $\beta = 0°$ while the minimum K_{II} is located at $\beta = 0°$. Also, maximum K_{II} values are located when β is around 45°.

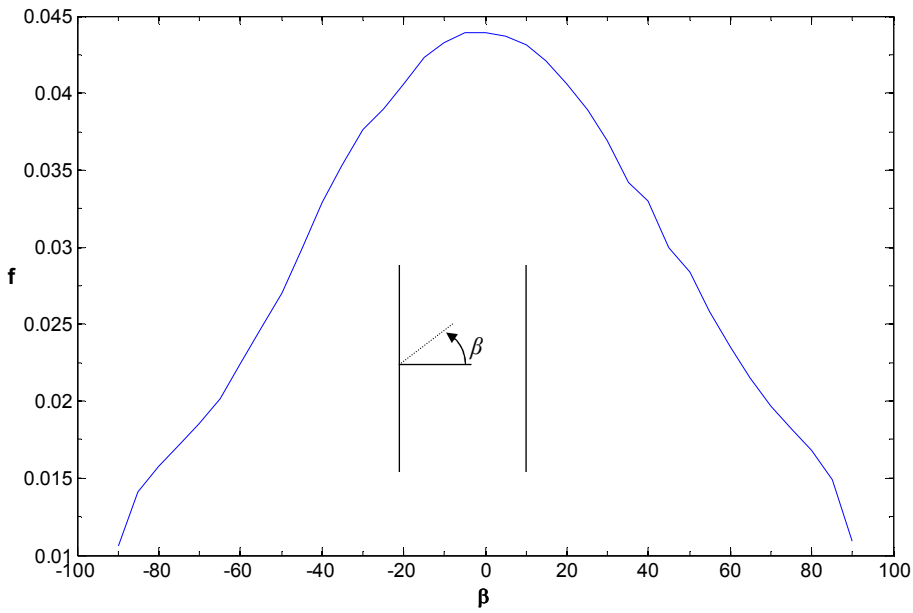

Figure 4.27: Mixed-mode *f* for single edge-crack with varying *β*.

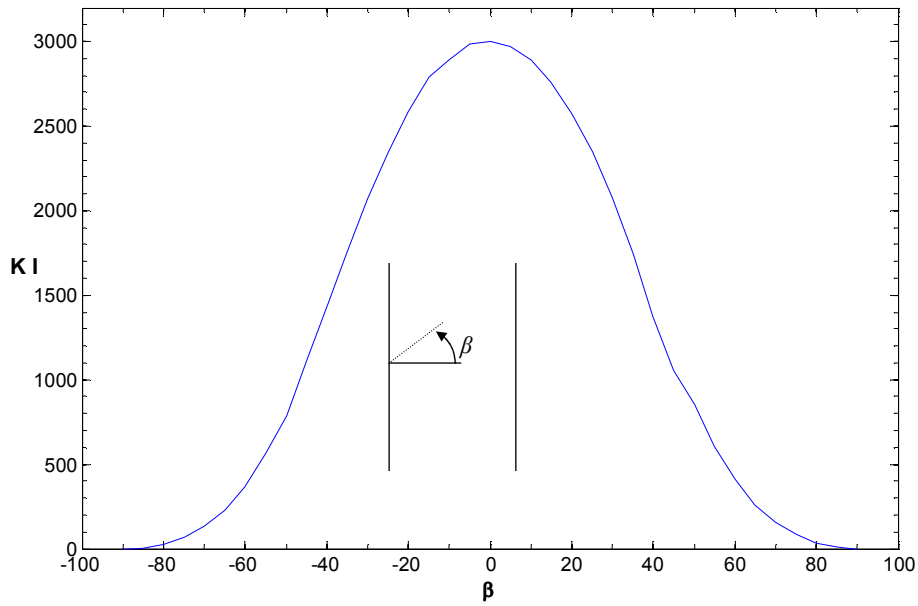

Figure 4.28: K_I for single edge-crack with varying β.

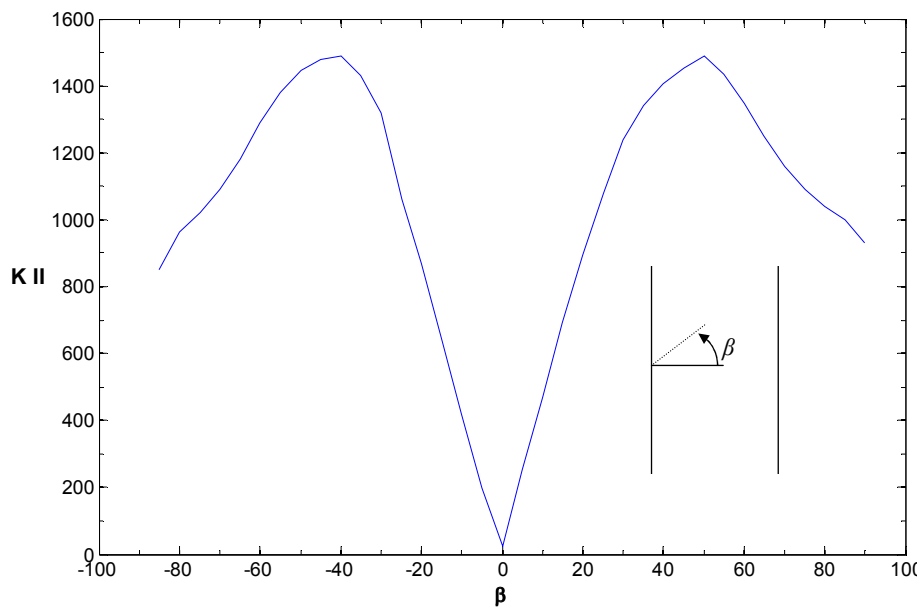

Figure 4.29: K_{II} for single edge-crack with varying β.

4.3.5: CASE 5: XFEM FATIGUE ANALYSIS

Figure 4.30 assumes that the SIF on the crack is constant and equal to the maximum *mode I* SIF on the whole front. The results show *mode I* SIF of a cracked blade on its most critical location with respect to the duty cycles. When the crack reaches a total length of approximately 15% of the total blade width, total failure occurs on the blade. Both plots show that the remaining duty cycles occur at the same value.

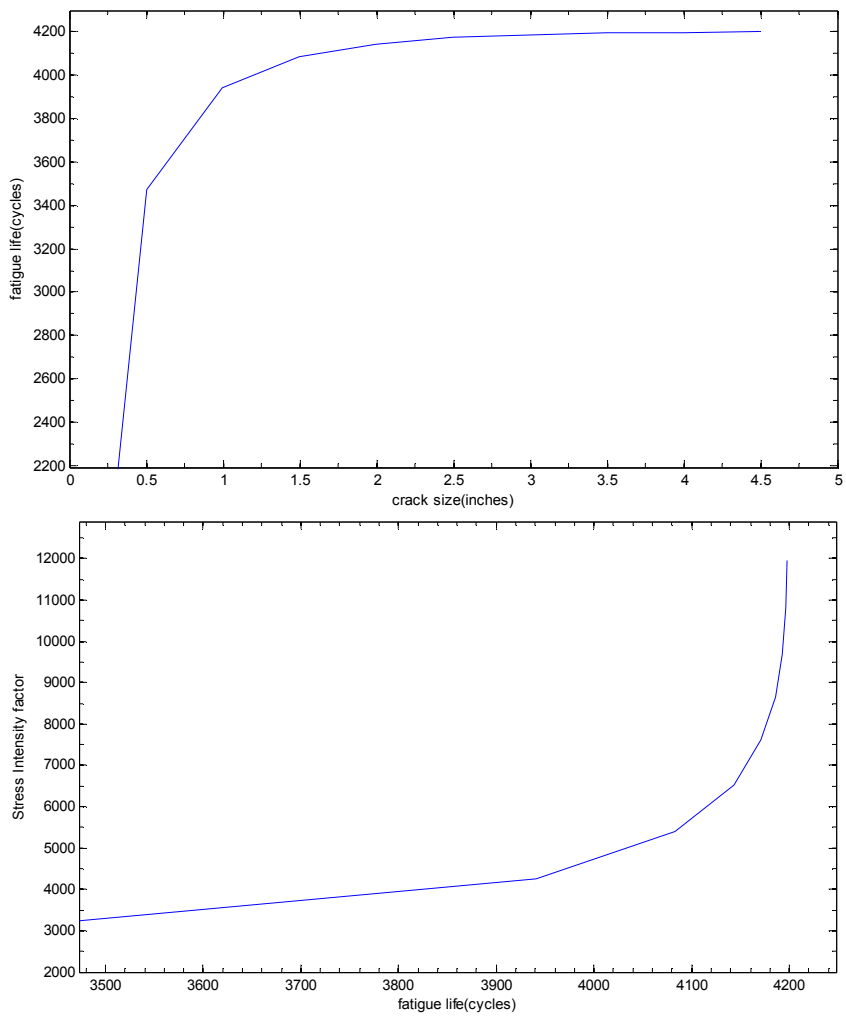

Figure 4.30: Remaining of duty cycles for an edge crack.

The two-dimensional mesh of the blade with the propagated crack is shown in Figure 4.31. Also, stress plots of the studied blade are shown in Figure 4.32. We can see that the maximum registered stress value is located around the crack tip area.

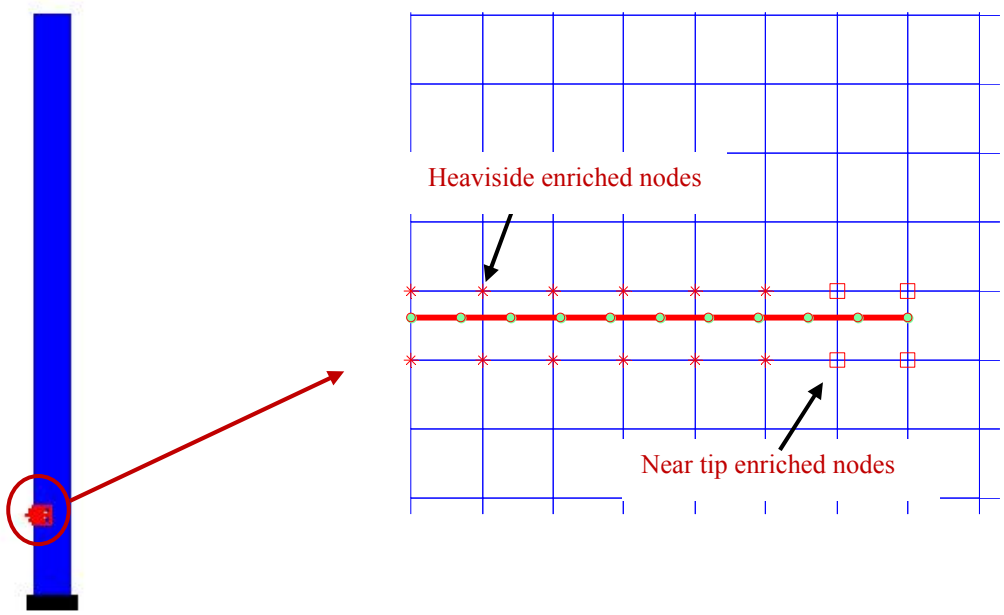

Figure 4.31: Two-dimensional blade mesh with propagated crack on critical location.

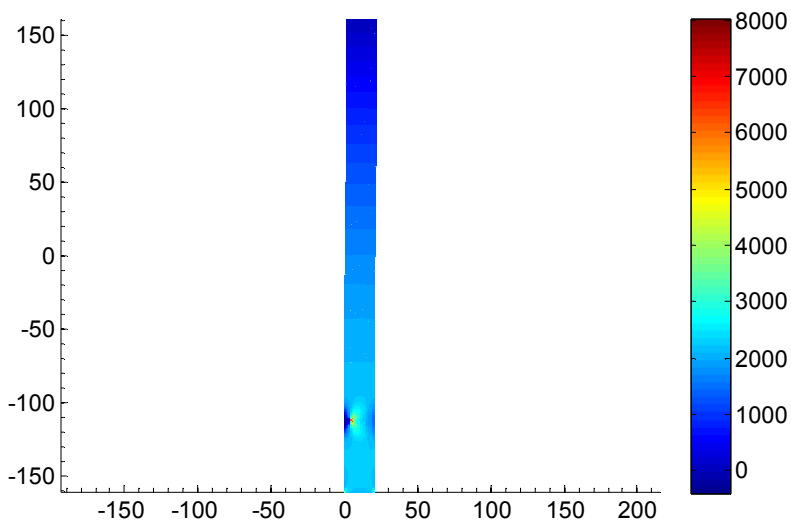

Figure 4.32: Main stress σ_{yy} on blade.

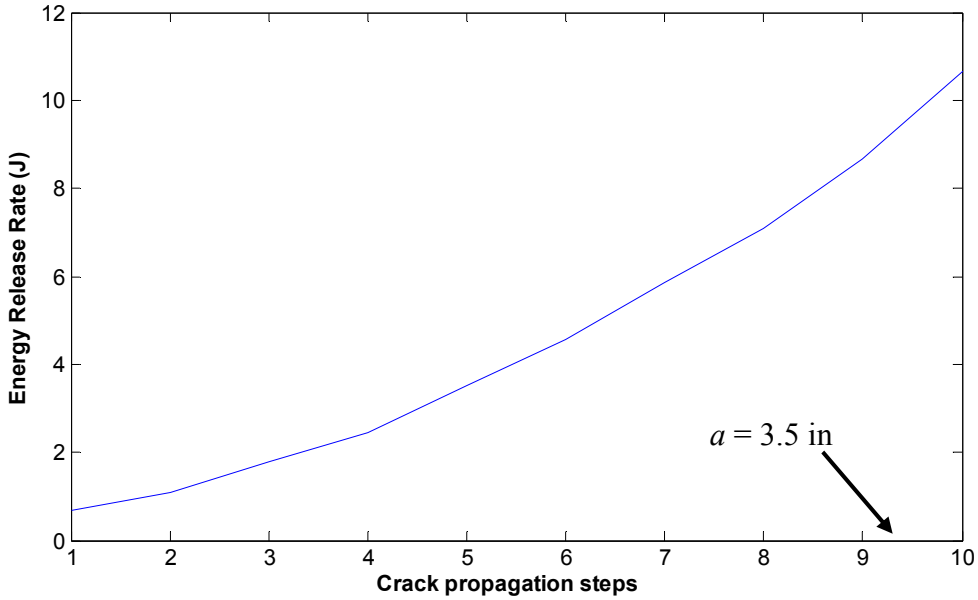

Figure 4.33: Energy Release Rate *(J)* for each propagation step.

Figure 4.33 shows the Energy Release Rate (J) for every propagation step. In this plot we can see how energy is being released in the blade at every propagation step. The maximum value of *J* is located at the last propagation step before total blade failure.

CHAPTER 5: FINAL REMARKS

5.1: CONCLUSIONS

The body forces and the fatigue analysis were implemented into XFEM. Results show that the critical location due to a leading-edge crack of the blade is around 8% of the center hub fixed end. The critical location might change as we include other effects ignored in this work. The results show a promising mixed-mode fatigue analysis using XFEM for rotating two-dimensional structures. A crack located at 8% of the center hub will reach a maximum of 15% of the total blade's width before it fails catastrophically.

5.2: FUTURE WORK AND RECOMMENDATIONS

Future work is necessary for the improvement of helicopter rotary blade fatigue analysis. In this work, we only included constant rotational velocity, and a work which includes tangential acceleration will become an instant upgrade in the search for simulating rotary blade fatigue life. Tangential accelerations will create in-plane shear, and it is motivating to know how this shear effect will affect the blade's total duty cycles. Also, extensive studies can be done regarding aeroelasticity effects on the blades. We have to remember that rotary blades are subjected to elastic loads, which includes lift forces as well as drag forces, and vibration due to actual flight characteristics. Bending caused by lift forces would make the problem a three-dimensional one, and therefore, there will be greater computational costs. Aerodynamic loads, like wind effects caused by the other blades, will also affect the blade's duty cycles.

Although extensive work can be done regarding different loading types, work can be done using multi-crack scenarios. A typical rotating blade may be subjected to more than one crack; this may or may not propagate simultaneously. Having a multi-crack blade configuration can cause eccentricity to the blade. Also, cracks can interact with each other, creating a significant not-continuous decrease in the blade's remaining duty cycles.

In this work, no contact effect was implemented. Near the crack tip nodes may encounter contact interaction, thus creating temporary new bonds between nodes which were initially

enriched due to crack propagation. This contact bonds will create spontaneous rigidity to already enriched nodes and this can cause spontaneous changes in crack tip direction.

BIBLIOGRAPHY

1. *Failure assessment Diagrams*, in *failure Analysis and Prevention*. 2002, ASM handbook. p. 243-249.
2. *army-technology*. 1999-2010 [cited; Available from: http://www.army-technology.com/terms.html.
3. *Flight Proven PurePower(TM) PW1000G Demonstrator Engine on Display at Paris Air Show*. 2009 [cited; Available from: http://www.pw.utc.com/Media+Center/Press+Releases/Flight+Proven+PurePower%28TM%29+PW1000G+Demonstrator+Engine+on+Display+at+Paris+Air+Show.
4. Kijk, P.V. *Rotor Research Pty Ltd/as Brumby Helicopters*. 1995-2010 [cited; Available from: http://brumbyhelicopters.com.au/metalmemory.htm.
5. Algera, D., Iyyer, N., Hong, C. H., Sarkar, S., Singh, A. Bradfield, S., *Rotary Wing Structural Life Tracking Architecture.* American Helicopter Society 66th Annual Forum, May 11-13, 2010.
6. Arms, S.W., Moon, S.M., Phan, N. *Energy Harvesting Wireless Sensors for Helicopter Damage Tracking*. in *AHS International Forum*. May 11 2006. Phoenix, AZ: American Society International, Inc.
7. Technics.Com, T. *Thai Technics.Com*. 2010 [cited; Available from: http://www.thaitechnics.com/helicopter/heli_intro.html.
8. Fries, J.C., *Black Hawk helicopter Vibration Analysis Due to Main Rotor Damage.* Army Research Laboratory, 2001: p. 1-27.
9. Cappelli, M.D., Kim, W., Urban, M.R., Kumar,R.S., Gurvich, M.G., Centolanza, L., *The Reduction of Composite Main Rotor Blade Maintenance: A practical approach.* Applied Mechanics Review, March 2004. **57**(No. 2).
10. Boyer, R., Welsch, G., Collings, E. W., *Materials Properties Handbook: Titanium Alloys*, in *ASM International*. 1994: Materials Park, OH.
11. ANSYS, *Academic Research*. 12.1.
12. Bordas, S., Rabczuk, T. Zi, G., *Three-dimensional crack initiation, propagation, branching and junction in non-linear materials by and extended meshfree method without asymptotic enrichment.* 2006.
13. Bordas, S. and B. Moran, *Enriched finite elements and level sets for damage tolerance assessment of complex structures.* Engineering Fracture Mechanics, 2006. **73**(9): p. 1176-1201.
14. Bordas, S., et al., *An extended finite element library.* International Journal for Numerical Methods in Engineering, 2006. **2**: p. 1-33.
15. Bordas, S.P.A., et al., *Strain smoothing in FEM and XFEM.* Computers & Structures. **88**(23-24): p. 1419-1443.
16. Bordas, S.R., T. Zi, G., *Three-dimensional crack initiation, propagation, branching and junction in non-linear materials by an extended meshfree method without asymptotic enrichment.* Dec. 13 2006.
17. MATLAB, *The Mathworks, Inc.* 2010.
18. Liu, Y., Mahadevan, S., *Threshold stress intensity factor and crack growth rate prediction under mixed-mode loading.* Engineering Fracture Mechanics, August 8, 2006.
19. Kaiyuan, L., L. Shuyao, and L. Guangyao, *A simple and less-costly meshless local Petrov-Galerkin (MLPG) method for the dynamic fracture problem.* Engineering Analysis with Boundary Elements, 2006. **30**(1): p. 72-76.
20. Biaecki, R.A., et al., *Coupling BEM, FEM and analytic solutions in steady-state potential problems.* Engineering Analysis with Boundary Elements, 2002. **26**(7): p. 597-611.

21. Armentani, E. and R. Citarella, *DBEM and FEM analysis on non-linear multiple crack propagation in an aeronautic doubler-skin assembly.* International Journal of Fatigue. **28**(5-6): p. 598-608.
22. Rabczuk, T. and T. Belytschko, *A three-dimensional large deformation meshfree method for arbitrary evolving cracks.* Computer Methods in Applied Mechanics and Engineering, 2007. **196**(29-30): p. 2777-2799.
23. Kettil, P., et al., *Strength and deformation of arbitrary beam sections using adaptive FEM.* Computers & Structures, 2007. **85**(1-2): p. 15-29.
24. Maligno, A.R., et al., *A three-dimensional (3D) numerical study of fatigue crack growth using remeshing techniques.* Engineering Fracture Mechanics. **77**(1): p. 94-111.
25. Malvar, L.J. and M.E. Fourney, *A three dimensional application of the smeared crack approach.* Engineering Fracture Mechanics, 1990. **35**(1-3): p. 251-260.
26. Goyal, V.K., Rome, J. I. *An Improved Cohesive Zone Model for Low Strength Materials*. in *50th AIAA Structures, Structural Dynamics, and Materials Conference*. May 4-7 2009. Palm Springs, CA.
27. Goyal, V.K., Rome, J. I., Schubel, P.M. *Structural Analysis of Solid Rocket Motor Cases*. in *49th AIAA Structures, Structural Dynamics, and Materials Conference*. April 7-10, 2008. Schaumburg, IL.
28. Goyal, V.K., Rome, J. I., Schubel, P.M. *Predicting Damage of a Composite Sandwich Structure Subjected to Low Velocity Impact*. in *Proceedings of the American Society for Composites, 22th Technical Conference*. September 2007. Seattle, WA.
29. Goyal, V.K., Rome, J. I., Schubel, P.M. *Enhancement to the Interfacial Element Formulation for the Prediction of Delamination*. in *AIAA Structures, Structural Dynamics, and Materials Conference*. April 2007. Honolulu, HI.
30. Goyal, V.K., Rome, J. I. *Failure Modeling and Simulation of Composites Subjected to Bypass and Bearing Loads*. in *47th AIAA Structures, Structural Dynamics, and Materials Conference*. May 2006. Newport, RI.
31. Goyal, V.K., Rome, J. I., Klug, J. C. *Burst Pressure Predictions of Composite Cylindrical Vessels with Wrinkled Plies*. in *41st AIAA/ASME/SAE/ASEE Joint Propulsion Conference and Exhibit*. July 2005. Tucson, Arizona.
32. Goyal, V.K., Johnson, E. R. *Cohesive-Decohesive Interfacial Constitutive Law for the Analyses of Fatigue Crack Initiation and Growth*. in *44th AIAA Structures, Structural Dynamics, and Materials Conference*. April 2003. Norfolk, Virginia.
33. Hutchinson, J.W., *behavior at the end of tensile crack tip in a hardening material.* Journal of the Mechanics and Physics of Solids, 1968. **16**: p. 13-31.
34. Rice, J.R., Ben-Zion, Y., Kim, K. S., *Three-dimensional perturbation solution for a dynamic planar crack moving unsteadily in a model elastic solid.* Journal of the Mechanics and Physics of Solids, 1994. **42**(813-843).
35. Gurson, A.L., *Continuum theory of ductile rupture by void nucleation and growth: Part I - Yield criteria and flow rules for porous ductile media.* Journal of Engineering Materials and Technology, 1977. **99**: p. 2-15.
36. Xu, X.P., Needleman, A., *Numerical Simulations of Fast Crack-Growth in Brittle Solids.* Journal of The Mechanics And Physics of solids, 1994. **42**(9).
37. Xu, X.P., Needleman, A., *Numerical simulations of dynamic crack growth along an interface.* International Journal of Fracture, 1996. **74**: p. 289-324.
38. Camacho, G.T., Ortiz, M., *Computational modeling of impact damage in brittle materials.* International Journal of Solids and Structures, 1996. **33**: p. 2899-2938.
39. Park, K., Paulino, G. H., Roesler, J. R., *A unified potential-based cohesive model of mixed-mode fracture.* Journal of the Mechanics and Physics of Solids, 2009. **57**(6): p. 891-908.

40. Xiao, Q.Z. and B.L. Karihaloo, *Implementation of hybrid crack element on a general finite element mesh and in combination with XFEM.* Computer Methods in Applied Mechanics and Engineering, 2007. **196**(13-16): p. 1864-1873.
41. Belytschko, T., Black, T., *Elastic Crack Growth in Finite Elements with Minimal Remeshing.* International Journal of Fracture Mechanics, October 3, 1998.
42. Vigneron, L., *FEM/XFEM-Based Modeling of Brain Shift, Resection, and Retraction for Image-Guided Surgery*, in *Department of Signal Processing*. Febrary 26 2009, University of Liege. p. 150.
43. Logé, R.E., Béringhier, M., Chastel, Y. B., Delannay, L. *Reducing Computational Cost and Allowing Automatic Remeshing in FEM Models of Metal Forming Coupled With Polycrystal Plasticity.* in *AIP Conference Proceedings*. 2007: MATERIALS PROCESSING AND DESIGN; Modeling, Simulation and Applications.
44. Moës, N., Dolbow, J., Belytschko, T., *A Finite Element Method for Crack Growth Without Remeshing.* International Journal of Numerical Methods in Engineering, 1999. **46**: p. 131-150.
45. Chahine, E., P. Laborde, and Y. Renard, *A non-conformal eXtended Finite Element approach: Integral matching Xfem.* Applied Numerical Mathematics. **In Press, Corrected Proof**.
46. Richardson. C., H.J., Sifakis., E., Hellrung, J., *Simulating crack propagation with XFEM and a hybrid mesh.* International Journal for Numerical Methods in Engineering, 2009. **18**(2.02).
47. Rabczuk, T., S. Bordas, and G. Zi, *On three-dimensional modelling of crack growth using partition of unity methods.* Computers & Structures. **88**(23-24): p. 1391-1411.
48. Bao, W., H. Han, and Z. Huang, *Numerical simulations of fracture problems by coupling the FEM and the direct method of lines.* Computer Methods in Applied Mechanics and Engineering, 2001. **190**(37-38): p. 4831-4846.
49. Goyal, V.K., E.R. Johnson, and C.G. Dávila, *Irreversible constitutive law for modeling the delamination process using interfacial surface discontinuities.* Composite Structures, 2004. **65**(3-4): p. 289-305.
50. Enderlein, M., A. Ricoeur, and M. Kuna, *Comparison of finite element techniques for 2D and 3D crack analysis under impact loading.* International Journal of Solids and Structures. **40**(13-14): p. 3425-3437.
51. Tilbrook, M.T., R.J. Moon, and M. Hoffman, *Finite element simulations of crack propagation in functionally graded materials under flexural loading.* Engineering Fracture Mechanics, 2005. **72**(16): p. 2444-2467.
52. Liu, Y., L. Liu, and S. Mahadevan, *Analysis of subsurface crack propagation under rolling contact loading in railroad wheels using FEM.* Engineering Fracture Mechanics, 2007. **74**(17): p. 2659-2674.
53. Combescure, A., et al., *X-FEM a good candidate for energy conservation in simulation of brittle dynamic crack propagation.* Computer Methods in Applied Mechanics and Engineering, 2008. **197**(5): p. 309-318.
54. Grégoire, D., et al., *Dynamic crack propagation under mixed-mode loading - Comparison between experiments and X-FEM simulations.* International Journal of Solids and Structures, 2007. **44**(20): p. 6517-6534.
55. Menk, A. and S.P.A. Bordas, *Crack growth calculations in solder joints based on microstructural phenomena with X-FEM.* Computational Materials Science. **50**(3): p. 1145-1156.
56. Xu, Y. and H. Yuan, *Computational analysis of mixed-mode fatigue crack growth in quasi-brittle materials using extended finite element methods.* Engineering Fracture Mechanics, 2009. **76**(2): p. 165-181.
57. Ayhan, A.O., *Three-dimensional fracture analysis using tetrahedral enriched elements and fully unstructured mesh.* International Journal of Solids and Structures. **48**(3-4): p. 492-505.

58. Motamedi, D. and S. Mohammadi, *Dynamic analysis of fixed cracks in composites by the extended finite element method.* Engineering Fracture Mechanics. **77**(17): p. 3373-3393.
59. Nagashima, T. and H. Suemasu, *X-FEM analyses of a thin-walled composite shell structure with a delamination.* Computers & Structures. **88**(9-10): p. 549-557.
60. Budyn, E., Hoc, T., *Multiple scale modeling for cortical bone fracture in tension using X-FEM.* European Journal of Computational Mechanics, 16/2007: p. 215-238.
61. Fries, T.P., Belytsschko, T, *The extended/generalized finite element method: An overview of the method and its applications.* International Journal for Numerical Methods in Engineering, 2000.
62. Sib, G.C., *Handbook of Stress Instensity Factors for Researchers and Engineers.* Institute of Fracture and Solid Mechanics, Lehigh University, Bethlehem, Pa 1973.
63. Goyal, V.K., Johnson, E. R., *Predictive Strength-Fracture Model for Composite Bonded Joints.* Composite Structures, 2008. **82**: p. 434-446.
64. NOEL, D., *Crack Simulation With Extended Finite Element Methods*. August 24, 2008.
65. Rice, J.R., *A Path Independent Integral and the Approximate Analysis of Strain Concentration by Notches and Cracks.* Journal of Applied Mechanics, 1968. **35**: p. 379-386.
66. Mayer, H., C. Ede, and J.E. Allison, *Influence of cyclic loads below endurance limit or threshold stress intensity on fatigue damage in cast aluminium alloy 319-T7.* International Journal of Fatigue, 2005. **27**(2): p. 129-141.
67. Goyal, V., Goyal, V., *Aircraft Structures for Engineers*. 2010, Mechanical Engineering Department, University of Puerto Rico at Mayaguez. p. 1276.
68. Budynas, R.G., Nisbett, J.K., *Shigley's Mechanical Engineering Design*, ed. B. Stenquist. Vol. eighth. 2008, New York: Mc-Graw-Hill. 234-235.
69. Pugno, N., et al., *A generalized Paris' law for fatigue crack growth.* Journal of the Mechanics and Physics of Solids, 2006. **54**(7): p. 1333-1349.
70. Moës, N., et al., *A computational approach to handle complex microstructure geometries.* Computer Methods in Applied Mechanics and Engineering, 2003. **192**(28-30): p. 3163-3177.
71. Jovicic, G., Zivkovic, M. Jovicic, N., *Extended Finite Element Method for Two-dimesional Crack Modeling.* Journal of the Serbian Society for Computational Mechanics, 2007. **1**(1): p. 184-196.
72. Sumi, Y., Yang, C., Wang, Z., *Morphologi cal aspects of fatigue crack propagation. Part II - effects of stress biaxiality and welding residual stresses.*, in *Department of Naval Archetecture and Ocean Engineering*. 1995, Yokohama National University: Yokohama, Japan.
73. Mohammadi, S., in *Discontinuum Mechanics by Combined Finite/Discrete Elements*. 2003, WIT Press: Southampton, Boston.
74. Liang, J., Huang, R., Prevost, J., Suo, Z., *Evolving crack patterns in thin films with the extended finite element method.* International Journal of Solids and Structures, 2003. **40**: p. 2343-2354.

APPENDIX A: THEORY BEHIND XFEM

In this chapter we will discuss the theory behind the extended finite element method (XFEM). Then we will explain how FEM works involving Linear Elastic Fracture Mechanics (LEFM) and the limitation FEM has regarding LEFM.

A.1 THE XFEM NUMERICAL APPROACH

XFEM is a numerical method that enables a local enrichment of approximation spaces. This technique was introduced at the end of the 20th century. The advantage of this technique is that mesh is independent from the crack geometry, while in the most of the FEM application; mesh should be created along the crack geometry. However, XFEM does not need to consider the crack geometry when is created. The enrichment is realized through the partition of unity concept. The method is useful for the approximation of solutions with pronounced non-smooth characteristics in small parts of the computational domain, for example near discontinuities and singularities. In these cases, standard numerical methods such as the FEM exhibit poor accuracy. The XFEM offers significant advantages by enabling optimal convergence rates for these applications.

This technique first introduced in 1999 by a research group directed by Ted Belytschko [41] at Northwestern University. Two main concepts of XFEM are explained. Both of them are enriching technique by using special function and adding extra degree of freedom. One of them is adding singular expression and the other is adding discontinuous expression in which allows the element to have two different strain and stress field. Equation **Error! Reference source not found.** is the general XFEM expression. First term represents the general FEM approximation of the displacement field. The second term applies a Heaviside enrichment function at the nodes being split by the crack. The basic concept is adding singularity field so that FEM displacement approximation achieve singular field to crack split elements. Finally, the third term gives and enrichment to the nodes included in the crack tip element.

$$u(x,y) = \underbrace{\sum_{i \in n_s} N_i\, u_i}_{\text{Standard FEA nodes}} + \underbrace{\sum_{i \in n_h} N_i\, \psi_i\, a_{x_i}}_{\text{Heaviside enriched nodes}} + \underbrace{\sum_{i \in n_f} \sum_{j=1}^{4} N_i\, \varphi_j\, b_{x_i}^{\,j}}_{\text{Near field tip nodes}} \tag{A.1}$$

$$v(x,y) = \underbrace{\sum_{i \in n_s} N_i\, v_i}_{\text{Standard FEA nodes}} + \underbrace{\sum_{i \in n_h} N_i\, \psi_i\, a_{y_i}}_{\text{Heaviside enriched nodes}} + \underbrace{\sum_{i \in n_f} \sum_{j=1}^{4} N_i\, \varphi_j\, b_{y_i}^{\,j}}_{\text{Near field tip nodes}} \tag{A.2}$$

By applying the discontinuity, we can express two different strain fields in one element. This means that the strain expression in one side of the crack is different from the other side of the crack. In Figure A. 1 region I and II are in the same element but different fields due to the discontinuous function. Also, two dash lines in the picture are assumed as two crack edge.

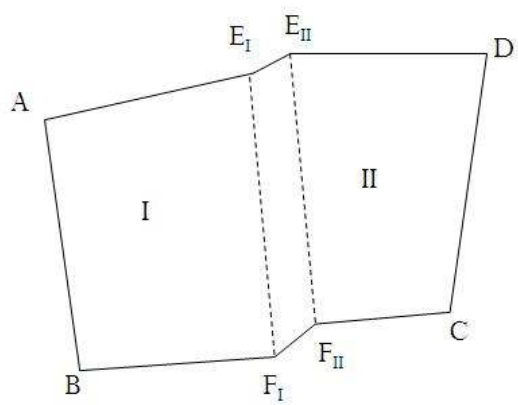

Figure A. 1: Enriched Element with discontinuous function

A.2 STRUCTURE ANALYSIS

One of the important applications of FEM is the analysis of crack propagation problems. Fundamentals of the present form of the linear elastic fracture mechanics (LEFM) came to the existence practically in naval laboratories during the First World War. Since then, LEFM has been successfully applied to various classical crack and defect problems, but remained relatively limited to simple geometries and loading conditions.

Progressive failure/fracture analysis of structures has been an active subject of research for many years. Historically, it was addressed either within the framework of continuum mechanics, including computational plasticity and damage mechanics, or the discontinuous approach of fracture mechanics. These methods, however, are applied to fundamentally different classes of failure problems. While the theory of plasticity and damage mechanics are basically designed for problems where the displacement field and usually the strain field remain continuous everywhere (continuous problems), fracture mechanics is essentially formulated to deal with strong discontinuities or "cracks" where both the displacement and strain fields are discontinuous across a crack surface, seen in Figure A. 2.

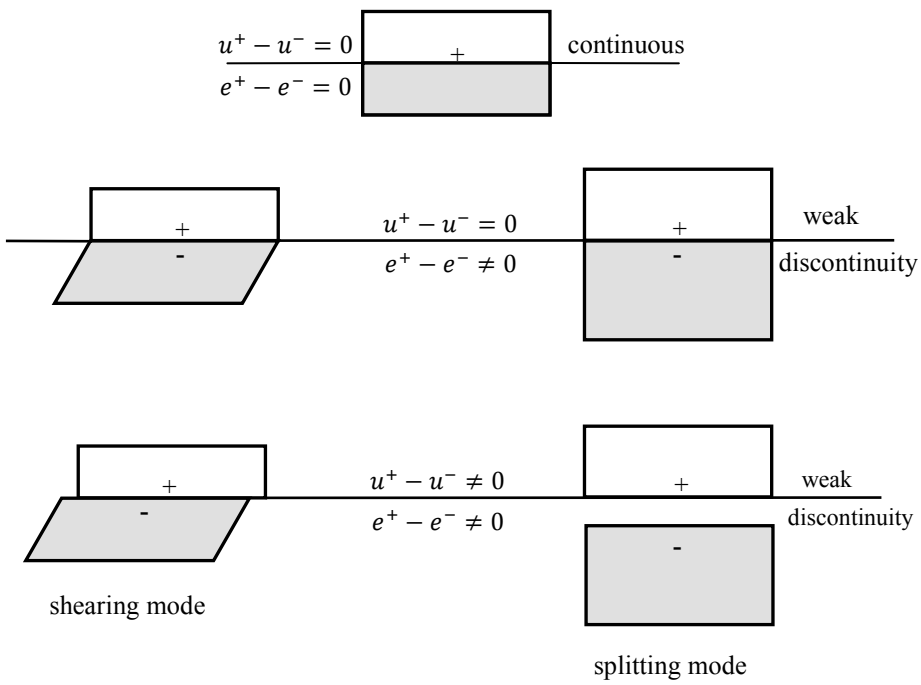

Figure A. 2: Different categories of continuities

In practice, fracture mechanics is also used for weak discontinuity problems, and both damage mechanics and the theory of plasticity have been modified and adapted for failure/fracture analysis of structures with strong discontinuities. It is, therefore, difficult to distinguish between the practical engineering applications exclusively associated with each class of analytical methods.

Global (non-local) energy based methods were gradually developed and solutions for classical problems were also obtained. Energy based methods allowed the classical fracture mechanics to be extended to nonlinear problems. Introduction of the J integral was a major breakthrough that allowed powerful numerical methods such as the finite element method to be efficiently used for determining the necessary fields and variables.

A.3 CRACK MODELING

Analytical, semi-analytical and numerical approaches, such as the boundary integral method, the boundary element method, the finite element method and recently a number of meshless methods, have been successfully used for modeling cracks; each one provides advantages and drawbacks in handling certain parts of the simulation. Although the same concepts can be more or less applied to many numerical methods, this thesis work emphasizes on the finite element method as a basis for its extension to the extended finite element method.

Crack simulation in the finite element method has been performed by a number of methods. They include the continuous smeared crack model and several discontinuous approaches such as the discrete inter-element crack model, the discrete crack model and the discrete element based model. Recently a new class has been proposed that simulates the singular nature of discrete models within a geometrically continuous mesh of finite elements. The extended finite element method has emerged from this class of problems, and is based on the concept of partition of unity for enriching the classical finite element approximation to include the effects of singular or discontinuous fields around a crack.

A.4.1 Enriched Elements

A special set of enriched shape functions are used to simulate singular or discontinuous displacement field within a finite element. This enriched shape functions allow for accurate approximation of the displacement field, seen in Figure A.3**.** This figure illustrates a model in which the crack path is through the middle of a finite element. As you can see, the mesh does not need to conform to the crack path and the crack is not geometrically modeled. In order to account for the effects of a crack or discontinuity, Moës [44] proposed additional enrichment approximation is added to the classical finite element model.

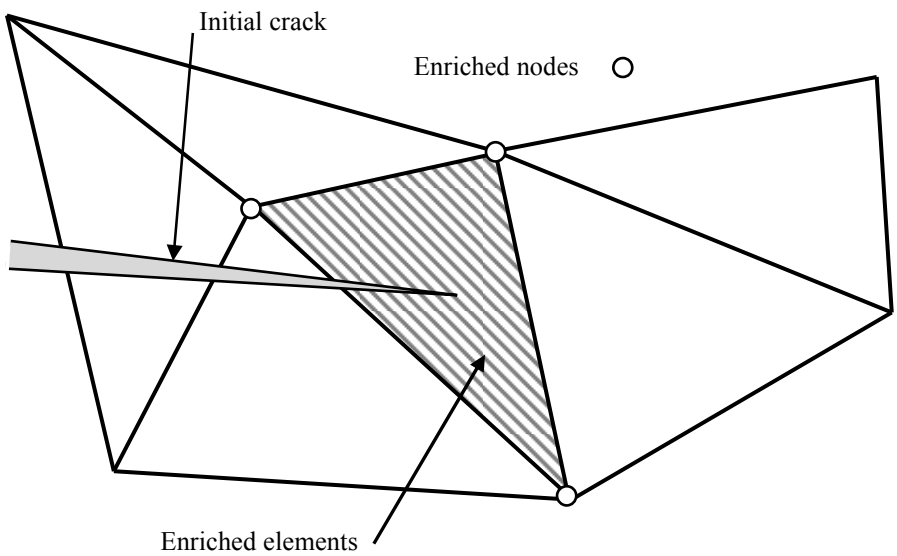

Figure A. 3: Crack tip with enriched nodes

This method does not require any remeshing in the process of crack propagation. It also automatically determines the elements around the crack/tip and generates necessary enrichment functions for the associated finite elements or nodal points. Locations of initial cracks or potential propagation paths do not affect the way the initial finite element model is constructed. Multiple cracks, including intersecting cracks, may be simulated by the same finite element mesh with comparable levels of accuracy.

A.4 XFEM FOR ISOTROPIC STRUCTURES

The basic concept of XFEM is to enrich the approximation space so that it is capable of reproducing certain features of the problem of interest, in particular discontinuities such as cracks or interfaces. In the extended finite element method, the usual finite element mesh is produced. Then, by considering the location of discontinuities, degrees of freedom are added to the classical finite element model in selected nodes near to the discontinuities to provide a higher level of accuracy.

A.4.1 Basic XFEM Approximation

Consider *x*, a point in a finite element model. Also assume there is a discontinuity in the arbitrary domain discretized in some *n* node finite elements. In XFEM the following is used to calculate the displacement for the point *x* locating within the domain.

$$u^h(x) = u^{FE} + u^{enr} = \sum_{j=1}^{n} N_j(x)\, u_j + \sum_{k=1}^{m} N_k(x)\, \phi(x) a_k \qquad \textbf{(A.3)}$$

where:

$u_j \rightarrow$ vector of regular nodal degree of freedom in FEM.
$a_k \rightarrow$ added set of degrees of freedom to the standard finite element model.
$\varphi(x) \rightarrow$ enrichment functions defined for the set of nodes that the discontinuity has in its influence (support) domain.

The enrichment function $\varphi(x)$ can be chosen by applying appropriate analytical solution according to the type of discontinuity. The main objectives for using various types of enrichment functions within an XFEM procedure are:

1) Reproduce the singular field around a crack tip.
2) Continuity displacement between adjacent finite elements.
3) Independent strain fields in two differents sides of crack surface.
4) Other features according to the specific discontinuity problem.

A.4.2 Modeling Strong Discontinuous Fields

Approximation of a discontinuous displacement field is based on the definition of designed shape functions by the use of enrichment functions. The method is based on additional independent virtual degrees of freedom for the definition of the crack boundary and displacement field approximation. Combined with classical finite element method it will approximate the overall solution.

Figure A.4 show a one dimesion element consisting of four nodes and three finite elements with a crack in arbitrary location $x_c \xi_c$ within the middle element.

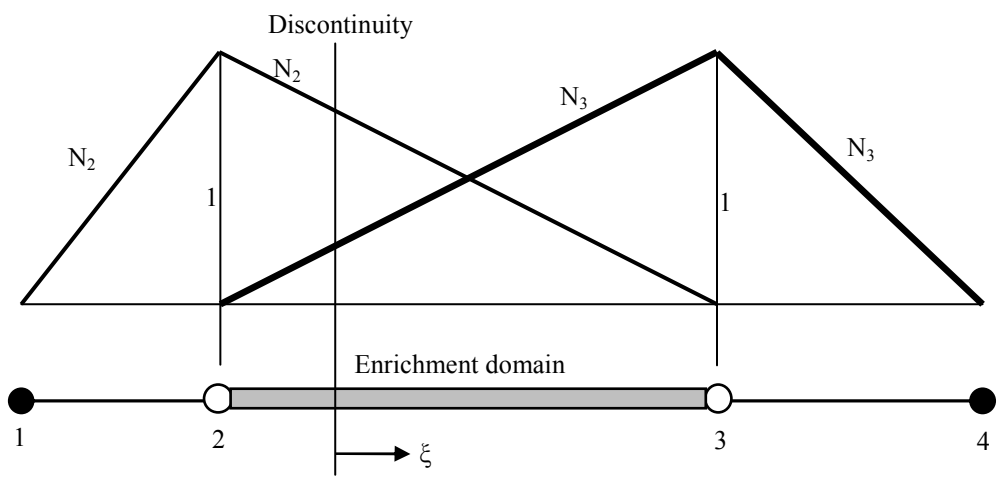

Figure A. 4: Simulation of crack in one-dim problem using linear finite element shape functions

In Figure (A.4)**,** nodes 2 and 3 are required to be enriched, whereas nodes 1 and 4 are not influenced by the crack. A type of simple enrichment function, the Heaviside function is discussed the next.

- **The Heaviside Function**

The Heaviside function $H(\xi)$ can be defined as a step function

$$H(\xi) = \begin{Bmatrix} 1 \ \forall \xi > 0 \\ 0 \ \forall \xi < 0 \end{Bmatrix} \tag{A.4}$$

A one-dimensional representation of this step function is shown in Figure A. 5.

Figure A. 6 illustrates the way the Heaviside "step" function simulates the discontinuity.

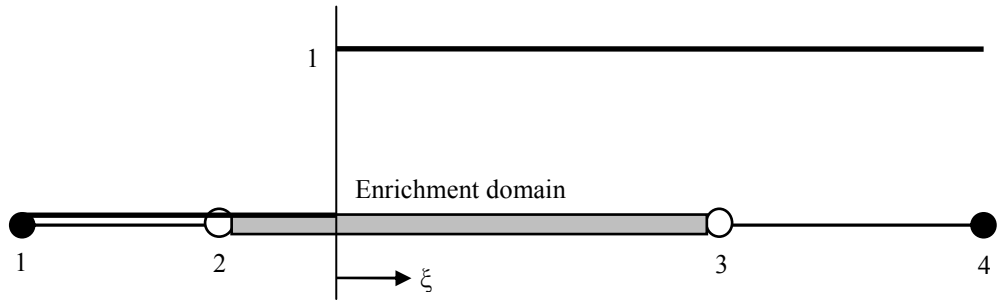

Figure A. 5: Representation of a step function.

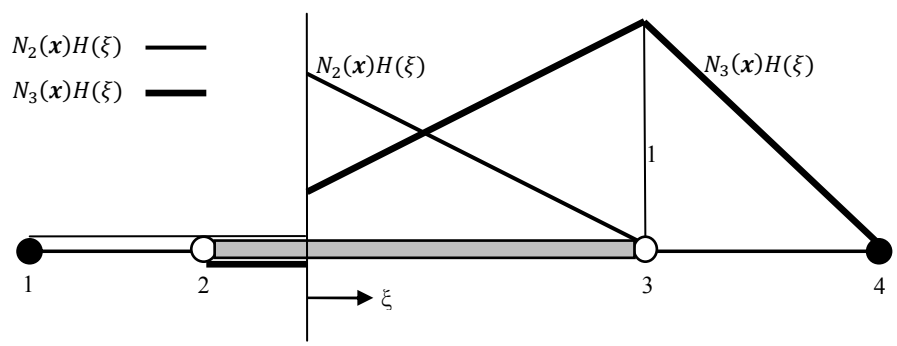

a) effect of the step function on shape functions

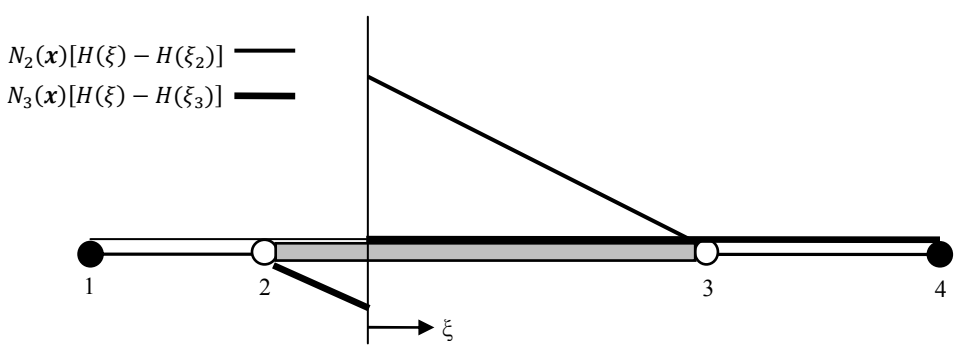

b) effect shifting on shape functions

Figure A. 6: Enriched shape functions for nodes 2 and 3 and applications of shifting Heaviside function.

With the use of the Heaviside Function, Eq. A.3) reads,

$$u^h(x) = \sum_{j=1}^{n} N_j(x)\, u_j + \sum_{k=1}^{m} N_k(x)\, H(\xi) a_k \tag{A.5}$$

Eq. (A.5) is not an interpolation and the nodal parameter u_i is not the real displacement value on the enriched node i. Simple remedy is to shift the step function around the node of interest:

$$u^h(x) = \sum_{j=1}^{n} N_j(x)\, u_j + \sum_{k=1}^{m} N_k(x) \left(H(\xi) - H(\xi)_{a_k}\right) \tag{A. 6}$$

In order to avoid numerical instabilities, following Heaviside function can also be used for a small value of β less than the element size.

$$\left\{ \begin{matrix} 0 & \xi < -\beta \\ \frac{1}{2} + \frac{\xi}{2\beta} + \frac{1}{2\pi} \sin\left(\frac{\pi\xi}{\beta}\right) & -\beta < \xi < \beta \\ 1 & \xi < -\beta \end{matrix} \right\} \tag{A. 7}$$

A.4.3 Modeling Weak Discontinuous Fields

Same as one-dimensional, only difference is the assumption of a weak discontinuity in arbitrary location $x_c(\xi_x)$ within the middle element. XFEM approximation is done replacing Heaviside function with an enrichment function $\chi(x)$

$$u^h(x) = \sum_{j=1}^{n} N_j(x)\, u_j + \sum_{k=1}^{m} N_k(x)\, \chi(x) a_k, \qquad \chi(x) = |\xi(x)| - |\xi(x_k)| \tag{A. 8}$$

Figure A. 77(a) illustrates these signed distance functions for the simple one-dimensional problem. As an effect of enrichment by the weak discontinuous enrichment functions, the original shape functions are transformed. According to Figure A. 7b**,** a kink in the displacement field is introduced. As a result, a jump in its derivative, discontinuity in the gradient of the function is anticipated.

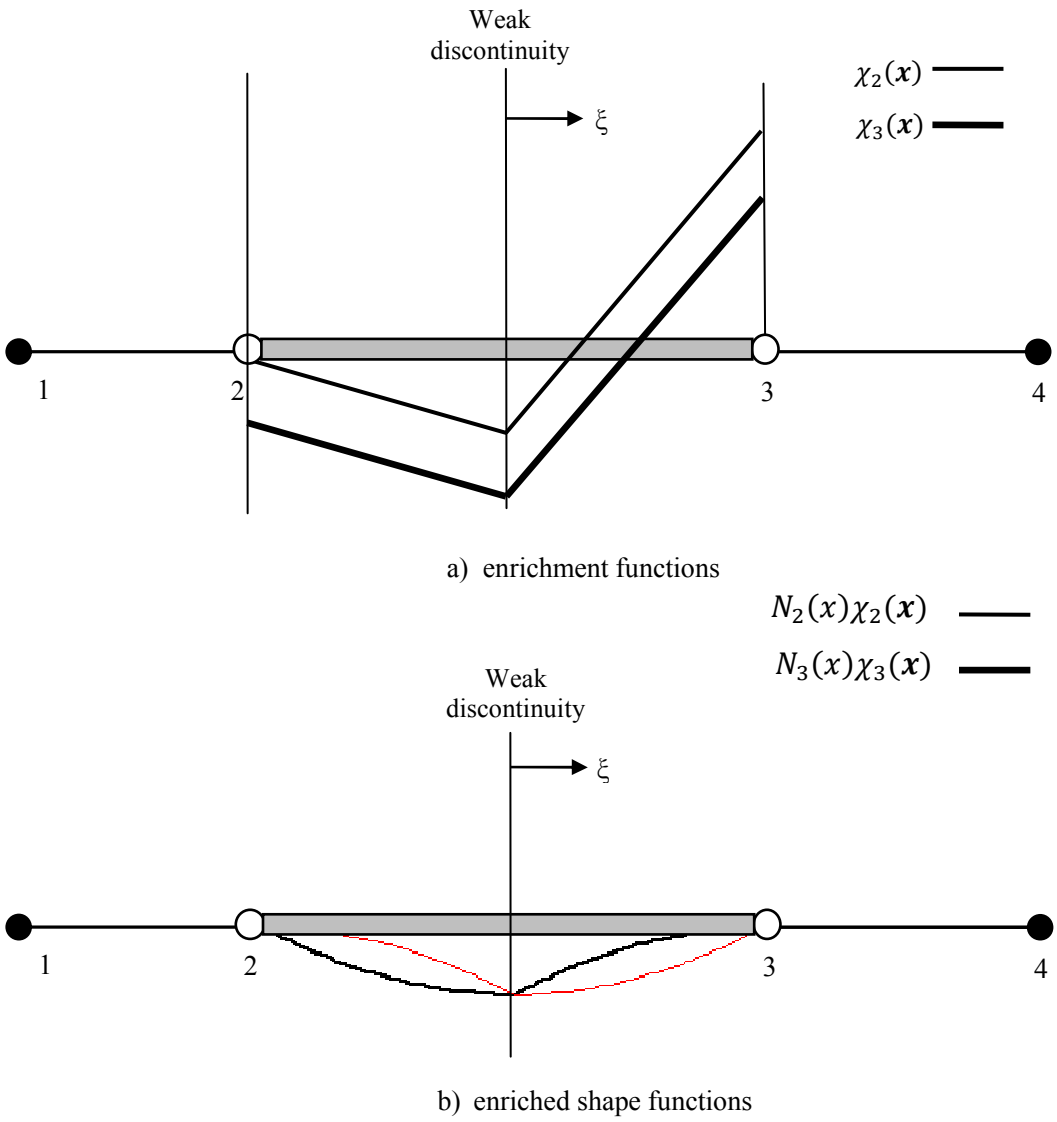

Figure A. 7: a) Weak discontinuous enrichment functions. b) Final enriched shape function.

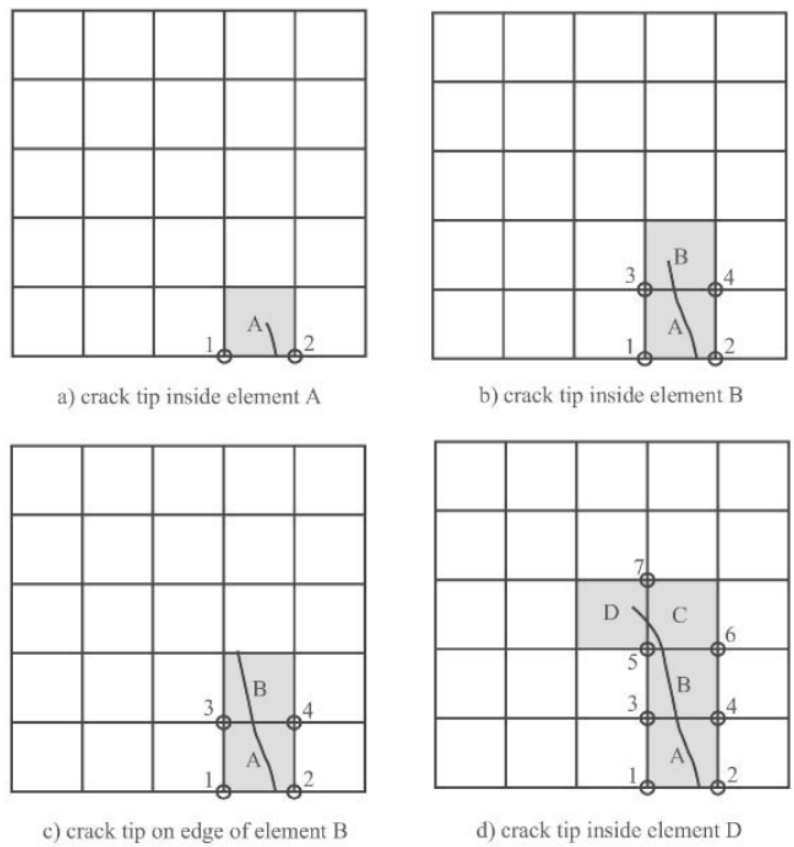

Figure A. 8: Enrichment nodes at different stages of crack propagation [73]

A.4.4 Selection of Nodes For Discontinuity Enrichment

The value of the modified (enriched) shape function N_i^h remains zero at all nodes and edges that do not intersect with the crack. This method only affects the elements containing a crack, and does not directly influence other elements, even if they share a common node with the enriched element.

Figure A. 8 illustrates a simple procedure for selection of nodes for enrichment. At each crack propagation stage, nodes on edges cut by crack path are enriched. Even if the crack tip locates just on an edge, the corresponding nodes are not enriched.

This technique adds two enriched degrees of freedom to an element per any enriched node. For quadrilateral elements on the path of crack, 16 degrees of freedom are assigned: eight classical degrees of freedom and eight enriched degrees of freedom.

XFEM using classical jump functions applies the enrichment onto the nodal points. As a result, elements containing an enriched node are affected by the enrichment degree of freedom. In

a finite element mesh, as shown in Figure A. 9**,** circles mark nodes that are enriched with Heaviside functions and squares mark nodes that are enriched by crack tip functions. The crack does not affect other nodes and their associated classical finite element degrees of freedom.

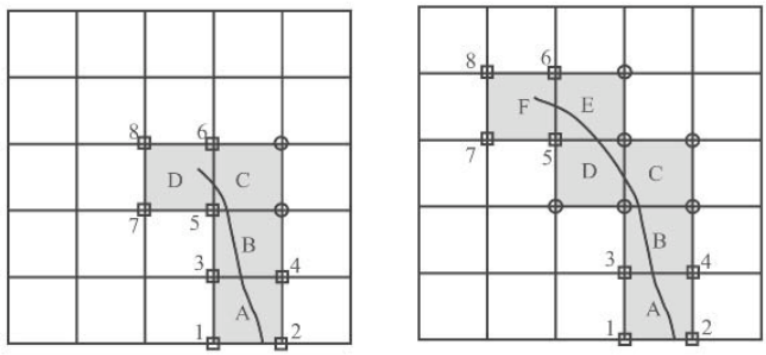

Figure A. 9: Node selection of enrichment at different stages of crack propagation; nodes marked by squares are tip functions enriched and nodes marked by circles are Heaviside enriched function [73]

A.4.5 Modeling The Crack

Moës [44] proposed that Equation (A.3 A.2) be rearranged in order to model crack surfaces and tips in the extended finite element method as below:

$$u^h(x) = \sum_{j=1}^{n} N_j(x)\, u_j + \sum_{k=1}^{m} N_h(x)\, H\big(\xi(x)\big) a_h + \sum_{k=1}^{mt_1} N_k(x) \left(\sum_{l=1}^{mf} F_l^1\,(x) b_k^{l1} \right) + \sum_{k=1}^{mt_2} N_k(x) \left(\sum_{l=1}^{mf} F_l^2\,(x) b_k^{l2} \right) \quad \textbf{(A. 9)}$$

where:

1. m→set of nodes that have the crack face (but not at the crack tip).
2. mt_1 and mt_2 → nodes associated with crack tip1 and 2 in their influence domain, respectively.
3. u_j → nodal displacements (standard dof's).

4. $a_h \rightarrow$ vectors of additional dof's for modeling crack faces.
5. b_k^1 and $b_k^2 \rightarrow$ additional dof's for modeling crack tips.
6. $F_l^i(x), i = 1,2 \rightarrow$ represent *mf* crack tip enriched functions.

In order to include the corrections related to interpolation failure of the enrichment, Eq.(A.9) can be written as:

$$u(x) = \sum_{j=1}^{n} N_j(x)\, u_j + \sum_{k=1}^{m} N_h(x) \left(H\big(\xi(x)\big) - H\big(\xi(x_h)\big) \right) a_h + \sum_{k=1}^{mt_1} N_k(x) \left(\sum_{l=1}^{mf} \left(F_l^1(x) - F_l^1(x_k) \right) b_k^{l1} \right) + \sum_{k=1}^{mt_1} N_k(x) \left(\sum_{l=1}^{mf} \left(F_l^2(x) - F_l^2(x_k) \right) b_k^{l2} \right) \quad \textbf{(A. 10)}$$

A.5 PROPAGATION LAW CRITERIA

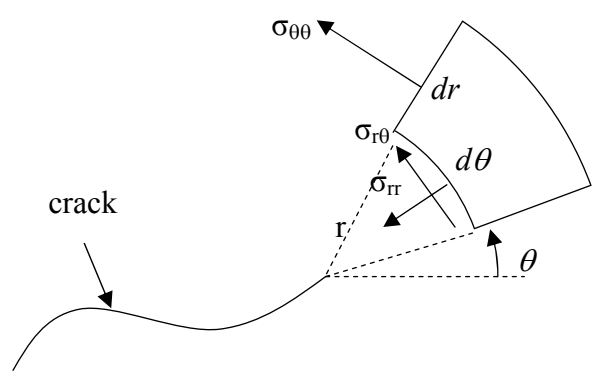

Figure A. 10: Circumferential stress criteria for crack propagation

The most commonly used crack growth criteria in LEFM is the maximum hoop stress criteria. The criterion is based on the evaluation of mixed mode stress intensity factors K_I and K_{II}. According to these criteria we assume that: (i) the crack initiation will occur when the maximum hoop stress reaches to a critical value, (ii) and the crack will grow in a direction $\sigma_{r\theta}$ in which circumferential stress $\sigma_{\theta\theta}$ is maximum. The direction is determined by evaluating the SIF K_I and K_{II} using the

domain form of interaction integral around the crack tip assuming the crack surfaces are traction free. The circumferential stress in the direction of crack propagation is a principal stress; hence, the crack propagation direction is determined by setting the shear stress equal to zero.

$$\sigma_{r\theta} = \frac{1}{2\pi r}\cos\frac{\theta}{2}\left(\frac{1}{2}K_I \sin\theta + \frac{1}{2}K_{II}(3\cos\theta - 1)\right) = 0 \qquad \textbf{(A. 11)}$$

Note that $\theta \neq \pi$ because we are propagating forward; hence, $\cos\frac{\theta}{2} \neq 0$. Thus, the only possibility to find the critical propagation angle is to solve the following equation

$$\frac{1}{2}K_I \sin\theta + \frac{1}{2}K_{II}(3\cos\theta - 1) = 0 \qquad \textbf{(A. 12)}$$

The solution to the above equation also provides the maximum circumferential stress $\sigma_{\theta\theta}$. In order to show this, we express the circumferential stress in polar coordinates (r, θ) belonging to the set of positive real number [-π, π] as follows:

$$\sigma_{\theta\theta} = \frac{1}{4}\frac{K_I}{\sqrt{2\pi r}}\left[3\cos\frac{\theta}{2} + \cos\frac{3\theta}{2}\right] + \frac{1}{4}\frac{K_{II}}{\sqrt{2\pi r}}\left[-3\sin\frac{\theta}{2} - \sin\frac{3\theta}{2}\right] \qquad \textbf{(A. 13)}$$

In order to maximize circumferential stress:

$$\frac{\partial\sigma_{\theta\theta}}{\partial\theta} = K_I\left(\sin\frac{\theta}{2} + \sin\frac{3\theta}{2}\right) + K_{II}\left(\cos\frac{\theta}{2} + 3\sin\frac{3\theta}{2}\right) = 0 \qquad \textbf{(A. 14)}$$

Using trigonometric manipulation and the fact that $\cos\frac{\theta}{2} \neq 0$, we get

$$K_I \sin\theta + K_{II}(3\cos\theta - 1) = 0 \qquad \textbf{(A. 15)}$$

which leads to the same equation that sets to the shear stress to zero (Eq. A.12). We solve the above equation by using the substitution of

$$t = \tan\theta, \quad \cos\theta = \frac{2t}{1+t^2}, \quad \sin\theta = \frac{1-t^2}{1+t^2} \tag{A. 16}$$

we get

$$\theta_c = \tan^{-1}\left[\frac{1}{4}\left(\frac{K_I}{K_{II}}\right)\left(1 \pm \sqrt{1+8\left(\frac{K_{II}}{K_I}\right)^2}\right)\right] \tag{A. 17}$$

where θ_c is the crack growth angle in the local crack-tip coordinate system. If $K_{II} = 0$ then $\theta_c = 0$ (pure mode I). By noting that if $K_{II} > 0$ then the crack growth angle $\theta_c < 0$; and if $K_{II} < 0$ then the crack growth angle $\theta_c > 0$. Hence, the critical may be expressed as follows [74]:

$$\theta_c = \tan^{-1}\left[\frac{1}{4}\left(\frac{K_I}{K_{II}}\right)\left(1 - \sqrt{1+8\left(\frac{K_{II}}{K_I}\right)^2}\right)\right] = 2\tan^{-1}\left[\frac{-2\left(\frac{K_{II}}{K_I}\right)}{1+\sqrt{1+8\left(\frac{K_{II}}{K_I}\right)^2}}\right] \tag{A. 18}$$

A.6 XFEM DISCRETIZATION AND INTEGRATIONS

A.4.1 Governing Equations

The variational formulation of the boundary value problem can be defined as:

$$\int_{\Omega} \sigma\delta\varepsilon d\Omega = \int_{\Omega} f^b \delta u d\Omega + \int_{\Gamma} f^t \delta u d\Gamma \tag{A. 19}$$

where $\boldsymbol{\sigma}$ is the stress tensor, f^b and f^t are the body force and external traction vectors.

Discretization of Eq. (A.19) using the XFEM results in a discrete system of linear equilibrium equations:

$$K * u^h = f \tag{A. 20}$$

where:

$K \rightarrow$ stiffness matrix

$u^h \rightarrow$ vector of dof's (classical and enriched)

$f \rightarrow$ vector of external forces

The global matrix and vectors are calculated by assembling the matrix and vectors of each element. For each element, K and f are defined as:

$$K_{ij}^{uu} = \begin{bmatrix} K_{ij}^{uu} & K_{ij}^{ua} & K_{ij}^{ub} \\ K_{ij}^{au} & K_{ij}^{aa} & K_{ij}^{ab} \\ K_{ij}^{bu} & K_{ij}^{ba} & K_{ij}^{bb} \end{bmatrix} \tag{A. 21}$$

$$f_i^e = [f_i^u \quad f_i^a \quad f_i^{b1} \quad f_i^{b2} \quad f_i^{b3} \quad f_i^{b4}] \tag{A. 22}$$

where $u^h \rightarrow$ vector of nodal parameters:

$$u^h = \{u \quad a \quad b_1 \quad b_2 \quad b_3 \quad b_4\}^T \tag{A. 23}$$

with,

$$K_{ij}^{rs} = \int_{\Omega^e} (B_i^r)^T D B_j^s \, d\Omega \tag{A. 24}$$

$$f_i^u = \int_{\Gamma_t} N_i f^t \, d\Gamma + \int_{\Omega_t^e} N_i f^b \, d\Omega \tag{A. 25}$$

$$f_i^{b\alpha} = \int_{\Gamma_t} N_i F_\alpha f^t \, d\Gamma + \int_{\Omega_t^e} N_i F_\alpha f^b \, d\Omega .....(\alpha = 1, 2, 3 \text{ and } 4) \tag{A. 26}$$

In Eq.(A.24), B is the matrix of shape function derivatives,

$$B_i^u = \begin{bmatrix} N_{i,x} & 0 \\ 0 & N_{i,y} \\ N_{i,y} & N_{i,x} \end{bmatrix} \tag{A. 27}$$

$$B_i^a = \begin{bmatrix} \left(N_i H\right)_{,x} & 0 \\ 0 & \left(N_i H\right)_{,y} \\ \left(N_i H\right)_{,y} & \left(N_i H\right)_{,x} \end{bmatrix} \tag{A. 28}$$

$$B_i^b = \begin{bmatrix} B_i^{b1} & B_i^{b2} & B_i^{b3} & B_i^{b4} \end{bmatrix} \tag{A. 29}$$

$$B_i^a = \begin{bmatrix} (N_i F_\alpha)_{,x} & 0 \\ 0 & (N_i F_\alpha)_{,y} \\ (N_i F_\alpha)_{,y} & (N_i F_\alpha)_{,x} \end{bmatrix} .....(\alpha = 1, 2, 3 \text{ and } 4) \tag{A. 30}$$

To include the effects of interpolation, the following shifting amendments are required:

$$B_i^a = \begin{bmatrix} N_i[H(\xi) - H(\xi)]_{,x} & 0 \\ 0 & N_i[H(\xi) - H(\xi)]_{,y} \\ N_i[H(\xi) - H(\xi)]_{,y} & N_i[H(\xi) - H(\xi)]_{,x} \end{bmatrix} \tag{A. 31}$$

$$B_i^\alpha = \begin{bmatrix} [N_i(F_\alpha - F_{\alpha i})]_{,x} & 0 \\ 0 & [N_i(F_\alpha - F_{\alpha i})]_{,y} \\ [N_i(F_\alpha - F_{\alpha i})]_{,y} & [N_i(F_\alpha - F_{\alpha i})]_{,x} \end{bmatrix} .....(\alpha = 1, 2, 3 \text{ and } 4) \tag{A. 32}$$

In order to determine the rest of the computations needed, first we have to consider the type of enrichment function. The following types are considered:

1) Heaviside Function $\psi(x) = H(\xi)$

Derivative of the Heaviside function is the Dirac delta function $H_{,i}(\xi) = \delta(\xi)$. This vanishes except at the position of the crack interface:

$$H_{,i}(\xi) = \begin{cases} 1 & \text{at crack tip} \\ 0 & \text{otherwise} \end{cases} \qquad \textbf{(A. 33)}$$

As a result, Eq. (A.31) can be written as:

$$B_i^a = \begin{bmatrix} N_{i,x}H & 0 \\ 0 & N_{i,y}H \\ N_{i,y}H & N_{i,x}H \end{bmatrix} \qquad \textbf{(A. 34)}$$

2)Weak discontinuity function $\psi(x) = \chi(x) = |\xi(x)|$

Derivatives of $\xi(x)$ are calculated from the derivatives of the shape functions if a standard finite element interpolation is adopted to define the function in terms of its nodal values:

$$\begin{aligned} \xi(x) &= \sum_{j=1}^{4} N_j(x)\xi_j \\ \xi_{,i}(x) &= \sum_{j=1}^{4} N_{j,i}(x)\xi_j \end{aligned} \qquad \textbf{(A. 35)}$$

3)Near tip enrichment functions $\psi = F_\alpha(r,\theta)$

Near tip enrichment functions have already been defined in terms of the local crack tip coordinates system(r, θ).

$$F_\alpha(r,\theta) = \left\{ \sqrt{r}\sin\left(\frac{\theta}{2}\right) \quad \sqrt{r}\cos\left(\frac{\theta}{2}\right) \quad \sqrt{r}\sin(\theta)\sin\left(\frac{\theta}{2}\right) \quad \sqrt{r}\sin(\theta)\cos\left(\frac{\theta}{2}\right) \right\} \qquad \textbf{(A. 36)}$$

Derivatives of $F_\alpha(r,\theta)$ with respect to the crack tip polar coordinates (r,θ) become:

$$F_{1,r} = \frac{1}{2\sqrt{r}}\sin\left(\frac{\theta}{2}\right) \qquad F_{1,\theta} = \frac{\sqrt{r}}{2}\cos\left(\frac{\theta}{2}\right) \qquad \textbf{(A. 37)}$$

$$F_{2,r} = \frac{1}{2\sqrt{r}}\cos\left(\frac{\theta}{2}\right) \qquad F_{2,\theta} = -\frac{\sqrt{r}}{2}\sin\left(\frac{\theta}{2}\right) \qquad \textbf{(A. 38)}$$

$$F_{3,r} = \frac{1}{2\sqrt{r}}\sin\left(\frac{\theta}{2}\right)\sin(\theta) \qquad F_{3,\theta} = \sqrt{r}\left(\frac{1}{2}\cos\left(\frac{\theta}{2}\right)\sin(\theta) + \sin\left(\frac{\theta}{2}\right)\cos(\theta)\right) \qquad \textbf{(A. 39)}$$

$$F_{4,r} = \frac{1}{2\sqrt{r}}\cos\left(\frac{\theta}{2}\right)\sin(\theta) \qquad F_{4,\theta} = \sqrt{r}\left(-\frac{1}{2}\sin\left(\frac{\theta}{2}\right)\sin(\theta) + \cos\left(\frac{\theta}{2}\right)\cos(\theta)\right) \qquad \textbf{(A. 40)}$$

And the derivatives of $F_\alpha(r,\theta)$ with respect to the local coordinate system (x^l, y^l) are:

$$F_{1,x^l} = \frac{1}{2\sqrt{r}}\sin\left(\frac{\theta}{2}\right) \qquad F_{1,y^l} = \frac{\sqrt{r}}{2}\cos\left(\frac{\theta}{2}\right) \qquad \textbf{(A. 41)}$$

$$F_{2,x^l} = \frac{1}{2\sqrt{r}}\cos\left(\frac{\theta}{2}\right) \qquad F_{2,y^l} = -\frac{\sqrt{r}}{2}\sin\left(\frac{\theta}{2}\right) \tag{A. 42}$$

$$F_{3,x^l} = \frac{1}{2\sqrt{r}}\sin\left(\frac{\theta}{2}\right)\sin(\theta) \qquad F_{3,y^l} = \sqrt{r}\left(\frac{1}{2}\cos\left(\frac{\theta}{2}\right)\sin(\theta) + \sin\left(\frac{\theta}{2}\right)\cos(\theta)\right) \tag{A. 43}$$

$$F_{4,x^l} = \frac{1}{2\sqrt{r}}\cos\left(\frac{\theta}{2}\right)\sin(\theta) \qquad F_{4,y^l} = \sqrt{r}\left(-\frac{1}{2}\sin\left(\frac{\theta}{2}\right)\sin(\theta) + \cos\left(\frac{\theta}{2}\right)\cos(\theta)\right) \tag{A. 44}$$

Finally, the derivatives in the global coordinate system are obtained:

$$F_{\alpha,x} = F_{\alpha,x^l}\cos(\alpha) - F_{\alpha,y^l}\sin(\alpha) \tag{A. 45}$$

$$F_{\alpha,y} = F_{\alpha,x^l}\sin(\alpha) - F_{\alpha,y^l}\cos(\alpha) \tag{A. 46}$$

where α is the angle of crack path with respect to the *x*-axis.